Title

The role of energy reservoirs in distributed computing: Manufacturing, implementing, and optimizing energy storage in energy-autonomous sensor nodes

Author

Cowell, Martin A

Publication Date

2017

The role of energy reservoirs in distributed computing: Manufacturing, implementing, and optimizing energy storage in energy-autonomous sensor nodes

by

Martin Andrew Cowell

A dissertation submitted in partial satisfaction of the

requirements for the degree of

Doctor of Philosophy

in

Engineering - Mechanical Engineering

in the

Graduate Division

of the

University of California, Berkeley

Committee in charge:

Professor Paul K. Wright, Chair
Professor James W. Evans
Professor Hayden Taylor

Summer 2017

The role of energy reservoirs in distributed computing: Manufacturing, implementing, and optimizing energy storage in energy-autonomous sensor nodes

Abstract

The role of energy reservoirs in distributed computing: Manufacturing, implementing, and optimizing energy storage in energy-autonomous sensor nodes

by

Martin Andrew Cowell

Doctor of Philosophy in Engineering - Mechanical Engineering

University of California, Berkeley

Professor Paul K. Wright, Chair

The world already hosts more internet connected devices than people, and that ratio is only increasing. These devices seamlessly integrate with peoples lives to collect rich data and give immediate feedback about complex systems from business, health care, transportation, and security. As every aspect of global economies integrate distributed computing into their industrial systems and these systems benefit from rich datasets. Managing the power demands of these distributed computers will be paramount to ensure the continued operation of these networks, and is elegantly addressed by including local energy harvesting and storage on a per-node basis. By replacing non-rechargeable batteries with energy harvesting, wireless sensor nodes will increase their lifetimes by an order of magnitude.

This work investigates the coupling of high power energy storage with energy harvesting technologies to power wireless sensor nodes; with sections covering device manufacturing, system integration, and mathematical modeling. First we consider the energy storage mechanism of supercapacitors and batteries, and identify favorable characteristics in both reservoir types. We then discuss experimental methods used to manufacture high power supercapacitors in our labs. We go on to detail the integration of our fabricated devices with collaborating labs to create functional sensor node demonstrations.

With the practical knowledge gained through in-lab manufacturing and system integration, we build mathematical models to aid in device and system design. First, we model the mechanism of energy storage in porous graphene supercapacitors to aid in component architecture optimization. We then model the operation of entire sensor nodes for the purpose of optimally sizing the energy harvesting and energy reservoir components. In consideration of deploying these sensor nodes in real-world environments, we model the operation of our energy harvesting and power management systems subject to spatially and temporally varying energy availability in order to understand sensor node reliability. Looking to the future, we see an opportunity for further research to implement machine learning algorithms to control the energy resources of distributed computing networks.

To: An energetically and computationally autonomous future

Contents

List of Figures

List of Tables

Acknowledgments

My time at UC Berkeley has been a period of enormous growth. Through collaborations, courses, discussions, and campus groups I have been privileged to learn subjects that I previously never new existed. Here I have met some of the world's brightest and most curious minds, and have relied on the support from some of most caring characters of my life. I am grateful that I have had this unique opportunity to develop relationships with people who will certainly change the world. I could not have thrived in this fast environment without the support of many people.

First I would like to thank my parents, John and Nina, for their unwavering support. They fostered my foundation of curiosity and have consistently encouraged my pursuits. Their voices have been a guidind g light and a grounding perspective.

I would also like to thank my advisors, Prof. Paul K. Wright and Prof. James W. Evans, for always pushing my work. They have taught me to persevere through long projects and have enabled me to navigate dynamic research terrain.

I would like to thank Dr. Rich Winslow for acting as a guide and tutor to the first years of my program and for helping to get me into the AME lab. Without his guidance I would have been swimming against a torrent.

Finally, I would like to thank all of my colleagues and friends for helping me along the path: Dr. Balthazar Lenchene, Eric Munsing, Bernard Kim, Zach Gima, Dan Chapman, Katherine Latimer, Qian Zhang, Christine Gregg, Bala Thoravi Kumaravel, Payton Goodrich, Isabel Yang, Marco Salvioli Mariani, Dr. Pit Pillatsch, Sean Wihera, Dominic Cincione, Adrien Pierre, Neeka Mashouf, Prof. Ana Arias, Prof. Eric Yeatman of Imperial College London, Prof. Scott Moura, Dr. Abhinav Gaikwad, and Alla Zaramayeva.

Chapter 1

Introduction and Motivation

By the year 2020, the world will host 200 billion internet connected (smart) devices in a network called the Internet of Things (IoT). These devices will seamlessly integrate with peoples lives to collect rich data and give immediate feedback about complex systems like business, health care, retail, and security. Industry will see radical benefit from rich datasets if smart devices are able to achieve ubiquitous adoption. Managing the power demands of these distributed computers will be paramount to ensure the continued operation of these networks, and is elegantly addressed by including local energy harvesting and storage on a per-node basis. By replacing non-rechargeable batteries with energy harvesting, wireless sensor nodes will increase their lifetimes by an order of magnitude.

1.1 Energy Storage Considerations for Energy Harvesting Applications

Supercapacitors are an energy storage technology that can supply high power and can survive for millions of charge and discharge cycles. A supercapacitor stores energy much in the same way as a parallel plate capacitor - by maintaining charge separation over very short distances. By understanding the operation of a parallel plate capacitor we are able to extend these principles to understand the supercapacitor.

Accurately measuring the behavior of supercapacitor cells is paramount for predicting their performance in an energy storage application. To measure the behavior of an electric double layer cell, it can be informative to model the system behavior as a low-order equivalent circuit and subject the cell to a broad spectrum of frequency inputs, also known as electrochemical impedance spectroscopy. The first-order circuit of a supercapacitor (sometimes called a Randles cell) includes series resistance and leakage resistance. Such a circuit exhibits a predictable response over a full range of excitation frequencies. By observing the real and reactive power across the supercapacitor cell, one can identify the cell's capacitive, resistive, and diffusive parameters.

In addition to understanding the supercapacitor's capacitive and resistive parameters, an energy storage designer must also consider the cell's energy and power capabilities. These quantities are best understood by plotting the cell's performance on a Ragone plot. In this analysis, the supercapacitor excels in high-power and low energy applications because it stores energy in a non-faradaic process. Battery technologies, on the other hand, are rate limited by chemical reactions and therefore show lower power and higher energy. To consider The DC application of interest, a power system designer should first understand the power demands of the load.

1.2 Load Demand Characteristics

Constant-current discharge tests are widely accepted in industry as the method for determining battery capacity. Pulse load demands often de-rate the energy storage capacity of commercial batteries beyond the values specified in their datasheets. In the battery market, many datasheets include top level information like nominal voltage and cell capacity which are important to the average customer, but may not include more specialized data on electrical performance or operating conditions that is important for product designers. Battery companies do not have a standardized template or format for battery specification sheets. This makes it difficult for product developers to make an informed comparison of different energy reservoirs they may consider for integration for unique load demands.

To support ubiquitous computing, IoT and wearable electronics often leverage wireless communication and power-hungry sensors to perform their unique tasks. These electronics have characteristically short duration, high peak current demands, which are not characterized well by the constant-current discharge tests commonly performed by battery manufacturers [28]. Because battery performance characteristics for constant-current discharge conditions are provided on battery specification sheets, product designers make the common mistake of averaging peak currents over low duty cycles to estimate the expected life of their battery powered system. This averaging results in overestimation of their batterys capacity and an unexpectedly short product life. The white paper from the collaboration between Nordic and Energizer [28] examines the effect of varying the pulse period, and the pulse amplitude while holding the other variables constant. The comparison of capacity, pulse amplitude, pulse duration, and pulse period highlights the importance of considering the load demand's time-dependent character when estimating an energy reservoir's life.

Energy storage manufacturing: Dispenser printing and screen printing

Many commercial supercapacitors are fabricated using carbon electrodes, liquid electrolyte, and a polymer separation layer. This architecture enables large throughput production like that of battery manufacturing, but requires a rigid enclosure to contain the liquid electrolyte and maintain layer separation. To create thin, flexible supercapacitors, an alternate approach is used wherein the layers of a supercapacitor are built within a polymer matrix. With this technique, the carbon electrodes are suspended in and separated by a porous polymer matrix which both contains the electrolyte and bonds to the surface of the electrodes. By using functional inks that contain a common polymer, these layers can be built up using a printing process to create a self-contained, polymer-bound supercapacitor.

Powering high-current micro devices with low-power generation often found at the micro-scale [4, 48] requires that energy be trickle-charged into a storage device capable of high-current discharge. While arrays of micro piezoelectric vibrational energy harvesters have been used to increase system output power [52], the power required to energize a wireless radio is still much higher [82, 15]. Charge storage via an electric double layer, such as found in a supercapacitor, offers high-current discharging while maintaining long cycle-life performance. The thermal and chemical stability of the ionic liquid electrolyte 1-butyl-3-methylimidazolium tetrafluoroborate ([BMIM+][BF4-]) (BMIMBF4) allows the thick film capacitor to be employed in harsh environments where aqueous electrolytes would otherwise evaporate [17], while the polymer binder allows for structural flexibility.

In the lab, we have produced supercapacitors with dry electrodes composed of activated carbon (AC), acetylene black (AB), graphite (GR), and poly(vinylidene fluoride-cohexafluoropropylene) (PVDF-HFP). Previous work by our lab used mesocarbon microbeads (MCMB) and AB as active electrode materials [36], but these have been found to have an inferior capacitance per electrode dry weight. To improve capacitance performance, composite electrodes leverage the high surface area of AC with the electrically conductive microstructure of AB [87] and structural reinforcement of GR. The solvent n-methylpyrrolidone (NMP) suspends the active material and solvate the polymer binder to achieve favorable rheological properties for printed manufacturing. The electrode and separator layers are printed with a CNC pneumatic dispenser printer, and the cell is dried after each layer is deposited. After drying, the electrode and separator layers are saturated with liquid electrolyte before they can function. Testing is done in a coin-cell enclosure to ensure repeatable contact, but can also be done with flexible current collectors if the application requires it.

Screen printing promises to allow higher throughput and more consistency in controlling layer thickness. The performance of a screen for screen printing is inherently built into the parameters and properties of the screen's mesh. Because these parameters are locked in once a screen is fabricated, careful calculation is required when designing a screen for printing electronics. Beyond the footprint pattern, the designer must consider the desired wet-layer thickness and the minimum in-plane feature size. These output characteristics are calculated by considering the mesh diameter and the open fraction.

Because a screen printing screen cannot be easily modified after it is manufactured, a print designer is constrained to a single 'footprint' design for each set of screens. It is at the stage of drawing up the screen's footprint that the designer has the greatest opportunity to leverage their creative freedom toward accomplishing the end goal simply and concisely.

1.3 Device-level Modeling of Energy Storage Phenomena

As industrial and commercial demand for thin, small-footprint energy storage devices increases (e.g., for wearable electronics, wireless sensor networks, etc.), it is essential to develop theoretical descriptions for those devices in order to make effective design choices. Of particular interest are porous interdigitated electrodes, which can function as supercapacitors but which are nontrivial to analyze due to their unique geometry. We develop a purely mathematical model to determine the dependence of a cell's capacitance and/or resistance on electrode height, width, and spacing, and electrolyte layer height. We then extend this model to incorporate effects from the porous nature of the electrodes, and show that in many cases of interest, the system can be described using a simple equivalent circuit.

The advancement of miniaturized, wearable electronics has increased the demand for thin, flexible energy storage. Two-dimensional or in-plane electrode geometries can be fabricated in a single process and are more robust against bending when compared to stacked electrode geometries [43, 67]. Supercapacitors are especially relevant to modern electronics, as they can readily meet high power demands associated with wireless communication. Here we develop an analytical model of interdigitated supercapacitor electrodes to understand the effect of device design on the performance of the planar supercapacitor.

Theory and Results

In what follows we make the usual assumption that the matrix phase of the electrode and the electrolyte therein can be treated as two superimposed continua with macroscopically uniform properties [55]. We further assume that conduction in the matrix obeys Ohms law with some effective conductivity. Finally, we assume that conduction in the electrolyte will also obey Ohms law. This last assumption is made because we are primarily interested in electrolytes that are ionic liquids consisting of one cation, one anion and no solvent; consequently, electroneutrality mandates there can be no concentration gradients, outside double layers, and therefore conduction in the electrolyte is only by migration. The assumption is also valid for electrolytes, with a solvent, that are well supported electrolytes. The assumption would be an approximation in other cases.

Of interest in this study is whether, and to what extent, a simplified equivalent circuit model can describe the behavior of the porous interdigitated electrode system. In order to investigate this, the parameters for electrolyte conductivity and electrode specific capacitance were varied over a range encompassing the baseline values of 1 S/m and 100 F/cm^3 (respectively), and exponential curves were fitted to the FEA output for current through the cell versus time.

The Schwarz-Christoffel conformal mapping can be used to analyze the relationship between a cell's capacitance/resistance and its geometric parameters (electrode height, width, and spacing, and electrolyte layer height) for an interdigitated electrode configuration. Results from this mathematical technique are confirmed by - and even show signs of improvement in speed and accuracy over - FEA. Therefore, given specific practical constraints (for example on cell volume, amount of electrode material to be used, etc.), one can optimize the cell's electrical characteristics.

1.4 System Integration: Energy Harvesting and Storage

Indoor Photovoltaic Energy Harvesting

Organic solar cells (OSC) currently achieve more than 10% of power conversion efficiency (PCE) under 1-sun conditions [33, 9] and can be stable over several years [60, 30]. The materials involved in their fabrication require low processing temperatures, compatible with many plastic substrates [22, 23]. They can also be completely printed [1, 31], allowing the use of large area, high throughput, low cost manufacturing processes such as roll-to-roll printing. As a result, full-scale outdoors demonstrations have already been successfully performed [38, 2].

Previous studies on the operation of organic solar cells under low light intensity suggested that an important parameter to control is the shunt resistance. Proctor and Nguyen [64] report that for a shunt resistance (R_{sh}) lower than 1 $M\Omega - cm^2$ the JV characteristics of solar cells can be significantly affected by parasitic leakage current for lights between 100 mW/cm^2 and 2 mW/cm^2. Steim et al. [75] show that a shunt resistance of at least 85 $k\Omega - cm^2$ is needed for operation under 1000 lx of a fluorescent lamp and that, overall, the performance of the solar cells under low light increases with higher shunt resistance. Zhou et al. [90] have also developed a solar cell which performs well under room light and exhibits a $R_{sh} = 10^8 \Omega cm^2$.

Here, the thickness of the PEIE layer is varied in order to control the shunt resistance and optimize the organic solar cells for indoor light. Previous studies [89, 50] have shown that PEIE is an insulator which can modify the series resistance and the work function of the cathode as a function of its thickness. PEIE thickness has also been shown to influence the reverse bias saturation dark current in organic photodiodes [61].

To support the power demands of the application, the parameters of the supercapacitor must be tailored. First, the supercapacitor must store enough charge to supply the load demand's integrated current profile. Second, the supercapacitor's maximum voltage must be greater than the open circuit voltage of the solar cell.

The supercapacitors primarily discussed in this work are printed and structured in a sandwich architecture. They consist of symmetric, composite carbon electrodes on either side of a gel polymer electrolyte. The gel polymer acts as a porous separator between the electrodes and houses the ionic liquid electrolyte butyl-methyl-imidazolium tetrafluoroborate (BMIM BF4) which allows ion migration. The electrodes consist of a threefold composite of activated carbon (AC), acetylene black (AB), and graphite (GR) held in a polymer binder of poly(vinylidine fluoride-co-hexafluoropropylene) (PVDF-HFP). The constituents of these electrodes are chosen to provide both good electrical conductivity and mechanical strength. The high surface area of AC acts as the main component to support the electric double layer phenomenon responsible for the high-energy storage in super-capacitors. AB provides electrical pathways between AC grains and improves electrical conductivity within the electrodes. AB is present at the critical fraction to engender markedly improved electrical conductivity. Graphite's large repeating structural flakes provide mechanical strength and electrical conductivity within the electrode. Finally, the PVDF-HFP binder fraction lends mechanical flexibility to the super-capacitor, and its fraction must be considered a trade off between electrical performance and mechanical flexibility.

Organic solar cells for indoor operation need to be specifically optimized for their unique spectral and intensity conditions. Particularly, achieving a low dark current is essential to maintaining a high PCE under low light intensities. Optimizing the thickness of the PEIE layer is an efficient way of controlling the dark current and we demonstrate cells with PCE of 7.6% under simulated indoor light. The ratio of dark current over short-circuit current is identified as a reliable indicator of the minimal light power below which a cell's efficiency decreases sharply. Fully-printed supercapacitors were developed, showing a maximum discharge capacitance of 130 mF/cm^2, and provided a maximum power of 9.8 mW/cm^2, and maximum energy of 31 $\mu W - hr/cm^2$. Those supercapacitors were integrated with OSC to form photo-rechargeable systems. Under 1-sun light, such systems had 1.56% of ECSE and generated 26 mJ of energy and up to 4 mW of power. Under simulated indoor light, photo-rechargeable systems using OSC optimized for indoor operation yielded 15% more energy per cycle than those using OSC optimized for 1-sun. The indoor-optimal photo-rechargeable system charged under indoor light for 3090 s provides energy and power levels similar to the 1-sun scenario, and reaches 2.92% of ECSE. Overall, these results suggest that organic solar cells are viable for powering autonomous sensor applications in various light environments.

Demonstration: WSN harvesting Indoor Light with a Single Reservoir using Voltage Triggering Algorithm

Indoor ambient light is a readily available source of energy for microelectronic devices, but its low power density has typically meant it is not considered for wireless sensor node (WSN) applications [76]. We extend prior literature on indoor photovoltaic energy harvesting by fabricating and demonstrating a wireless sensor node in which a spectrum-tailored organic solar cell is used to charge a supercapacitor, which in turn intelligently powers a radio payload using a state-based control strategy.

Because solar cells are generally optimized for outdoor use, their performance is traditionally measured under 1-sun standard irradiance of 100 mW/cm^2 with AM 1.5G spectrum. However, indoor conditions differ considerably from this conventional scenario. First, indoor light intensity is characterized in illuminance, as seen by the human eye. Standard indoor illumination at 300 *lux* corresponds to 100-500 $\mu W/cm^2$ irradiance depending on the light source. Second, the light spectrum is very different than the sun. The absorption spectrum of organic photo-active materials is well-suited to absorb indoor light spectra, so they are a natural solution for indoor light harvesting. The solar cells absorption spectra overlaps well with high fractions of LED and CFL emission spectra. By tailoring the energy harvester to the intended environment, we are able to operate in very low power-availability environments. Indoor lighting intensity in workspaces and industrial settings is internationally regulated and must be above a minimum threshold [19, 74]. This lighting level is adequate to power our WSN with a periodicity below one minute, a frequency applicable for intermittent sensing applications like environmental monitoring.

To meet the power demands of wireless sensor operation and communication protocols, energy harvested from the OSC accumulates in the high-power energy reservoir of a printed carbon supercapacitor [16, 47] for use during radio transmission. It is important to avoid oversizing the supercapacitor in this low-power harvesting environment to mitigate leakage currents. An excessively leaky reservoir can quickly make the WSN inoperable in low-power harvesting environments.

In this demonstration we implement a triggering algorithm wherein the WSN lies dormant until the energy stored in the supercapacitor is adequate to power sensing and transmission protocols. The WSN cold-starts when the radio's low voltage bound is reached and immediately enters a sleep state. The supply voltage continues to scale linearly as the supercapacitor accumulates charge. The WSN wakes periodically to measure the reservoir's bus voltage. Once the bus voltage exceeds a threshold voltage, the WSN senses from the accelerometer and transmits the data via advertising packet. The triggering voltage must be above the cold start voltage plus the worst case voltage drop. We demonstrate an energy harvesting WSN that integrates a printable organic solar cell and printed supercapacitor to power the WSN in indoor light. Power is managed with a simple voltage-based triggering algorithm that only enables data acquisitions and transmission once the supercapacitor is adequately charged. This demonstration shows time-series acceleration data being transmitted to a base station where it is processed to view the frequency response.

With this work we demonstrate a wireless sensor node capable of running exclusively on indoor light, illustrating feasibility for nodes that can operate autonomously in low-light and indoor environments.

1.5 System Modeling for Optimal Sizing

Optimal Sizing: Dynamic Programming

In this section, we focus on creating a tool for optimizing the energy management within a WSN of centimeter scale. The modeled components are printed and flexible and support a wireless sensor node. Current work uses printed thermoelectric generators [53] for energy harvesting, rechargeable printed batteries [35] for energizing a low-power microcontroller, and printed supercapacitors [16] for high power communications via radio. These components have been characterized individually, but their integration into a single device as a unified power platform is not optimized - resulting in over sized components and excess device footprint. The design tool discussed here examines current work as described above but can be easily extended beyond this specific system, allowing node designs that harvest energy from light, motion, or others, and sense temperature, light intensity, chemical presence, humidity, vibration, or others. Microcontroller, sensor, and radio duty cycles all contribute to the power demands of a wireless sensor node, so this novel design tool will allow for engineered exploration of the node feasibility space using printed electronics for energy harvesting and storage.

Modeling the first-order equivalent circuits that describe sub-components within the wireless node provides insight into the transient behavior of the power platform. Understanding this transient behavior is important in ensuring that current and potential at the load node never move outside the design specifications required by the load.

The equivalent circuit model of a semiconductor-based thermoelectric generator is described as a variable voltage source in series with a resistor [51]. Five physical processes dictate the performance of the variable voltage source:

1. Kirchoff's Voltage Law
2. Kirchoff's Current Law
3. Heat Conduction
4. Joule Heating
5. Seebeck Power Generation

Battery polarization voltage is characterized by two phenomena ion concentration and electrochemical polarizations [42]. This second order RC model accounts for these two phenomena separately. Using Kirchhoffs laws, two current nodes and one voltage loop can be used to determine the characteristic equations for a battery.

Non-ideal supercapacitors are represented by an ideal capacitor in series and parallel with resistors that represent real-world phenomena. Series resistance accounts for ion adsorption time dependence and internal electrical resistances, while the parallel resistor accounts for leakage currents across the supercapacitors electrolyte layer. Kirchhoffs laws are similarly used to describe the equivalent circuit.

The Dynamic Program (DP) developed in this model gives the system designer the ability to peer into the time-series response of the energy reservoirs of the power platform for printed wireless sensor nodes. Collected lab data is used to identify parameters of the printed supercapacitor, printed battery, and printed thermoelectric generator. As the model exists now, it forgoes state and control dependent parameterization, however further opportunities have been identified for including these real device nonlinearities. Identification of the equivalent circuit models for individual components and their characteristic equations is outlined herein. The diagrams electrical connections within the power platform and the system of equations that describes the power platform is the basis of this model.

The work produces an optimal current dispatch tool that informs printed wireless sensor node design and lays the foundation for a device footprint optimization tool. Such a tool empowers the Industrial Internet to bring about global abundance. Understanding the feasibility space of application-specific sensor nodes enables optimized system design and leads to footprint reduction on the scale necessary for economic ubiquitous sensor networking. The original deliverables for this project highlighted system integration modeling to identify optimum system requirements for tailored printed sensor designs and to ascertain simplified use configurations. The power platform model discussed here achieves these goals and has already obviated a simple use case wherein the battery reservoir is eliminated. Two topics are identified for further modeling: First, the inclusion of the node voltage state space for key nodes in the power platform (referred to as the equivalent circuit model). Second, the expansion of the equivalent circuit model via non-constant and nonlinear parameterization of circuit elements will be further modeled.

Optimal Sizing: Particle Swarm Optimization

Energy management systems for wireless sensor nodes must deliver reliable power and voltage while being small and low-cost. In prior literature, power reliability is maintained by using active energy management components (voltage regulators, DC/DC converters), but these impose efficiency losses [41] while increasing device cost and size [77, 32]. While the use of an active energy management system allows for a convex formulation of the optimal sizing problem in a two-reservoir battery/capacitor system [39], the passive energy management problem is nonconvex and has not been explored in prior literature.

This work extends prior literature on energy management in energy harvesting systems in the following ways:

- Demonstrates a method for designing a passive energy management system without the use of voltage regulators or DC/DC converters, and
- Applies particle swarm optimization to microelectronic energy management system design.

We consider an equivalent circuit circuit model in which power is harvested through strings of thermoelectric generator cells (TEGs) in series; the approach we consider can also accommodate photovoltaics or other energy harvesting modes [48]. Charge is stored in parallel banks of supercapacitors and batteries; the components are linked by a main bus at voltage V. A radio is attached to the bus, and is modeled as a current sink with 15-second cycles with a deterministic current profile. We seek to design an energy management system which can repeat a representative load cycle indefinitely.

We expand on the methods in [77, 32, 49, 73] to provide a baseline estimate of system design using conventional engineering calculations.

Particle Swarm Optimization is a nonlinear optimization method in which a large number of particles explore the parameter space to identify a low-cost solution [63]. We provide a brief description of our implementation below; additional details can be found in [63] and associated references.

We demonstrate a method for energy management in a wireless sensor node which does not require the use of voltage regulators or DC-DC converters, instead satisfying payload requirements through optimal component sizing. Using particle swarm optimization, we find a design with significant reductions in system cost relative to conventional engineering calculations. While this nonlinear optimization technique does not guarantee a globally optimal design, it can be readily applied to other demand profiles and generation/storage technologies and we expect that similar results may be found in other energy management problems.

1.6 Stochastic Modeling (necessitated by real-world conditions)

To understand and predict the variability of available energy for solar harvesting, we examine a dataset of solar irradiance collected in the field. The data are available from NRELs South Park field station and cover a period of 13.8 years from 2003 to 2017. Representative data are collected on five-minute intervals, which provide resolution to observe short-term events like cloud cover, medium-term events like the diurnal cycle of the sun, and long-term events like season changes. By examining daily cycles and binning into seasons we are able to examine the five-minute mean and variance of solar irradiance for the four seasons. By considering this seasonal five-minutely data, we create a probability density function that obeys the mean and variance of the dataset. With this time-series probability density function we are able to create random days that obey the statistical nature of the dataset and which can be fed into a model of WSN energy flow behavior to predict reliability of individual.

Chapter 2

Supercapacitors and their use as energy storage

2.1 Mechanism of Energy Storage

A supercapacitor stores energy much in the same way as a parallel plate capacitor - that is by maintaining charge separation over very short distances. By understanding the operation of a parallel plate capacitor we are able to extend these principles to understand the supercapacitor.

A parallel plate capacitor (PPC) is made up of two electrically conducting plates which are separated by an electrically insulating separator layer as seen in figure 2.1. The separator layer in its most basic form is a vacuum, but is often made of a polymer for reasons of practicality. When a differential charge $(+/-Q)$ is placed between the two plates of the PPC, an electric field develops between the two plates. Energy stored in this electric field manifests as a voltage that is proportional to the charge stored on the plates and inversely proportional to the system's capacitance (equation 2.1). As equation 2.2 indicates, the system's capacitance is proportional to its dielectric permittivity ϵ and plate area A, and inversely proportional to the distance d between the charged plates. Please note, this equation represents an idealized approximation that ignores edge effects. The separator layer is made to be as thin as possible while still maintaining electrical isolation. In practice, these separation distances are on the order of $1\mu m$.

$$Q = CV \tag{2.1}$$

$$C = \frac{\epsilon A}{d} \tag{2.2}$$

Instead of a dielectric separating the two electrodes, a supercapacitor uses an ionic electrolyte to build an electric double layer at the surface of its electrodes. When a differential charge is created on the electrodes of a supercapacitor, ions of correspondingly opposite charge attract to the electrode. Attracted ions diffuse through the bulk electrolyte and ad-

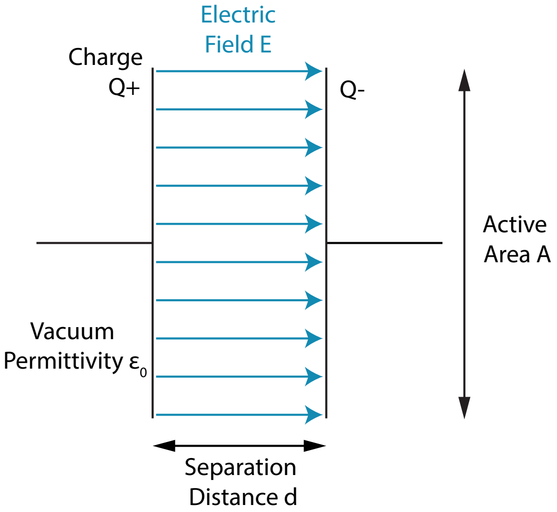

Figure 2.1: Cross section of parallel plate capacitor illustrating energy storage via electric field in vacuum.

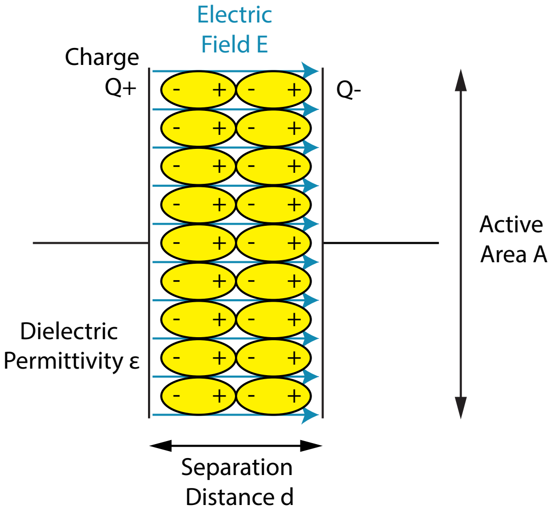

Figure 2.2: Cross section of parallel plate capacitor illustrating energy storage via electric field across a dielectric.

sorb on to the surface of the electrode to create the outer Helmholtz plane (OHP) as seen in figure 2.3. This OHP defines an extremely small separation distance d between the ionic charge and the charged electrode and drives the system's capacitance high via the denominator of equation 2.2. While charge separation distance depends on the exact chemistry of the electrolyte, it is not unreasonable to create a separation distance on the scale of $1nm$.

Additionally, supercapacitors can boost their capacitance be using extremely high surface area materials like activated carbon [71] and graphene to provide large ion adsorption surfaces and increase the numerator of equation 2.2.

Equation 2.3 speaks to the energy storage capabilities of the supercapacitor. By increasing the system's capacitance supercapacitors are able to store magnitudes more energy than its dielectric-only counterpart.

$$E = \frac{CV^2}{2} \tag{2.3}$$

It is important to note the quadratic relationship between the cell's voltage and its energy storage capabilities. The allowable maximum voltage of a supercapacitor is often limited by the breakdown voltage of the electrolyte separating the electrodes. In the case of aqueous electrolytes, this limiting voltage can be as low as 1.0 volts. A supercapacitor's voltage limit is its strongest variable in energy storage capability.

Contrastingly, parallel plate capacitors can usually withstand much higher voltages (some of as high as $100V$). At first glance this would appear to make PPCs more favorable for

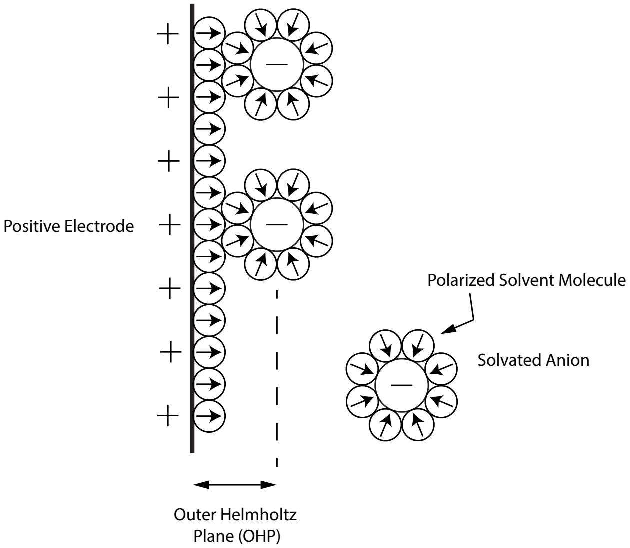

Figure 2.3: Cross section of supercapacitor illustrating energy storage via electric double layer. Only the positive electrode is illustrated here, which constitutes half the double layer.

energy storage, however the practicality of managing an energy reservoir with a large voltage range is very difficult. Charging and discharging from voltages that are drastically different from the end-use voltage incurs efficiency penalties, and requires bulky and expensive voltage regulation.

2.2 Parameter Identification: Electrochemical Impedance Spectroscopy

To predict the behavior of an electric double layer cell, it can be informative to model the system behavior as a low-order equivalent circuit. Figure 6.9 illustrates the first-order circuit of a supercapacitor (sometimes called a Randles cell) that includes series resistance and leakage resistance. Such a circuit exhibits a predictable response over a full range of excitation frequencies, around which a parameter identification experiment can be formulated. Electrochemical impedance spectroscopy subjects the cell to an alternating current excitation program wherein the AC frequency is swept over a controlled range. By observing the real and reactive power across the supercapacitor cell, one can identify the cell's capacitive and resistive parameters.

AC impedance enables the understanding of an electrical component's response to alternating current by considering the real and imaginary components of AC power. The basic elements in AC impedance circuit modeling are resistive, capacitive, and inductive, and their component impedances are expressed as follows:

$$Z_R = R \tag{2.4}$$

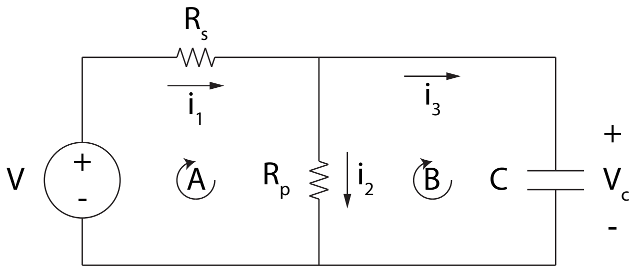

Figure 2.4: First order equivalent circuit diagram of supercapacitor reservoir including series resistance and leakage resistance.

$$Z_C = \frac{1}{j\omega C} \tag{2.5}$$

$$Z_L = j\omega L \tag{2.6}$$

Where Z is the complex impedance of a circuit element, j is the imaginary number $\sqrt{-1}$, ω is the AC angular frequency, R is the resistance in Ohms, C is the capacitance in farads, and L is the inductance in henries.

The AC angular frequency ω (in radians/second) is related to its frequency f (in Hz) by a factor of 2π.

$$\omega = 2\pi f \tag{2.7}$$

A multi-component circuit's impedance can be calculated by first expressing each element in terms of its impedance and then simplifying the circuit as groups of series and parallel impedances. Series impedances are added:

$$Z_s = Z_1 + Z_2 \tag{2.8}$$

Parallel impedances can be combined as the reciprocal of the sum of reciprocals:

$$\frac{1}{Z_p} = \frac{1}{Z_1} + \frac{1}{Z_2} \tag{2.9}$$

The equivalent circuit shown in figure 2.4 simplifies into two parallel circuit elements (R_p and C) in series with a third circuit element (R_s), so the complex impedance of such a circuit is easily derived with the definitions and equations 2.4 through 2.9.

$$Z(j\omega) = R_s + \frac{R_p}{j\omega C R_p + 1} \tag{2.10}$$

Because this equation is written as a function of $j\omega$, it already exists in the complex frequency domain. Familiar frequency domain notation is recognized by replacing the $j\omega$

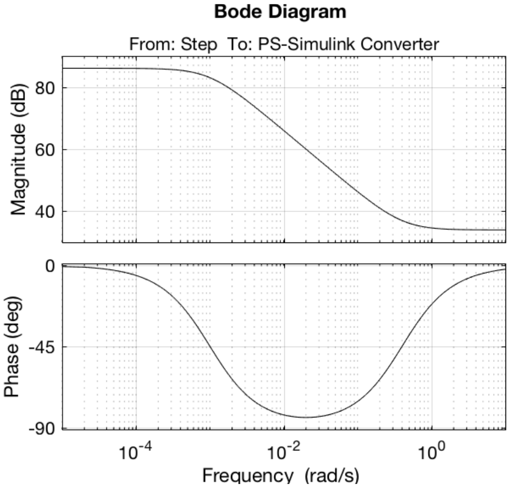

Figure 2.5: Bode plot of equivalent circuit seen in figure 2.4 illustrating its low-pass nature.

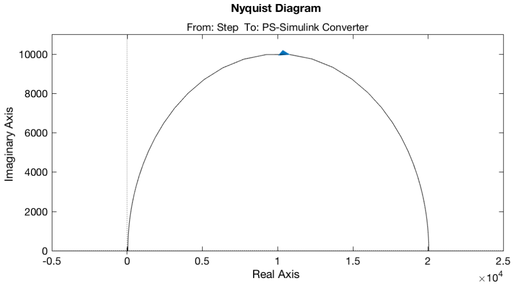

Figure 2.6: Nyquist plot of equivalent circuit seen in figure 2.4 from which we are able to determine the circuit parameters.

with the complex frequency parameter s. Here, equation 2.10 is converted into the familiar transfer function notation indicating one pole and one zero:

$$Z(s) = \frac{R_s s + \frac{R_s + R_p}{R_p C}}{s + \frac{1}{R_p C}} \tag{2.11}$$

Examining equation 2.11 on a Bode plot allows us to see the low-pass nature of this equivalent circuit. Figure 2.5 shows the magnitude and frequency response of an equivalent circuit with values of $R_s = 50$ Ohm, $C = 0.050$ farad, and $R_p = 20,000$ Ohm.

By performing an EIS frequency sweep across a full cell supercapacitor, we are able to experimentally determine its circuit parameters. In figure 2.6, we examine the Nyquist plot representative of 2.4 and are able to identify the values of R_s,R_p, and C by considering the semicircle's intercepts with the real axis, and the angular frequency at the semicircle's largest imaginary magnitude. The value of R_s is found as the smallest magnitude intercept with the real axis. The larger magnitude intercept with the real axis is the sum of R_s and R_p. The angular frequency at the semicircle's peak can be used to determine C as indicated with equation 2.12.

$$\omega = \frac{1}{R_p C} \tag{2.12}$$

It is important to note that experimental measurements of supercapacitor cells will behave like this equivalent circuit at low to mid frequencies, but will exhibit an affine diffusion response at higher frequencies. This more complex system can be expressed as a circuit model containing what is known as a Warburg element (element of constant phase).

2.3 Parameter Identification: DC Charge and Discharge

The simplest way of determining the basic parameters of an electric double layer capacitor is to analyze the current-voltage response of a supercapacitor when subjected to constant current charge and discharge regimes. By controlling the current and measuring the time-based slope of the voltage, the cell's capacitance can be calculated with equation 2.13. By imposing a stepwise change in current, the cell's equivalent series resistance can be calculated with equation 2.14.

$$I = C\frac{dV}{dt} \tag{2.13}$$

$$\Delta V = \Delta I R \tag{2.14}$$

The time progression of voltage is seen in figure 2.7 when a supercapacitor is charged and discharged with constant currents I_1 and I_2 respectively. The supercapacitor starts the experiment with zero charge and zero voltage at time t_0. At t_1 the charging current I_1 is initiated. The cell voltage jumps to V_1 due to Ohmic losses (equation 2.14) across R_s. The charging current is held and the supercapacitor's voltage climbs per equation 2.13 until the final voltage V_f is reached at t_2. At this instant, the current switches to the discharge current of I_2 and the Ohmic drop is seen as the change in current across R_s. The discharge current is maintained while the supercapacitor's voltage falls, again per equation 2.13, until the cell's voltage reaches zero at t_3. At this point the driving current is set to zero and the discharging Ohmic loss is regained, bringing the cell voltage to V_3. Note, the supercapacitor still holds a small amount of charge, as it rests at a non-zero voltage V_3. Due to the Ohmic losses across R_s, the supercapacitor cannot be drained of all stored charge by anything but an infinitesimally small current. This constant current testing procedure enables the tester to identify the supercapacitor's capacitance and series resistance.

Beyond the value of parameter identification, this simple exercise brings to light two important considerations for the practical use of supercapacitors as energy storage. First, the energy efficiency of the charge and discharge cycle is readily observed. The energy cost of charging the supercapacitor is the product of the charge current and the instantaneous voltage integrated over the entire charge step, as is seen in equation 2.15. Because the charge step's Ohmic losses result in a positive voltage, the energy required to charge the supercapacitor incurs a cost for overcoming the cell's series resistance R_s. During discharge, this Ohmic loss is negative and thus, there is a similar cost for extracting energy across the series resistance. The relevant integration range is written in equation 2.16. Because of detrimental Ohmic losses during charge and discharge, the full-cycle energy efficiency (equation 2.18) of a supercapacitor with a non-zero series resistance will always be below 1.

$$W_{chg} = \int_{t_1}^{t_2} IV dt \tag{2.15}$$

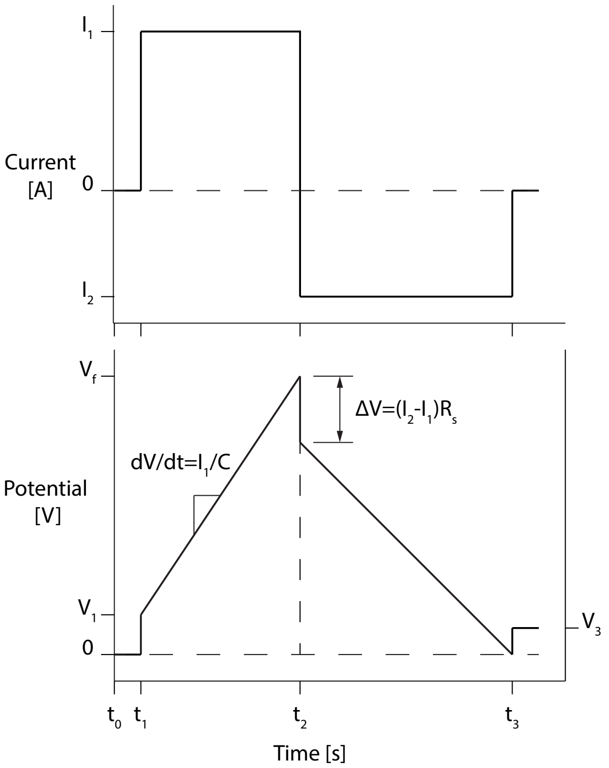

Figure 2.7: Current-voltage response of electric double layer capacitor during constant current charge and discharge regimes.

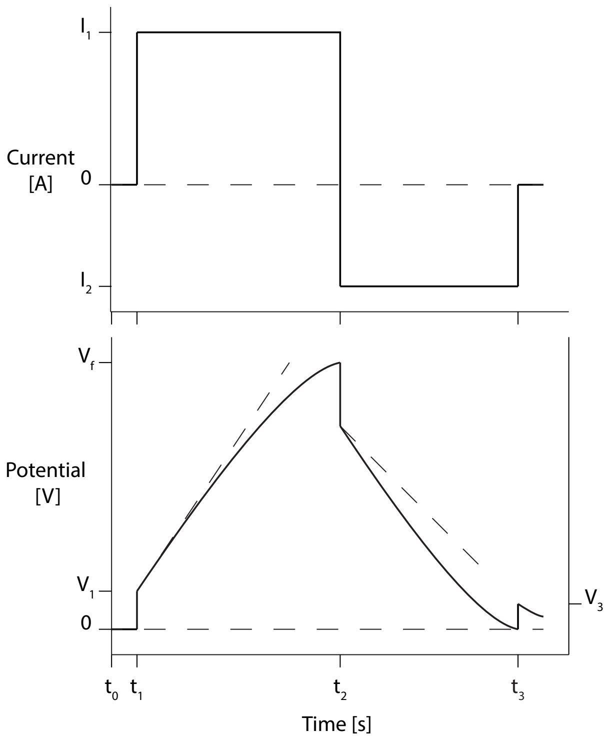

Figure 2.8: Current-voltage response of electric double layer capacitor during constant current charge and discharge regimes. Leakage currents included.

$$W_{dchg} = \int_{t_2}^{t_3} IV dt \tag{2.16}$$

$$\eta_E = \frac{W_{dchg}}{W_{chg}} \tag{2.17}$$

Second, the coulombic efficiency of the supercapacitor is easily identified by considering the integrated charge during the charge step and the integrated charge during the discharge step. Note, because the supercapacitor will have a positive, non-zero voltage after t_3, one must recognize that some charge is still stored in the supercapacitor after discharge has stopped. This charge cannot be extracted from the supercapacitor using the constant current I_2 without driving the cell's voltage to a negative value. This quantity of charge is simply found with equation 2.1.

$$\eta_C = \frac{\int_{t_2}^{t_3} Idt}{\int_{t_1}^{t_2} Idt} \tag{2.18}$$

If the coulombic efficiency is not sufficiently close to one, the supercapacitor could be undergoing faradaic reactions which would falsely characterize the supercapacitor's parameters and potentially limit the life of the cell.

2.4 Leakage

DC charge and discharge testing can identify some basic parameters of the supercapacitor. Figure 2.7 and its relevant equations assumed that the leakage of the supercapacitor is negligible over the timespan tested. In reality, this is not the full story. Leakage across a supercapacitor will increase with the potential across it, so the affine voltage curves during charge and discharge will actually have a slight plateauing shape to them. The current-voltage response of a leaky supercapacitor will exhibit the plateauing shapes seen in figure 2.8. Note, the ideal response is illustrated as dashed lines during charge and discharge. Depending on its magnitude, this leakage current can produce a considerable effect on the cell's coulombic efficiency as electrons lost across the electric double layer during charge and discharge do not contribute to the discharge current. Leaky supercapacitors are not able to maintain their charge after being brought to an elevated voltage, and their voltage will slowly decay as we see at t_3 after the current is brought to $0A$.

Kirchoff's current law

$$i_1 = i_2 + i_3 \tag{2.19}$$

Kirchoff's voltage law around loop A

$$V - i_1 R_s - i_2 R_p = 0 \tag{2.20}$$

Kirchoff's voltage law around loop B

$$i_2 R_p - \frac{1}{C}\int i_3 dt = 0 \tag{2.21}$$

Add equations 2.20 and 2.21 to get

$$V - i_1 R_s - \frac{1}{C}\int i_3 dt = 0 \tag{2.22}$$

Differentiate equation 2.22 in time to get

$$\frac{di_1}{dt} R_s + \frac{1}{C} i_3 = 0 \tag{2.23}$$

Substitute i_3 of equation 2.19 to get

$$\frac{di_1}{dt} R_s + \frac{1}{C}(i_1 - i_2) = 0 \tag{2.24}$$

Substitute i_2 of equation 2.20 to get

$$\frac{di_1}{dt}R_s + \frac{1}{C}(i_1 - \frac{V - i_1R_s}{R_p}) = 0 \tag{2.25}$$

Which simplifies to the standard form

$$\frac{di_1}{dt} + (\frac{R_p + R_s}{R_pR_sC})i_1 - \frac{V}{R_pR_sC} = 0 \tag{2.26}$$

This is a first-order ODE whose general solution takes the form of

$$i_1 = Ae^{-t/\tau} + B \tag{2.27}$$

And whose first time derivative is

$$\frac{di_1}{dt} = \frac{-A}{\tau}e^{-t/\tau} \tag{2.28}$$

By substituting equations 2.27 and 2.28 into equation 2.26 and combining like terms, we can solve for τ, and B.

$$\tau = \frac{R_pR_sC}{R_p + R_s} \tag{2.29}$$

$$B = \frac{V}{R_p + R_s} \tag{2.30}$$

By providing the updated equation 2.26 with the initial condition wherein the stepwise voltage changes from 0 to V, we are able to solve for A. At this instant the capacitor C acts as a short circuit because $\frac{dV}{dt} = \inf$, leaving V to complete its path through only R_s.

$$i_1(0) = \frac{V}{R_s} = Ae^0 + \frac{V}{R_p + R_s} \tag{2.31}$$

$$A = \frac{VR_p}{R_s(R_p + R_s)} \tag{2.32}$$

With constants A and B identified, the final solution takes the form

$$i_1 = \frac{V}{R_p + R_s}[\frac{R_p}{R_s}e^{-t/\tau} + 1] \tag{2.33}$$

Following this process for solving the circuits differential equations, the leakage resistance of a supercapacitor can be identified using stepwise DC methods. The energy storage device approaches steady state and the measured current approaches its DC leakage current. Figure 2.9 illustrates the circuit's time series response to a stepwise voltage input at time 0. Using Ohm's law 2.14, the leakage resistance is readily determined. Because this process acts as

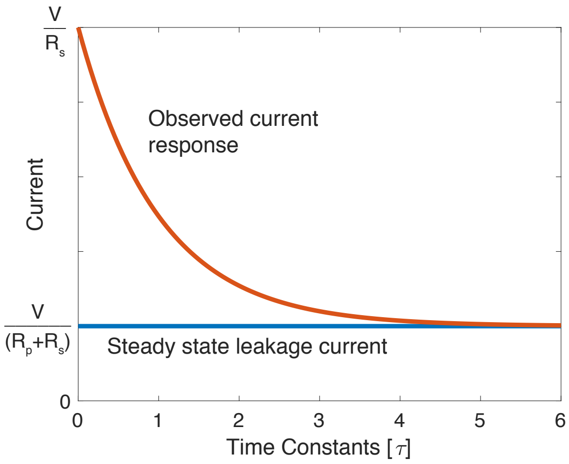

Figure 2.9: Current response of first-order supercapacitor to stepwise voltage input. Observed current exponentially approaches steady state leakage current.

an over-damped oscillator as described in equations 2.10, its time constant is measured on the order of seconds. The cell current's asymptotic approach to steady state follows the exponential curve described in 2.33 and is within 99% of the leakage current after five RC time constants defined by equation 2.29. Time constants for the supercapacitors fabricated in our labs are on the order of 2.5 seconds, so measuring their parameters using DC methods is relatively quick. However, for much larger R_p, R_s, or C, a supercapacitors DC response could be quite slow to reach steady state. For extremely high time constants, a supercapacitor's internal parameters can be identified by measuring its current at any two points along its exponential decay curve and solving for its constants at finite times.

2.5 Power and Energy: Ragone Plots

Supercapacitors often have RC time constants on the order of seconds which makes them ill-suited for high-frequency voltage stabilization. Instead, the high capacitance of supercapacitors makes them very favorable for DC energy storage. Figure 2.10 compares various electrical energy storage technologies including batteries and supercapacitors. Note, battery technologies show higher energy density but lower power densities because they leverage rate-limited chemical reactions while supercapacitors show higher power densities and lower energy densities because their energy storage doesn't involve faradaic reactions. To consider The DC application of interest, a power system designer should first understand the power demands of the load. Once the power demand is established, the energy reservoir's energy enables the system to run for a longer duration.

Power is defined simply as the time derivative of energy, so differentiating equation 2.16 gives us a way to identify the supercapacitor's discharge power.

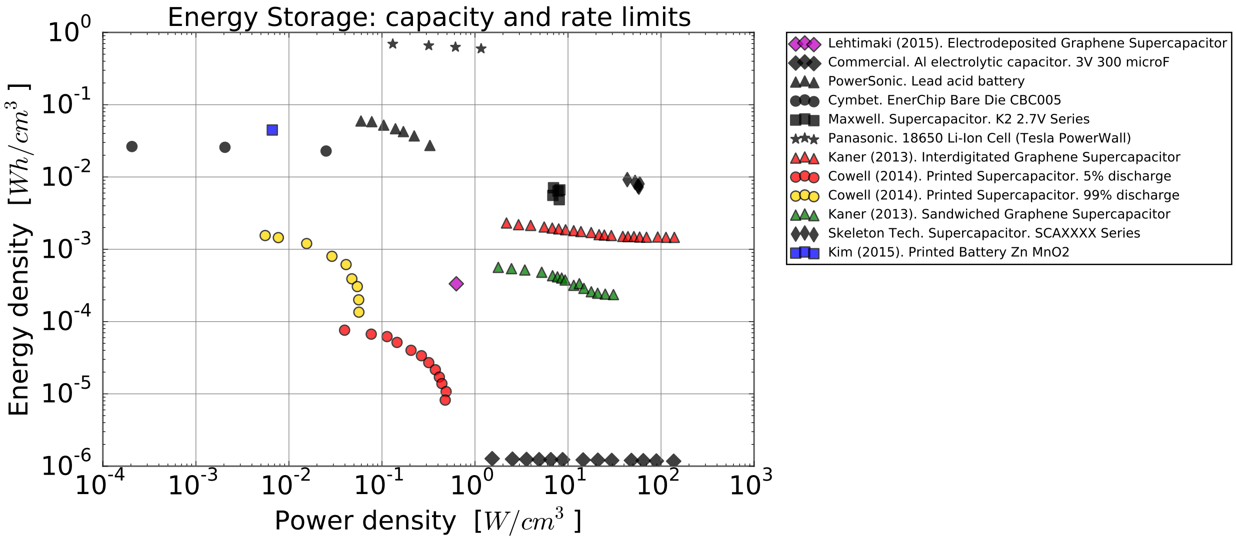

Figure 2.10: Ragone plot comparing energy density and power density of various energy storage technologies

$$P = IV \tag{2.34}$$

If we consider the supercapacitor's entire discharge step from t_2 to t_3, we can identify its average power capability and its full energy capability. This metric is beneficial for an application where the load demand would consume the majority of the stored energy in a supercapacitor. However it is important to note that the supercapacitor's average power capability will not match its power capability at higher voltages. For applications where short duration, high power are necessary, a better metric for understanding a supercapacitor's high upper voltage power capability. The two different performance metrics of a printed supercapacitor can be seen in 2.10 as yellow and red circles respectively. Higher energy is extracted at a lower power by discharging the supercapacitor entirely. Lower energy is extracted at higher power by discharging only the top 5% of the voltage range.

2.6 Energy storage response to Pulse Loads

Portable batteries are the foundation for mobile and wearable IoT devices, and are often the largest single component in such a devices bill of materials. Because traditionally rigid and bulky batteries are infeasible for many wearable and IoT applications, some battery companies have made recent efforts to develop flexible batteries. While these developments have opened new doors for the IoT, product designers have trouble comparing flexible batteries between manufacturers because the field lacks well-established standards for testing and reporting their mechanically coupled electrical properties.

Historical Overview

Many product manufacturers provide customers with specification sheets and safety data sheets that include information relevant to product performance across a range of expected applications and environments. In the battery market, this includes top level information such as nominal voltage and cell capacity that would be important to the average customer, but may include more specialized data on electrical performance or operating conditions that would be important for product designers.

Problems

Battery companies do not have a standardized template or format for battery specification sheets. This makes it difficult for product developers to make an informed and fair comparison of different batteries they may consider for integration into their products. Furthermore, these manufacturers do not clearly describe the methods used in obtaining the properties reported.

Flexible batteries are a new and emerging sector of the market, and have widespread applications. While flexible batteries grant added abilities, their capacity to mechanically deform adds complexity to the evaluation of the devices and their properties. No single method of testing these new properties and their electrical-mechanical coupling has been widely adopted by industry.

The purpose of this investigation was as follows:

1. Review current specifications and standards on the market in order to identify relevant parameters and tests needed for product developers to fairly compare the performance of different batteries, with particular focus on low capacity ($< 250mAh$) and flexible batteries.
2. Determine factors that are relevant to the performance of flexible batteries and assess their relevance for developers.
3. Design a standardized combined safety and specifications sheet that provides product developers with the minimum necessary information needed for a fair comparison of products.
4. Define or identify standardized procedures for obtaining the metrics listed in the standardized specification sheet.

General Approach

A comprehensive specification sheet must be easily understood by readers with little background in battery science. To accommodate this audience, we identified flexible battery parameters that are relevant to battery performance without being esoteric. By making

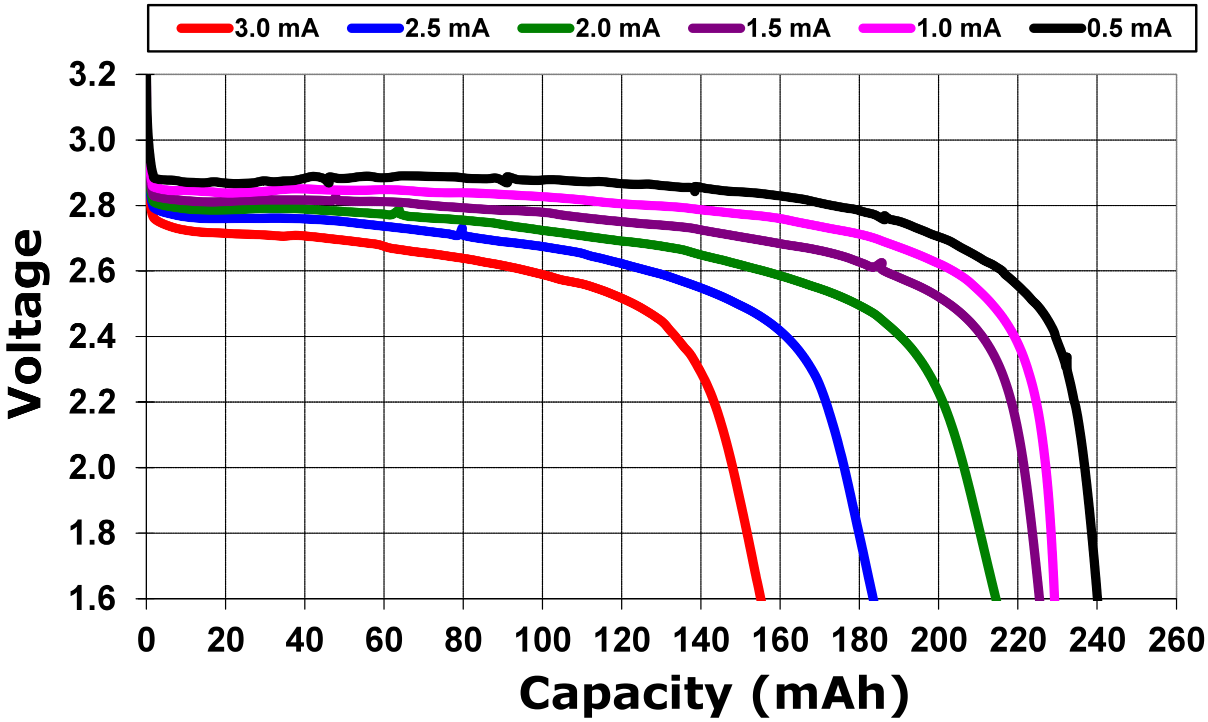

Figure 2.11: Capacity of CR 2032 Batteries discharged under constant current regimes [28]

these simplifications, we enable product designers to easily compare specification sheets between manufacturers and make informed decisions for their product.

A reporting standard for flexible batteries must describe traditional battery metrics in addition to containing details on mechanical properties and mechanically coupled electrical properties. Traditional battery metrics include chemistry, voltage, capacity, dimensions, and safety, while flexible battery metrics must extend to describe how properties like capacity and safety are affected by mechanical perturbations. We identified tests to efficiently quantify these mechanically coupled responses in addition to tests that are relevant to the electrical loads of widely used IoT electronics like radios and sensors.

We developed an expansive list of all factors that are relevant to flexible battery performance in the context of the IoT, which are covered in this document. We outlined the most important tests in the body of this document, and leave the remaining items to be described in future work.

With a finalized list of metrics relevant for a product designer, we created a template for a standardized specification sheet (attached as separate document) that presents the information in a clear and concise way.

Electrochemical Performance

Pulse Discharge

IoT and wearable electronics often leverage wireless communication and power-hungry sensors to perform their unique tasks. These electronics have characteristically high peak current, which is not characterized well by the constant-current discharge tests commonly performed by battery manufacturers (fig 2.11 [28]). Because battery performance characteristics for constant-current discharge conditions are provided on battery specification sheets, product designers make the common mistake of averaging peak currents over low duty cycles to estimate the expected life of their battery powered system. This averaging results in overestimation of their batterys capacity and an unexpectedly short product life. The white paper from the collaboration between Nordic and Energizer ([28]) examines the effect of varying the pulse period, and the pulse amplitude while holding the other variables constant. Figure 2.12 shows the capacity response of holding pulse amplitude constant and varying the pulse period. Figure 2.13 shows the capacity response of holding the pulse period constant and varying the pulse amplitude. In both of these cases, the average load demand over the pulse period matches the corresponding constant current demand from figure 2.11. The comparison of these three figures highlights the importance of considering the load demand's time-dependent character when estimating a battery's life.

To anticipate a batterys response to pulse discharging, the batterys specification sheet must combine the testing parameters outlined above to describe a 4-dimensional pulse-design space which considers the battery in the context of the time-dependent nature of a pulse load demand. This space considers three input parameters: pulse amplitude [mA], rest duration [s], and the circuits Functional End Point (FEP) [V]; and one output variable: battery capacity [mAh]. Armed with a battery specification sheet that covers this design space, the product designer can simply input the pulse power characteristics and voltage regulation requirements of their application to gain accurate insight into the batterys expected life during pulse discharging. Because this space is non-linear, it is important to consider the battery's response to the full spectra of input parameters. Maximizing the usable capacity from a battery is not always as simple as minimizing the pulse amplitude or decreasing the rest duration. By combining figures 2.12 and 2.13 into figure 2.14 we observe the non-linearity more clearly - the greatest capacity exhibits a maximum in the middle of the input parameter ranges. In this case, the greatest capacity was extracted with a pulse amplitude of $30mA$ and a rest duration of $24ms$ even though the tested ranges extend beyond these values.

To measure battery performance for pulse discharging:

1. Identify relevant range of input parameters. [(1) pulse amplitude, (2) rest duration, (3) FEP]. See reference material for relevant ranges.

2. Holding input parameters (1) and (2) constant, cycle cell to failure (or recharge voltage limit). Record current and voltage at change in current amplitude.

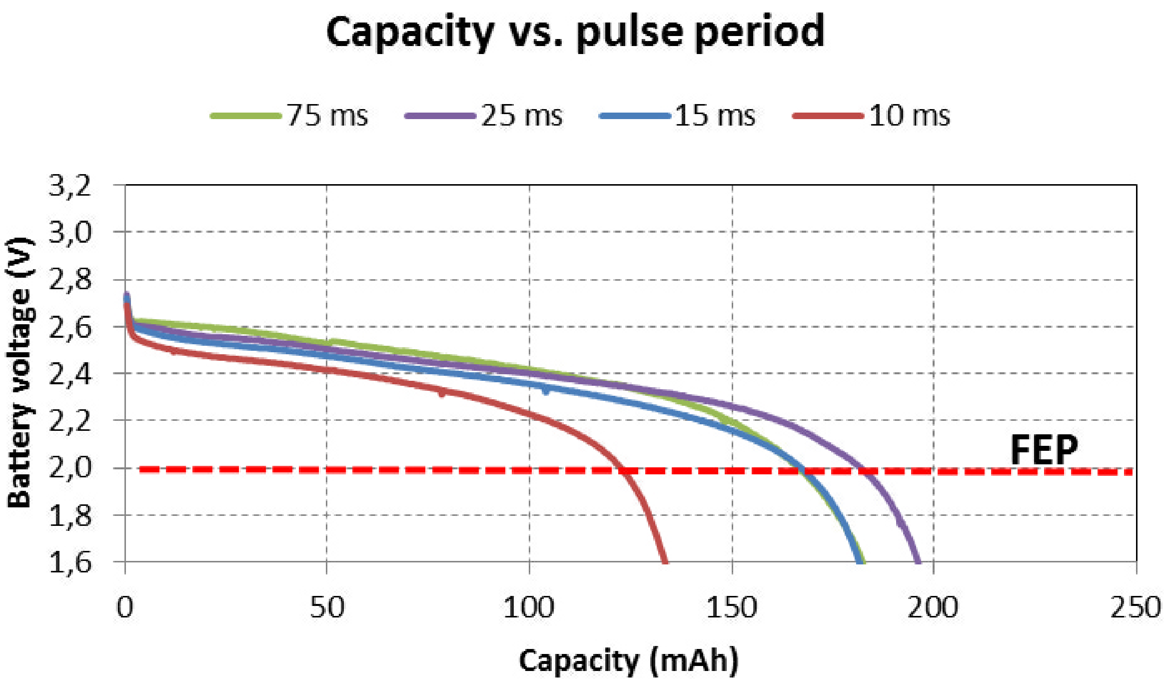

Figure 2.12: CR2032 Battery voltage during 30 mA pulse load [28]. Intersections with FEP indicate battery capacity at full discharge.

3. Recorded data provides datum on remaining parameter (3), and output variable [battery capacity (4)].
4. Recharge or replace cell.
5. Hold parameter (1) constant and vary parameter (2) across relevant range identified in step 1 by repeating steps 2 through 4.
6. Increment parameter (1) through its relevant range and repeat step 5 until the full surface is mapped.

To define a battery-specific surface in this 4-dimensional pulse-design space, a battery manufacturer has two hardware options.

Option 1: Use battery cyclers with have high frequency control and measurement capabilities. This option requires higher capital cost but can be easily customized to cover the full 4-D pulse-design space.

Hardware required: High frequency battery cyclers. Arbin, MACCOR, BioLogic, Ivium, Princeton Tech. (approximately $1500/channel)

Software & Programming: Straightforward continuity between

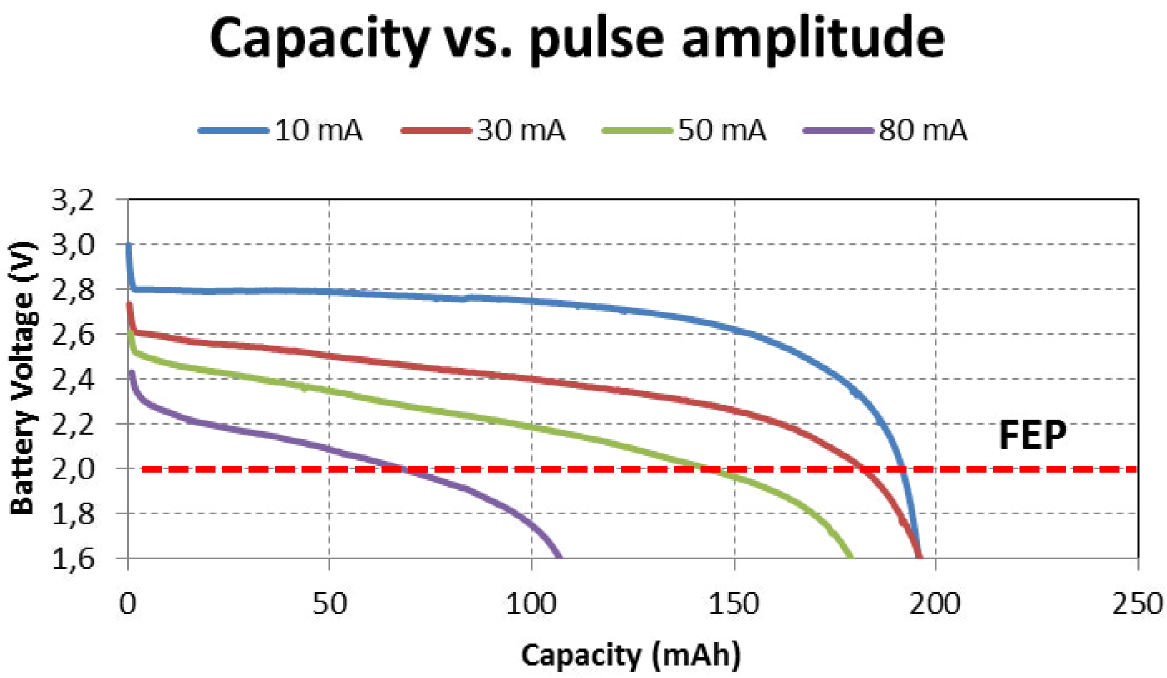

Figure 2.13: Pulse magnitude impact on battery capacity for CR2032 [28]. Intersections with FEP indicate battery capacity at full discharge.

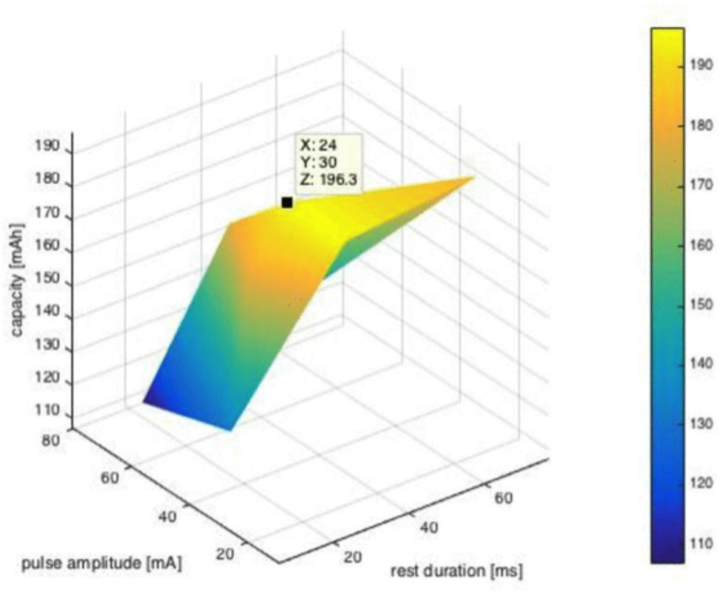

Figure 2.14: Surface describing battery performance in pulse load condition.

Pro: Radio and sensor agnostic. Customizable load profiles allow the battery manufacturer to easily test the full range of variables in surface in the 4-D pulse design space.

Con: High capital cost. Load profile is an approximation of real load profile.

Option 2: Build device-specific development boards out of radios and sensors that will be used in the final product. This option requires low capital cost but sacrifices scalability for the full spectrum of device loads that the IoT and wearable industry covers.

Hardware required: Development boards and sensors in quantities equal to the number of batteries that will be tested in parallel.

Software & Programming: Because the development boards will be running hardware-dependent firmware, the testing agency must be proficient with programming in many languages.

Pro: Low capital cost. Load demand exactly matches end use.

Con: Not scalable hardware. Not easily customizable. Not trivial to cover the entire 4-D pulse-design space.

Continuous Discharge

Constant-current discharge tests are widely accepted in industry as the method for determining battery capacity. Because these standards are already well established we dont suggest making any modifications to these tests. We do, however, recommend that specification sheets provide more comprehensive information on the spectrum of currents that a battery can discharge by providing a range of discharge rates and displaying them on a Ragone plot.

While many battery specification sheets provide the reader with a single number for battery capacity, the rate at which a battery is discharged can have a large affect on battery capacity (mAh). While this single number is accurate for a single discharge current, the relationship between discharge rate and capacity is better described by plotting energy versus power for the batterys discharge rate spectrum. The method described below is used to acquire relevant data for populating a simple Ragone plot. This can be extended into the 3rd dimension of FEP for a more comprehensive understanding of application-specific performance.

1. Identify the range of discharge rates over which the battery will operate.
2. Beginning with a fully charged cell, discharge with constant current until failure (or recharge voltage limit). Record voltage at regular intervals, collecting ¿¿ 100 data points during cycle.

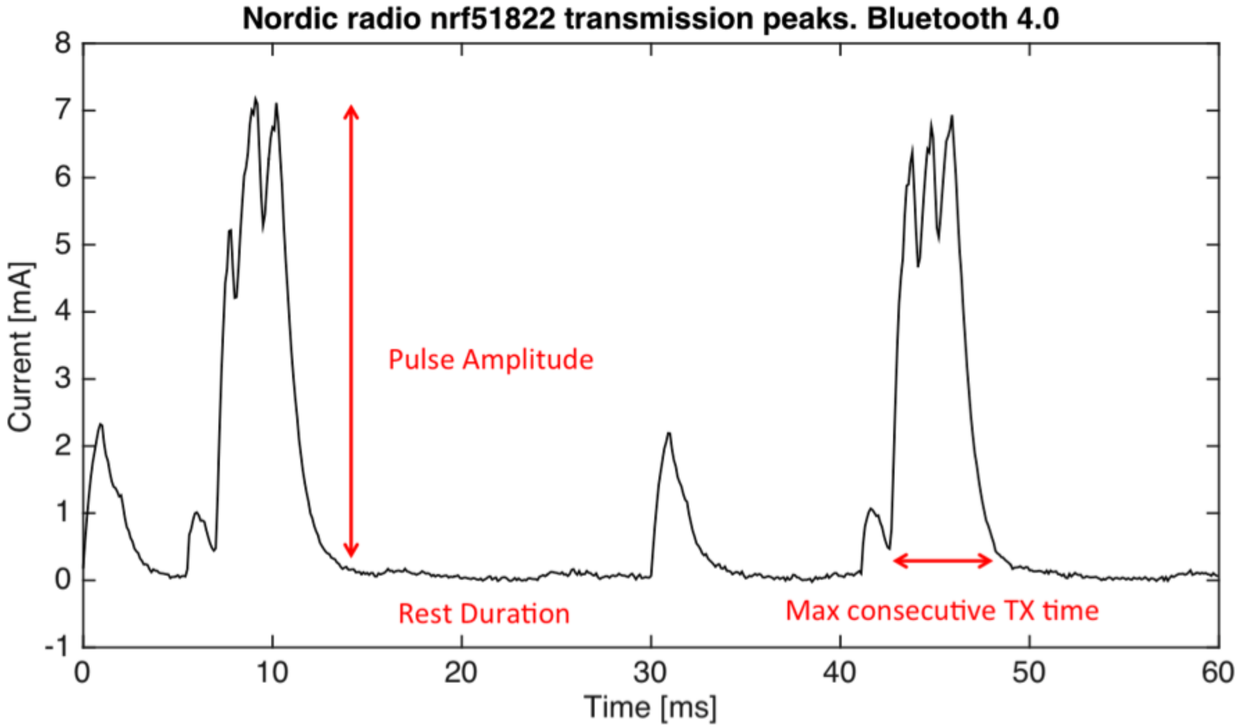

Figure 2.15: Pulse load demand profile

3. Recorded data provides datum on functional end point and discharge capacity.
4. Recharge or replace cell.
5. Increment across relevant current range identified in step 1 by repeating steps 2 through 4 until the full current spectrum is tested.
6. Using the functional end point as the voltage cutoff, calculate the total energy discharged over the cycle as per the trapezoidal summation:
   $E = \frac{I\delta t}{2}\sum_{i=1}^{i_{FEP}-1}(V_i + V_{i+1})$

   Where;

   E is the energy discharged over the cycle

   I is the constant current

   δt is the time step between voltage measurements

   V_i is the measured voltage at index i

   FEP is the functional endpoint

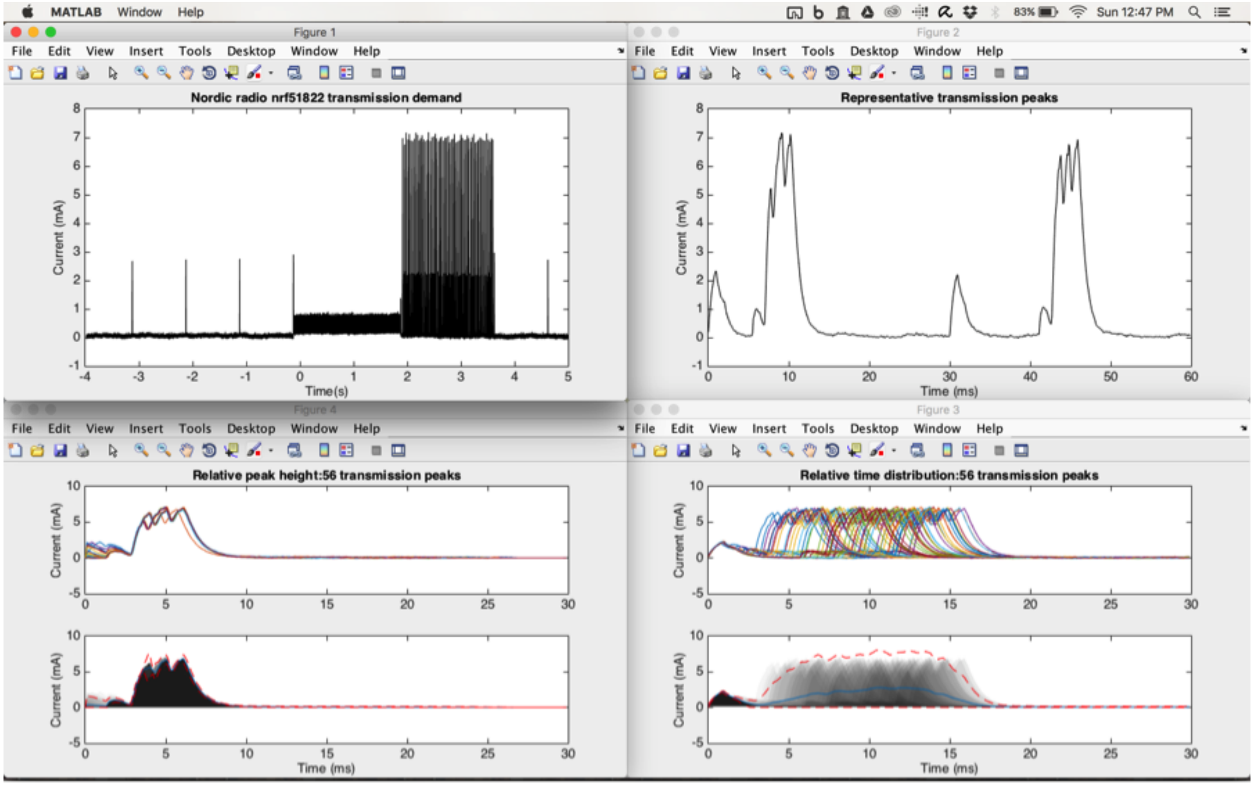

Figure 2.16: Pulse load demand profile. (TL) 56 packet communication demand. (TR) communication protocol magnified. (BL) mean and variance of pulse amplitude. (BR) time spread of pulse peak

7. The average power discharged over the cycle is then simply:

   $P = \frac{E}{\Delta t}$

   Where;

   P is the average power of the discharge cycle

   Δt is the time from cycle start to FEP

Chapter 3

Experimental Work, Fabrication, and Prototyping

3.1 Dispenser printing carbon composite

Powering high-current micro devices with low power generation often found at the micro-scale [4] requires that energy be trickle-charged into a storage device capable of high-current discharge. While arrays of micro piezoelectric vibrational energy harvesters have been used to increase system output power [52], the power required to energize a wireless radio is still much higher [82]. Charge storage via an electric double layer, such as found in a supercapacitor, offers high-current discharging while maintaining long cycle-life performance. The thermal and chemical stability of the ionic liquid electrolyte 1-butyl-3-methylimidazolium tetrafluoroborate ([BMIM+][BF4-]) (BMIMBF4) allows the thick film capacitor to be employed in harsh environments where aqueous electrolytes would otherwise evaporate [17], while the polymer binder allows for structural flexibility.

3.2 Cell Manufacturing

Layer Composition

Symmetrical capacitor geometry was employed with dry electrodes composed of activated carbon (AC), acetylene black (AB), graphite (GR), and poly(vinylidene fluoride-co - hexafluoropropylene) (PVDF-HFP) with mass ratios outlined in table 3.1. Previous work by our lab used mesocarbon microbeads (MCMB) and AB as active electrode materials [36], but

---

Work reported on in this chapter has been published as “Composite carbon-based ionic liquid supercapacitor for high-current micro devices” in the 2014 article of the Journal of Physics: Conference Series 557 by authors Martin A. Cowell, Rich Winslow, Qian Zhang, Jae Bin Ju, James W. Evans, and Paul K. Wright. This work is included with permission.

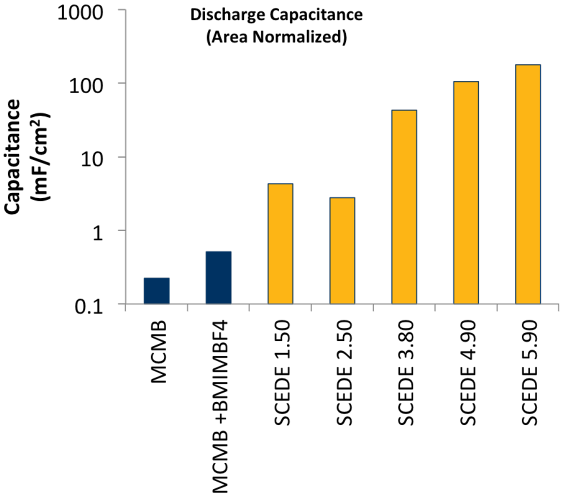

Figure 3.1: Capacitance performance improvements over previous work by leveraging AC, AB, and GR.

Table 3.1: Composite electrode variations. NMP was used to achieve rheology suitable for printing. Note, recipe 5 is the same as recipe 4 but with the addition of IL.

Composite Electrode Version	Electrode Composition AC:AB:GR:PVDF-HFP (Mass Ratio)
1.50	0:1:0:1
2.50	1:0:1:2
2.80	2:0:2:1
3.50	0:9:1:10
4.50	17:1:2:20
5.50	17:1:2:20:18(BMIMBF4)

these have been found to have an average capacitance of $0.50 mF/cm^2$ as seen in figure 3.1. To improve capacitance performance, composite electrodes leverage the high surface area of AC with the electrically conductive microstructure of AB [87] and structural reinforcement of GR. The solvent n-methylpyrrolidone (NMP) was used to suspend the active material and solvate the polymer binder to achieve favorable rheological properties for printed manufacturing.

Recipe code numbers represent the following code:

$$A.BB \tag{3.1}$$

Where A represents the recipe number and whose constituents can be found in table 3.1. BB represents the mass fraction of the ink that is made up of 'active' material. 'Active' material is defined as being non-binder, non-solvent, and non-electrolytic material and in all five recipes is made of the carbonaceous compounds AC, AB, and GR. Figure 3.1 shows the highest performing recipe to be 5.90. Note, Recipe 5 is identical to recipe 4 except it also includes an addition of ionic liquid electrolyte equal to half the mass of the other electrode materials.

The gel polymer electrolyte (GPE) was composed of (50 wt%) PVDF-HFP and (50 wt%) [BMIM+][BF4-]. NMP was also used as a solvent to ensure a printable rheology. The gel polymer layer electrically separated the electrodes while contributing ion migration pathways to support the electric double layer characteristic of supercapacitors.

Layer Dispenser Printing and Assembly

The electrolyte was printed via CNC pneumatic dispenser printer, and electrodes were stencil cast (figure 3.2). They were dried in an oven at 80°C for 12 hours, driving off the NMP to leave only the active and binder materials. Once dry, electrodes were peeled off their stainless steel substrate without damaging their structural integrity. Dried gel polymer electrolyte layers were peeled off their glass substrate (figure 3.3). The dry layers were wetted with [BMIM+][BF4-] and stacked to create parallel-opposed cells (figure 3.4), which were housed in CR2023 coin cells for cycling and performance characterization.

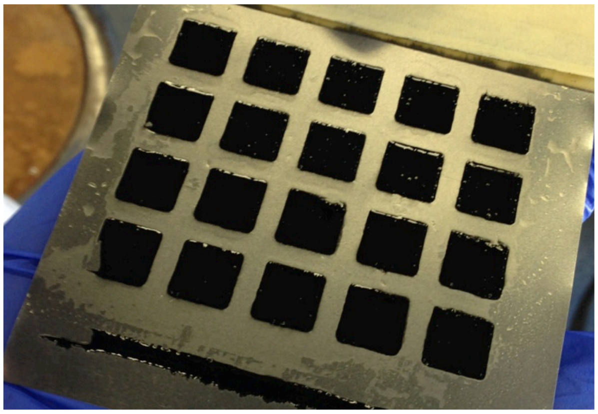

Figure 3.2: Stencil cast electrodes before drying.

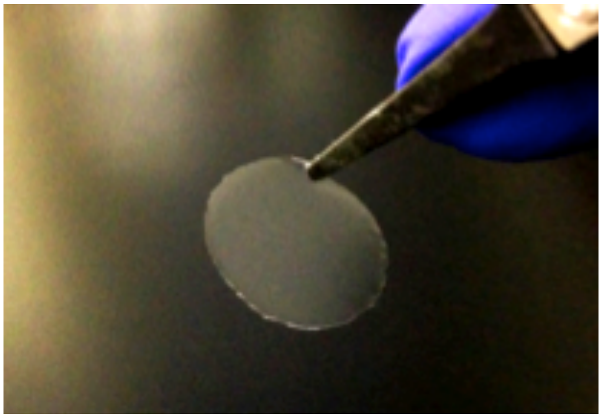

Figure 3.3: Gel polymer ionic liquid electrolyte after oven drying.

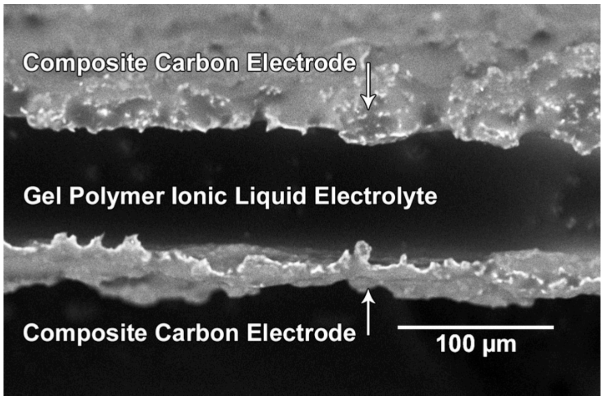

Figure 3.4: SEM of stacked cross section of carbon electrode and GPE.

Table 3.2: Constant current charge and discharge regime.

Step Name	Limit/ Condition
Constant current charge	1.00 V
Rest	5.00 s
Constant current discharge	0.00 V
Rest	5.00 s

3.3 Testing and Performance Results

Short cycle galvanostatic testing was performed on the Gamry Reference 600^{TM}. Constant current charge and discharge cycling was performed as outlined in supercapacitor testing standard IEC 62391-1:2006 [14]. During this cycling regime supercapacitors were looped ten times through steps outlined in table 3.2.

Energy was quantified via numerical integration of the voltage-current product vs. time curve during charging and discharging described by

$$W = \sum_{t=t_o}^{t_f} I_t V_t \Delta t \tag{3.2}$$

where I_t is the time series current in amperes, V_t is the time series voltage in volts, Δt is the time step between samples in seconds, t_f and t_o are the final time and initial time in seconds.

Power during charge and discharge was quantified by

$$P = W/(t_f - t_o) \tag{3.3}$$

Bulk capacitance was calculated using the time rate of change of voltage relation between current and capacitance, based on states at the beginning and end of charge and discharge:

$$C = I(t_f - t_o)/(V_f - V_o) \tag{3.4}$$

where I is the average current in amperes, V_f is the voltage at the end of the charge or discharge step, and V_o is the voltage at the start of the charge or discharge step.

Equivalent series resistance (ESR) was calculated using Ohm's law for voltage drop seen at the transition between charge, rest, and discharge steps:

$$ESR = (V_{o-1} - V_o)/I \tag{3.5}$$

where V_{o-1} represents the voltage immediately before charging or discharging begins. The voltage drop across the cell becomes substantial at higher discharge rates.

Coulombic efficiency was defined as

$$\eta_C = \sum_{t=t_o}^{t_f Discharge} I_t \Delta t / \sum_{t=t_o}^{t_f Charge} I_t \Delta t \tag{3.6}$$

where the number of coulombs transferred was determined through numerical integration of current-time series data.

Energy efficiency was defined as

$$\eta_E = W_d/W_c \tag{3.7}$$

where W_d represents the discharge energy in joules and W_c represents charge energy in joules.

Figures 3.5 and 3.6 show data taken from a cell whose electrodes (1 cm x 1 cm each) were composed of composition 2.80 and separated by a single layer of GPE 60 μm thick. The cell was subjected to constant current charge/discharge regimes using the same magnitude of current during charging and discharging steps (10 and 1000 μA/cm^2 for the two tests). The high voltage limit of 1.0 V was selected to avoid the possibility of side reactions associated with the electrolysis of trace water, but the cells were expected to be able to sustain voltages of 2.5 V to 4.0 V without breakdown of the ionic liquid electrolyte [3]. Results from the two tests are shown in table 3.3. Performance metrics were normalized by a footprint area of 1 cm^2.

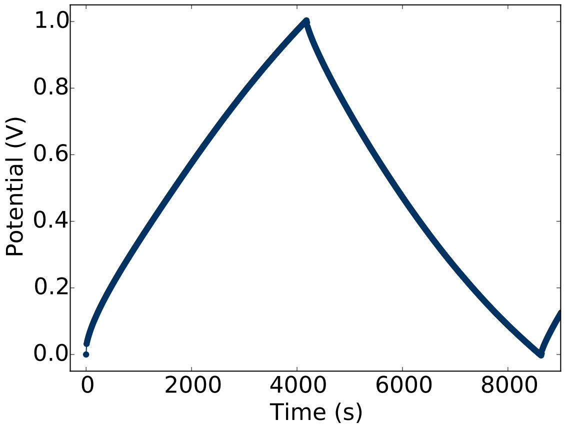

Figure 3.5: Constant current (10 μA/cm^2) charge/discharge voltage response of supercapacitor cell using electrode composition 2.80.

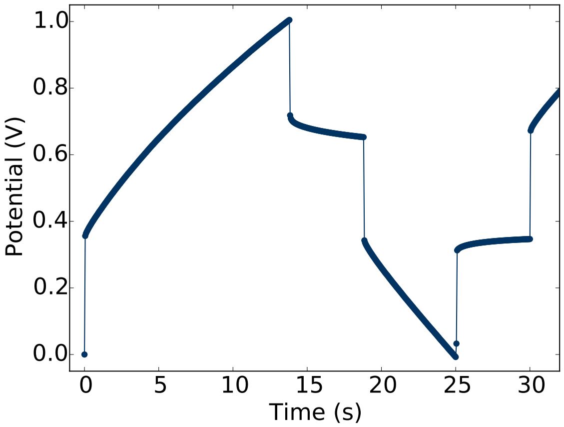

Figure 3.6: Constant current (1000 μA/cm^2) charge/discharge voltage response of supercapacitor cell using electrode composition 2.80.

As is evident in table 3.3, the testing regime heavily influenced the performance of the supercapacitor cell. The highest reported discharge energy density (5.03 μW-hr/cm^2) and discharge capacitance density (43.0 mF/cm^2) were attained by composition 2.80 at a discharge current of 10 μA/cm^2; discharge power density (404 μW/cm^2), composition 1.50 at 1000 μA/cm^2; lowest reported discharge ESR (79.0 Ohms), composition 2.50 at 1000 μA/cm^2; highest reported coulombic efficiency (100%), composition 3.50 at 1000 μA/cm^2; and highest reported energy efficiency (84.2%), composition 1.50 at 50 μA/cm^2. (Please note the 100% coulombic efficiency is accurate to three significant figures, and does not represent perfect charge transfer.)

Long cycle life testing of 100,000 cycles was performed on the cell containing electrode composition 2.80. Figure 3.7 illustrates the cell's capacitance degradation versus cycle number (points plotted for every 1,000 cycles). The cell's capacitance degraded from 28.5 mF/cm^2 to 17.9 mF/cm^2 over the course of the test, a decrease of 37.0%. Note, however, that the

Table 3.3: Performance metrics of supercapacitor cell containing electrode 2.80 tested at two different current densities.

	10 μA/cm^2		1000 μA/cm^2	
	Charge	Discharge	Charge	Discharge
Energy (μW-hr/cm^2)	6.75	5.03	1.61	0.300
Power (μW/cm^2)	5.46	4.26	855	164
Capacitance (mF/cm^2)	45.0	43.0	20.4	18.0
ESR (Ω)	1020	1150	325	307
Coulombic Efficiency (%)	95.4		97.5	
Energy Efficiency (%)	74.4		18.7	

largest drop (22.5% down to 22.1 mF/cm^2) occurred between cycle number 1 and 1,000, suggesting an initial "break-in" process occurred within the capacitor's first thousand cycles. Once the capacitor was "broken-in," the long cycle life capacitance only dropped by 14.5% over the course of the last 99,000 cycles.

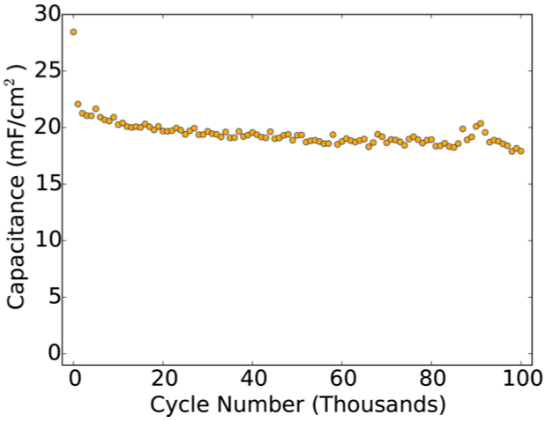

Figure 3.7: Long cycle life effects on cell capacitance

A high-current printable supercapacitor of composite carbon electrode composition employing gel polymer ionic liquid electrolyte has been shown to provide excellent discharge power to support trickle charging provided by micro-scale energy harvesters. This strong attribute promises to pair with micro-energy harvesting devices to meet the demands of high power devices, such as modern wireless radios, for applications in printed flexible wireless sensor nodes. The printing process employed can be rapidly scaled up for high-throughput manufacturing of printed energy storage to be integrated with MEMS device solutions.

Experimental testing reached a maximum voltage of 1.0 V and achieved a discharge efficiency of 84.2%, discharge power of 404 μW/cm^2, and discharge energy of 5.03 μW-

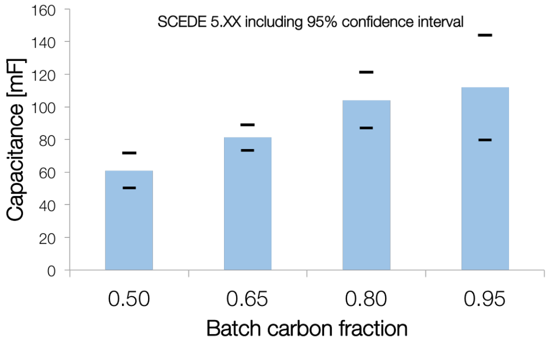

Figure 3.8: Confidence of supercapacitor mean capacitance while varying active fraction.

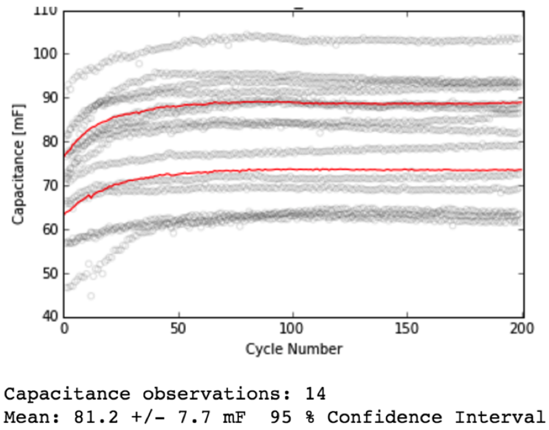

```
Capacitance observations: 14
Mean: 81.2 +/- 7.7 mF  95 % Confidence Interval
```

Figure 3.9: 95% confidence interval of mean capacitance as a function of cycle number.

hr/cm^2. Long cycle life testing of up to 100,000 cycles showed no sign of precipitous cell degradation.

Previous work confirmed a proof of concept for the printability of carbon based ionic liquid supercapacitors but left composition optimization and manufacturing process control unfinished. The research presented in this chapter improves upon the proof of concept with a composite carbon electrode to achieve higher capacitance, energy, and power density.

Dispenser printing, at least with the pneumatic control that the lab printer uses, has its drawbacks. For instance, the layer thickness is a function of the ink viscosity, the dispensing pressure, and the x-y speed. This indirect control results in poor control over the thickness of the deposited layer and thereby the mass of active material present in each electrode. Figure 3.8 summarizes an experiment performed that examined the repeatability of printed supercapacitors by calculating the mean capacitance for samples across populations with varying active fractions. Population active carbon fraction varied from 0.50 to 0.95. While the experiment was originally designed to consider 16 samples of each population, practical issued prevented all the samples from functioning properly. As a result, there were fewer samples collected to represent some populations. To properly correct for small sample sizes, the 95% confidence interval of the population mean was calculated using the student t-test distribution.

Figure 3.9 displays the tested cell capacitance as a function of cycle number for samples in the 0.65 active fraction population. The figure illustrates the high variability of cell capacitance. Each cell displays a consistent behavior, but the variation between cells is very high.

By considering the overlap between confidence intervals across the samples examined, we cannot say with statistical certainty that the populations are different. The only interval that does not overlap with the others is the confidence interval of the mean capacitance for

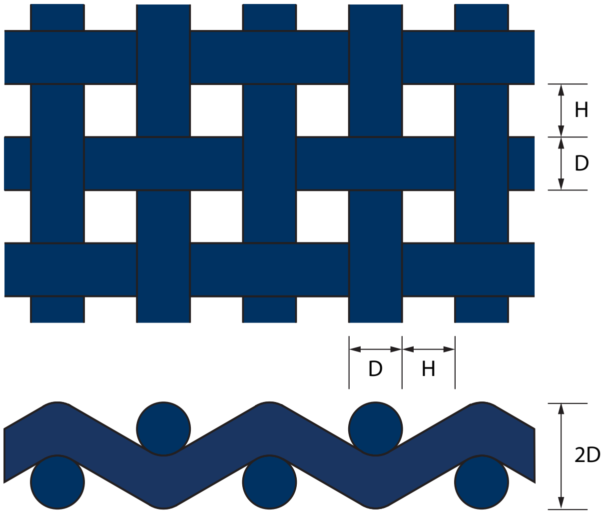

Figure 3.10: Illustration of the cross-hatching pattern of printing screens.

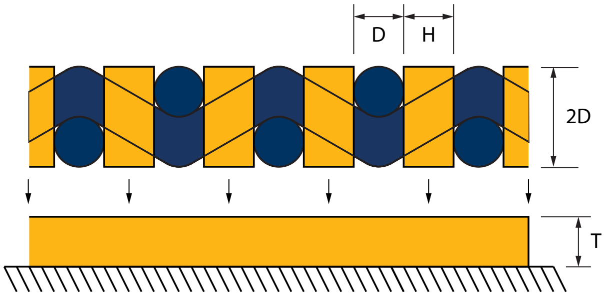

Figure 3.11: Illustration of screen loaded with ink and subsequent wet-layer on substrate.

the 0.50 active fraction population. This poor repeatability provides motivation to consider more repeatable manufacturing techniques.

3.4 Screen printing and carbon composite

While dispenser printing has proven effective for manufacturing small quantities of printed supercapacitors, the method is inherently slow and prone to variations in layer thickness as inferred from 3.8. Screen printing promises to allow higher throughput and more consistency in controlling layer thickness.

Screen design

The performance of a screen for screen printing is inherently built into the parameters and properties of the screen's mesh. Because these parameters are locked in once a screen is fabricated, careful calculation is required when designing a screen for printing electronics. Beyond the footprint pattern, the designer must consider the desired wet-layer thickness and the minimum in-plane feature size. These output characteristics are calculated by considering the mesh diameter and the open fraction as illustrated in figure 3.10. In this figure, the mesh cross-hatching is symmetric across the 45° axis. Figure 3.11 illustrates ink flowing through the screen and being deposited as an ideal rectangular cross-section.

The wet-layer thickness T is a derived from conservation of volume from the openings in the screen mesh.

$$T = \frac{2DH^2}{(D+H)^2} \tag{3.8}$$

The pattern's minimum resolvable feature size F_{min} is limited by the self-leveling of the ink after passing through the screen mesh, and is calculated as the total thickness of the screen including the thickness of the emulsion over mesh (EOM). Emulsion over mesh is the thickness of the mask emulsion layer. This layer enables complex geometries to be designed into the screen footprint, and has a non-zero thickness.

$$F_{min} = 2D + EOM \tag{3.9}$$

Screen labeling nomenclature is standardized in the format of A-M/D, where A is an abbreviation of the material type, M is the thread mesh count in $threads/in$, and D is the thread diameter in μm. Initial screen testing for ink compatibility was performed using the Dynamesh BS-500/18 screen mesh. In this case, BS stands for Asada Hardmesh-Type medium strength stainless steel. This screen's geometrical parameters are 500 threads per inch and thread diameter of 18 micrometers.

Converting from mesh count to hole length H as shown in 3.10 is done with the simple geometric conversion of equation 3.10, wherein the thread diameter D and the hole length add to the repeating unit length along the mesh count. Note, the units are not accounted for in this equation.

$$M = \frac{1}{D+H} \tag{3.10}$$

Profilometry measurements of Layer Thickness

Layer thickness measurements were done on a Dektak profilometer which physically drags a tiny needle tip over the surface of the printed device. Damage to the surface is avoided by precisely controlling the force applied by the needle tip within the Dektak software. As the needle tip deflects over the the surface of the printed layer, its height is measured and reported as a series of height points above the surface of the substrate.

As mentioned above, the screen used for these initial tests was the Dynamesh BS-500/18, which has the following characteristic dimensions and parameters:

$$D = 18\mu m$$

$$H = 32.8\mu m$$

$$EOM = 17.5\mu m$$

$$T = 15.1\mu m$$

$$F_{min} = 53.5\mu m$$

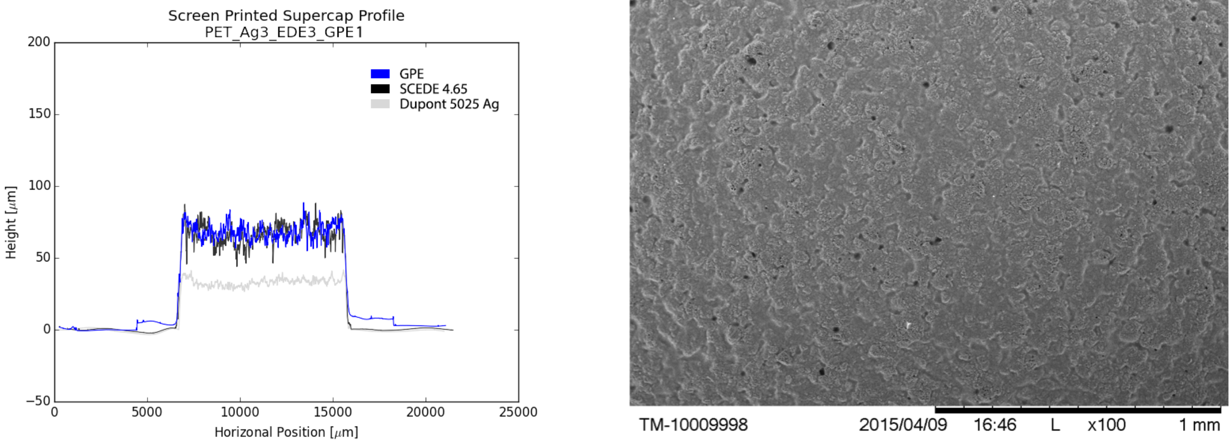

Figure 3.12: One sub-layer of GPE. Note high GPE surface porosity. The legend shows three layers: GPE (Gel Polymer Electrolyte), SCEDE 4.65 (Supercapacitor electrode recipe 4, 65% carbon fraction), and Dupont 5025 Ag (Commercially available silver ink)

To measure the thickness of each layer within a fully screen-printed five-layer supercapacitor, profilometry measurements were made between the printing of each layer. The layers measured here were fabricated by printing many thin sub-layers of the same material to form a final layer of adequate thickness. The wet-layer thickness of 15 microns will provide thinner layers once the ink solvent is evaporated.

The current collector layer is printed with commercial silver ink. These tests used Dupont's 5025 Silver Conductor ink which has a solid loading of 68-72%. When this solid load is left after curing, the BS-500/18 screen's dry-layer thickness will be 10.6 microns. Three sub-layers of silver ink were printed on top of one-another to build a current collector layer thickness of approximately 30 microns.

The electrode layer's thickness contributes primarily to the cell's capacitance, as a thicker layer provides greater active material to for participation in the electric double layer. Controlling this layer's thickness is important for controlling the repeatability of the output devices. Three sub-layers of electrode ink were used to provide an electrode thickness of approximately 30 microns.

The gel polymer electrolyte (GPE) layer's thickness is critical for maintaining electrical separation between the two electrodes. An inadequately thick GPE layer will enable a physical breach and a subsequent electrical short. This layer's thickness is therefore a critical dimension which must maintain a minimum threshold value. Because the electrode inks contain the same solvents and binders as the electrode inks, the GPE layer thickness did not increase proportionally to the number of sub-layers printed. Instead, initial sub-layers act to fill pores in the electrode base layer below. Filling these holes and smoothing the surface acts to reduce the thickness-stacking effect that is necessary to build an adequately thick GPE layer.

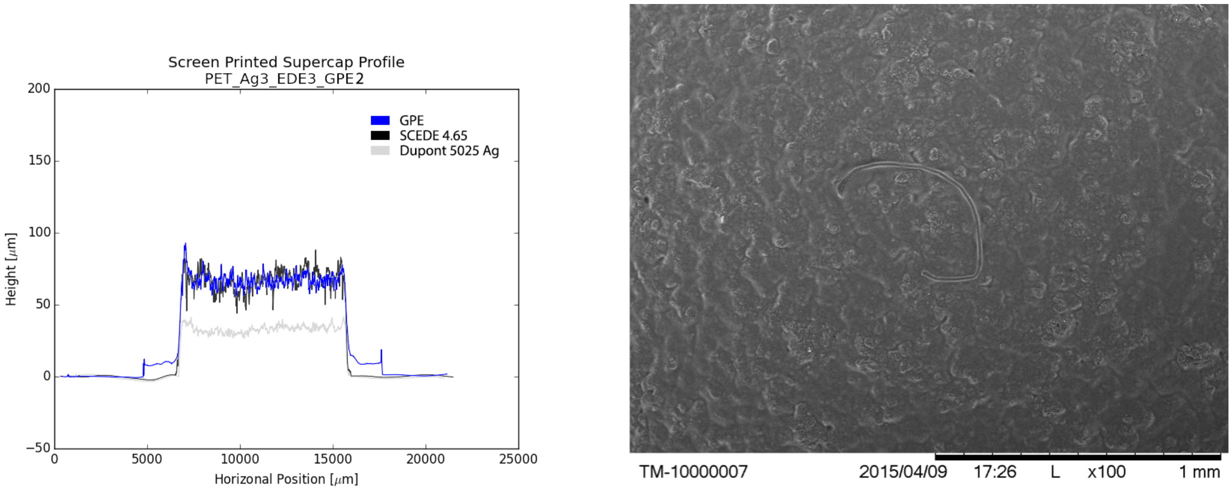

Figure 3.13: Two sub-layers of GPE. As layers accumulate, surface porosity is filled in.

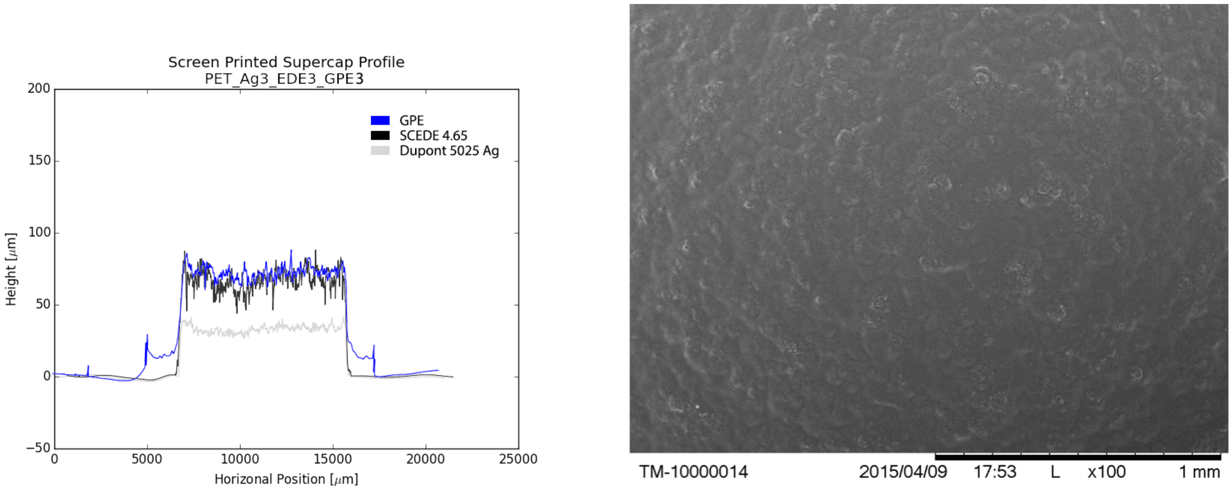

Figure 3.14: Three sub-layers of GPE.

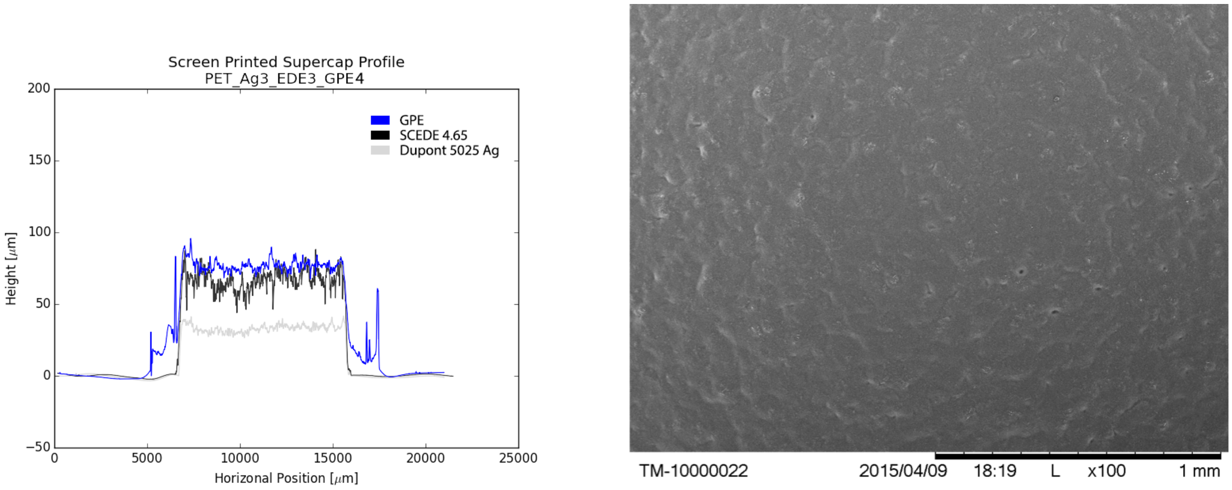

Figure 3.15: Four sub-layers of GPE.

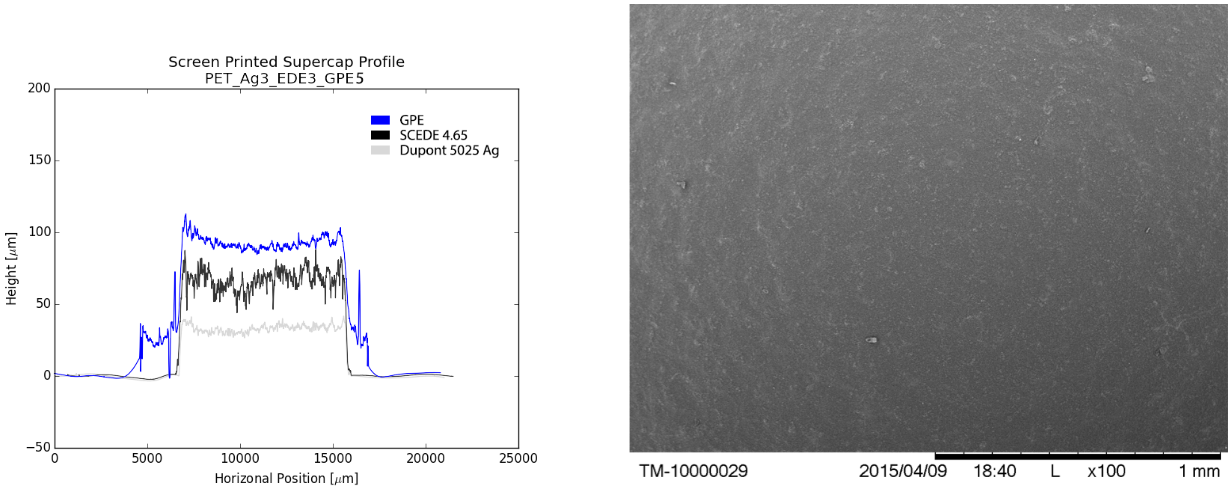

Figure 3.16: Five sub-layers of GPE. Greatest layer thickness and smoothest surface - indicative of best electrically isolating layer.

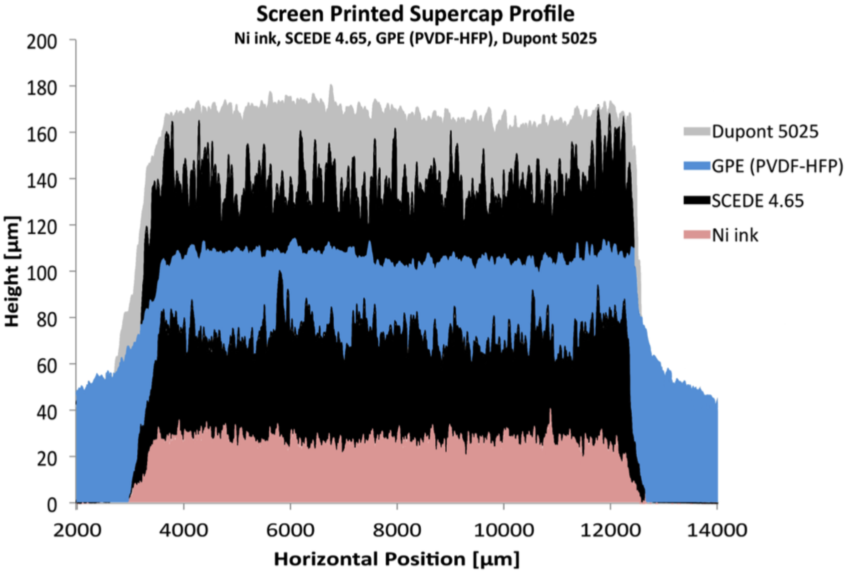

Figure 3.17: Layer-resolved cross section profile of fully screen printed supercapacitor.

Figures 3.12 through 3.16 show the progression of GPE layer thickness as five sub-layers are printed and cured on top of the current collector and electrode stack. The first sub-layer seen in 3.12 results in a very thin total GPE thickness, a highly porous surface, and an insufficient electrical insulation. Subsequent sub-layers of GPE begin to fill in the surface pores, but only marginally add to the GPE layer thickness. Once the pores are filled and the surface roughness is reduced, additional GPE sub-layers contribute to a marked increase in GPE layer thickness. This effect is most noticeable between sub-layers 4 and 5 seen in 3.15 and 3.16.

The final layer configuration is seen in 3.17, wherein the second electrode layer and second current collector layer are printed on top of a sufficiently thick electrode layer. This figure shows a nickel current collector printed on the bottom layer. This nickel layer does not negatively affect the subsequent GPE thickness.

3.5 Arrays of Supercapacitors

Because a screen printing screen cannot be easily modified after it is manufactured, a print designer is constrained to a single ‘footprint’ design for each set of screens. It is at the stage of drawing up the screen’s footprint that the designer has the greatest opportunity to leverage their creative freedom toward accomplishing the end goal simply and concisely.

In the research setting of the university, it is often important to manufacture devices in a way that provides the greatest application flexibility. Printed devices must be manufactured quickly and repeatably, and the devices must integrate easily with future projects as yet unknown. To support statistical evaluation, the designed set of supercapacitor screens to provides large sample sizes (96 unit cells per print). But the greatest creative achievement of this set of screens was designing the electrical connections to be series and parallel configurable by way of a simple cutting procedure. With this critical consideration, my supercapacitor screen design enables application-specific electrical customization while using a single set of screens.

The key consideration for enabling electrical customization lies in the current collector screen's asymmetric traces. By printing the bottom current collector layer in the orientation seen in figure 3.18, and the top current collector rotated 180°, the asymmetric traces are laid beside one another. The two-abreast trace placement shown in figure 3.19 enables the traces to maintain electrical isolation while making them easily accessible for post-print cutting. As printed, the trace patterning produces a full sheet of electrically parallel unit cells. Assuming identical unit cells, the full sheet of parallel unit supercapacitors will have parameters as follow from equations 2.8 and 2.9:

$$C_{total} = nC_{unit} \tag{3.11}$$

$$R_{s-total} = \frac{R_{s-unit}}{n} \tag{3.12}$$

$$R_{p-total} = \frac{R_{p-unit}}{n} \tag{3.13}$$

Where n is the number of involved cells. R_{s-unit} and R_{p-unit} are the unit cell's series and parallel resistance respectively. $R_{s-total}$ and $R_{p-total}$ are the full sheet series and parallel resistance. C_{unit} and C_{total} represent the capacitance of the unit cell and the full sheet respectively.

The customizability of the sheet is fully realized if the application requires supercapacitors with a combination of parallel and series electrical connections. By selectively cutting alternating traces of the top and bottom layers as indicated in figure 3.20, the unit cells are isolated into electrical series. Assuming identical unit cells, the full sheet of series unit supercapacitors will have parameters as follow from equations 2.8 and 2.9:

$$C_{total} = \frac{C_{unit}}{n} \tag{3.14}$$

$$R_{s-total} = nR_{s-unit} \tag{3.15}$$

$$R_{p-total} = nR_{p-unit} \tag{3.16}$$

The detail figure 3.21 illustrates a single row of supercapacitors whose traces are cut to produce the electrical series configuration. Let's follow the the electrical path from the top of unit cell 1 to the top of unit cell 8 to verify that the cutting pattern produces cells in electrical series. Starting at the top of unit cell 1 (TUC1), the circuit continues into the page through supercapacitor cell 1 to the bottom of unit cell 1 (BUC1). From here, a blue trace connects the BUC1 to the BUC2. The circuit then continues out of the page through

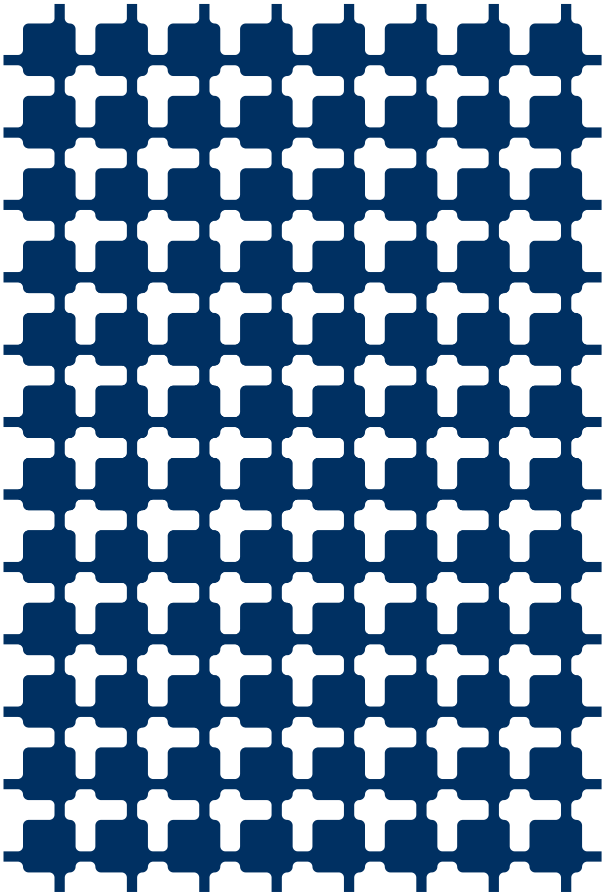

Figure 3.18: Bottom layer of asymmetric trace design.

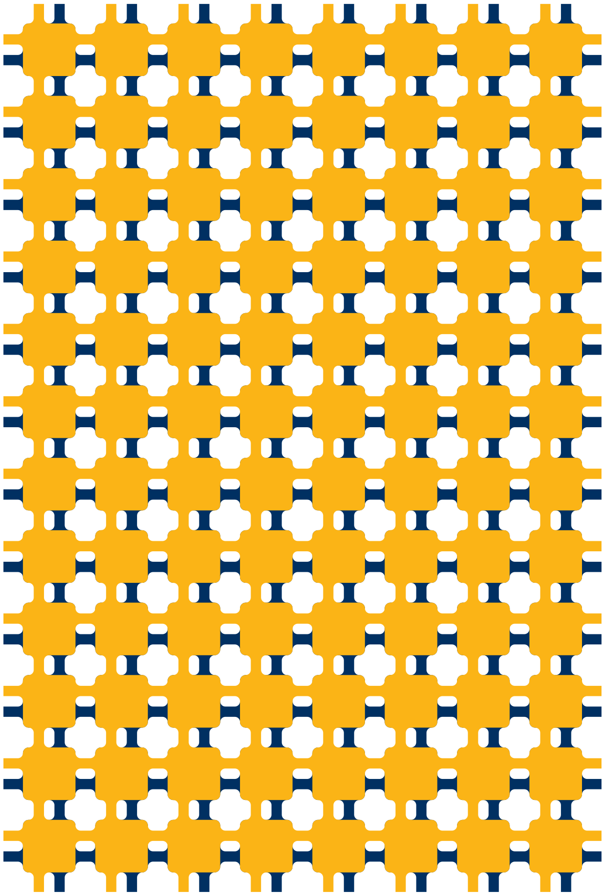

Figure 3.19: Top and bottom layers of asymmetric trace design. The yellow top layer is the same pattern as the dark bottom layer, just rotated 180°.

supercapacitor cell 2 to the TUC2. Now, the yellow trace connects the TUC2 to the TUC3. By continuing this procedure, we follow the alternating asymmetric traces into and out of the page all the way to the top of unit cell 8. This simple string of unit cells was converted from parallel electrical connection to series electrical configuration by simply cutting alternating asymmetric traces.

It is important to note that this electrical series configuration is only available for energy storage components that use symmetric electrodes. Each unit cell alternates in polarity as the circuit passes into and out of the page across each supercapacitor. The supercapacitors discussed in this dissertation contain symmetric carbon electrodes, and are therefore able to capitalize on this customizable series and parallel cutting technique. The asymmetric electrodes used in a battery, however, prevent the series configuration from being viable because the unit cell potential is created and canceled every time the circuit passes into and

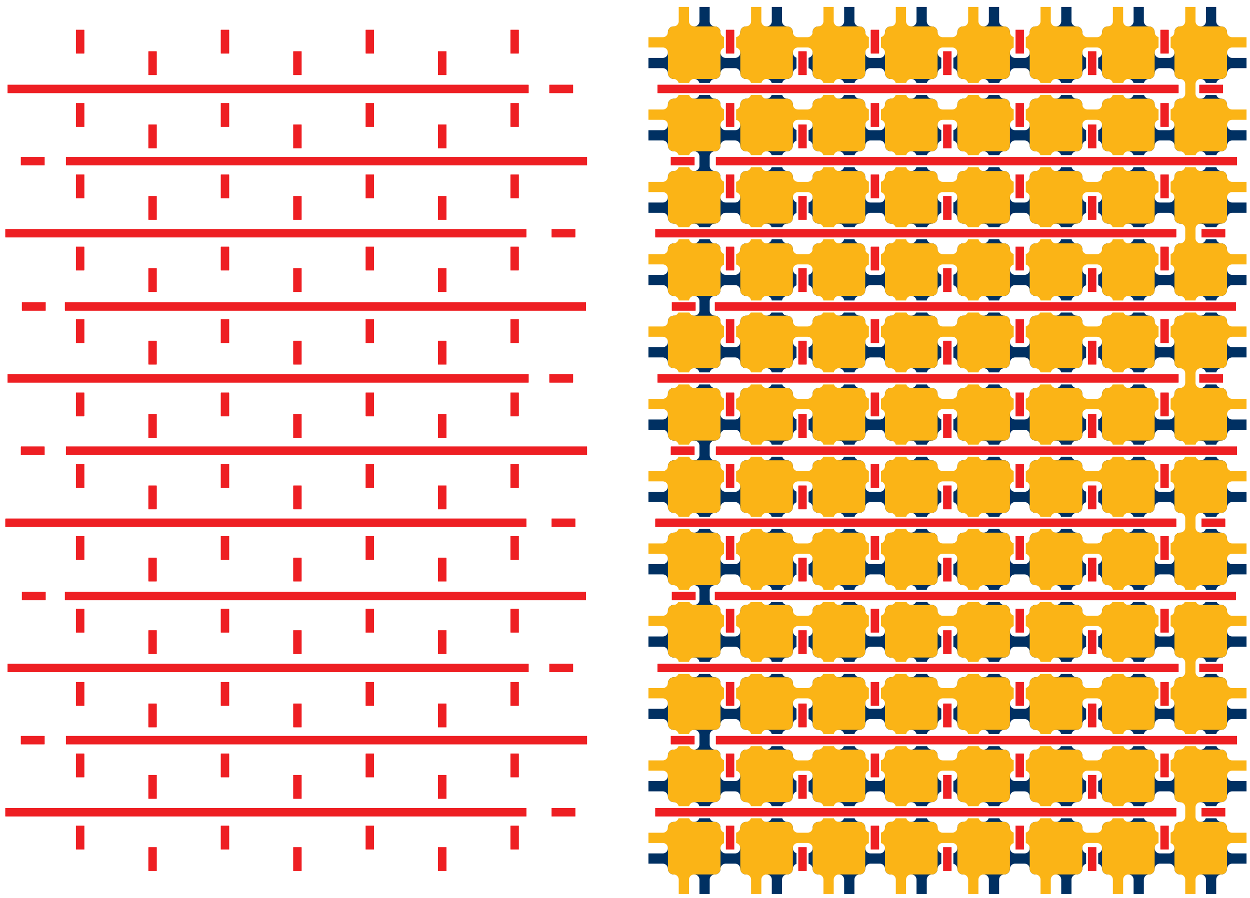

Figure 3.20: Cut pattern to convert cells into electrical series configuration.

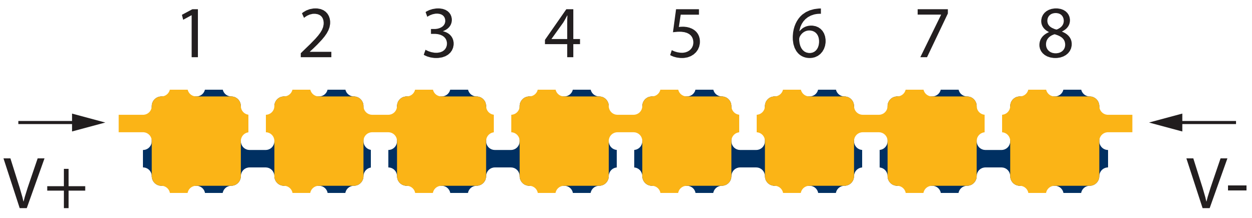

Figure 3.21: Detail of a single row cut into electrical series configuration.

out of the plane.

To facilitate printing a full sheet of gridded supercapacitors, we have designed three screens which create adequately thick layers on a single pass. These three screens are used to print the five layers of a supercapacitor, and have the following characteristics from Dynamesh Technologies:

Current Collector: BS-230/35. Steel screen with theoretical wet deposit of 35.25 μm.

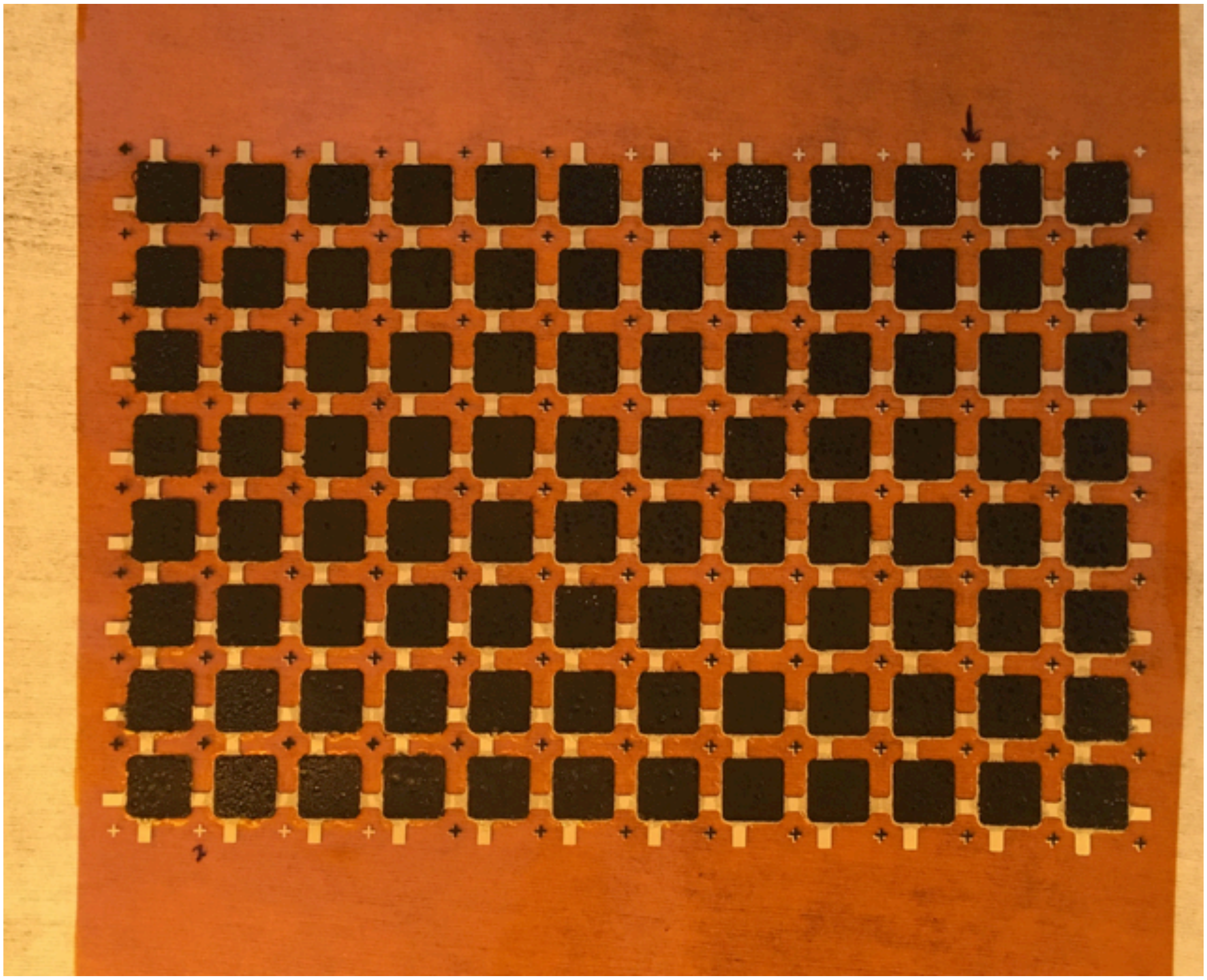

Figure 3.22: Image of our first successfully printed gridded superapacitors. The top layer of current collectors is not present in the image.

Electrode: 3D-200-115. Steel screen with theoretical wet deposit of 54.05 μm.

Electrolyte: Poly Alpha EX30-250 PW. Polymer screen with theoretical wet deposit of 250 μm.

Using these screens, we have successfully screen printed a full sheet of gridded supercapacitors as described above using the following formulations of inks:

Current Collector: Dupont 5025 Silver Conductive Ink.

Electrode: Composite carbon recipe SCEDE 6.95 as described previously in the dispenser printing section of this chapter.

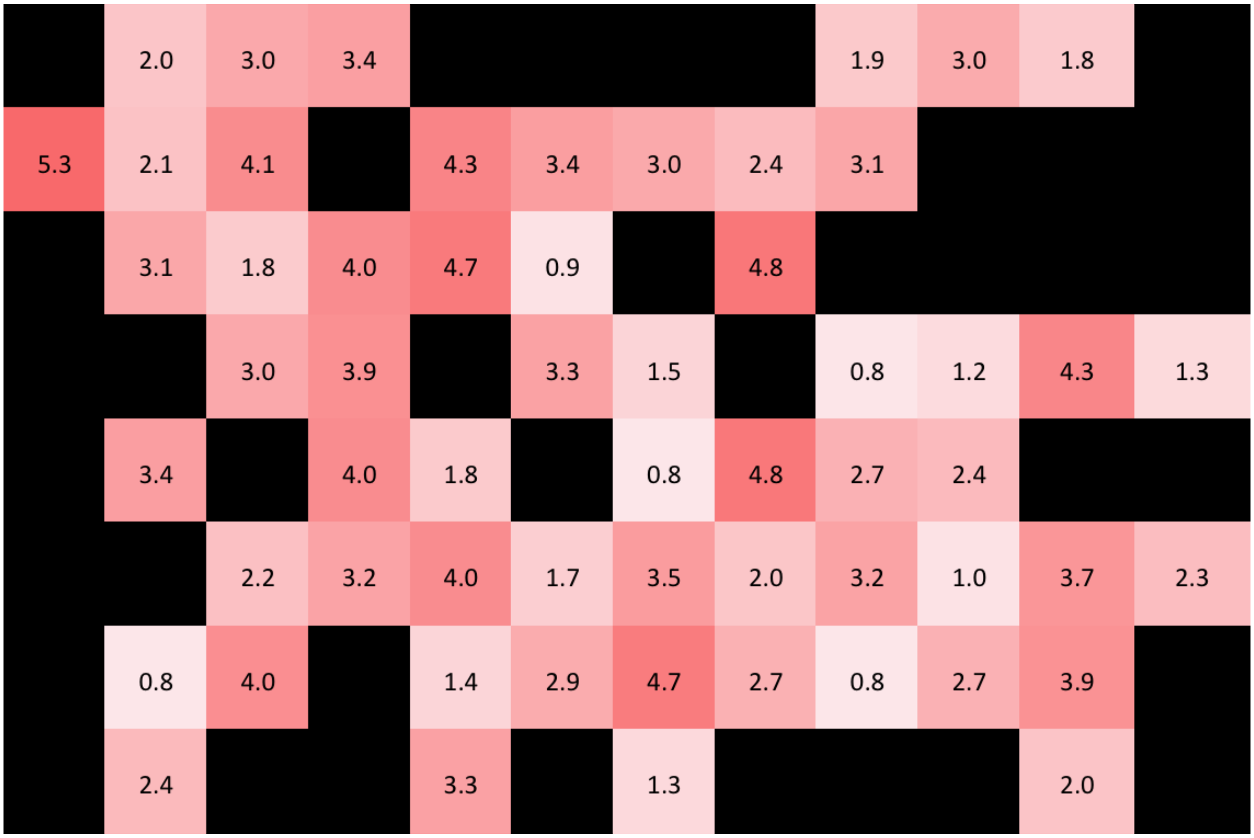

	2.0	3.0	3.4					1.9	3.0	1.8	
5.3	2.1	4.1		4.3	3.4	3.0	2.4	3.1			
	3.1	1.8	4.0	4.7	0.9		4.8				
		3.0	3.9		3.3	1.5		0.8	1.2	4.3	1.3
	3.4		4.0	1.8		0.8	4.8	2.7	2.4		
		2.2	3.2	4.0	1.7	3.5	2.0	3.2	1.0	3.7	2.3
	0.8	4.0		1.4	2.9	4.7	2.7	0.8	2.7	3.9	
	2.4			3.3		1.3				2.0	

Figure 3.23: Capacitance measurements (in mF) of individual supercapacitors in the grid pattern corresponding to figure 3.22. Black indicates shorted cell. Intensity of red is proportional to the capacitance measurement. Squeegee direction was from left to right.

> Electrolyte: Gel polymer electrolyte recipe as described previously in the dispenser printing section of this chapter.

The results from the first screen printed grid array are imperfect but promising. Individual cells show a mean capacitance of 2.8 mF with a standard deviation of 1.2 mF. Fifty eight of the 96 cells acted as capacitors and were not shorted, giving a 60% success rate. Two things to note: First, the relatively low capacitance (compared to dispenser printed cells) can be attributed to thinner electrode layers. Electrode wet layer thickness 54 μm will produce an even thinner dry layer, while cells produced on the dispenser printer were seen to have layer thicknesses in excess of 100 μm. Second, the truly customizable nature of the supercapacitor grid cannot be fully realized with a sparsely populated 60% success rate. To eliminate shorted cells, future printing should leverage two layers of GPE to ensure electrical isolation between electrodes. Additionally, to mitigate short-circuited cells, future work should focus on improving the homogeneity of the electrode and GPE inks. Dry nests and large particles cause blockages in the screen which result in swaths of cells with inadequate layer thicknesses. This is seen on the top-right side of the capacitance measurement grid. Also, noticeable is higher densities of shorted cells on the front, back, left, and right sides of the grid. This is likely due to pressure fall-off at the sides of the screen printing substrate plate. This could be ameliorated with a larger substrate plate, or by designing screens that use a smaller area of the available substrate plate.

Chapter 4

Modeling Interdigitated Porous Electrodes

As industrial and commercial demand for thin, small-footprint energy storage devices increases (e.g., for wearable electronics, wireless sensor networks, etc.), it is essential to develop theoretical descriptions for those devices in order to make effective design choices. Of particular interest are porous interdigitated electrodes, which can function as supercapacitors but which are nontrivial to analyze due to their unique geometry. In this paper, we develop a purely mathematical model to determine the dependence of a cell's capacitance and/or resistance on electrode height, width, and spacing, and electrolyte layer height. We then extend this model to incorporate effects from the porous nature of the electrodes, and show that in many cases of interest, the system can be described using a simple equivalent circuit.

4.1 Introduction

The advancement of miniaturized, wearable electronics has increased the demand for thin, flexible energy storage. Two-dimensional or in-plane electrode geometries can be fabricated in a single process and are more robust against bending when compared to stacked electrode geometries [43, 67]. Supercapacitors are especially relevant to modern electronics, as they can readily meet high power demands associated with wireless communication. Here we develop an analytical model of interdigitated supercapacitor electrodes to understand the effect of device design on the performance of the planar supercapacitor.

Modeling supercapacitors with interdigitated geometries requires consideration of the nontrivial geometry itself as well as how it couples to the behavior of porous electrodes. While

---

Work reported on in this chapter has been published as "Modeling of Interdigitated Electrodes and Supercapacitors with Porous Interdigitated Electrodes" in the March 2017 article of the Journal of the Electrochemical Society by authors Katherine J. Latimer, James W. Evans, Martin A. Cowell, and Paul K. Wright. This work is included with permission.

theories for these two components have been developed independently, we are unaware of a study which incorporates both. Wei first used the technique of conformal mapping to derive in closed form the capacitive properties of a periodic array of electrodes [80]. A subsequent extension of the theory by Igreja and Dias accounts for a finite dielectric layer height and substrate effects [40], but not for a finite electrode height, which we explore in this paper.

The characteristics of the cell with interdigitated electrodes, described by El-Kady and Kaner, depend on the electrodes being porous [43]. There has been much analysis of porous electrodes since the 1960s, for example the works of Euler and Nonnenmacher, or Newman and Tobias [24, 55]. A recent example is the modeling of porous electrodes of lithium batteries by Thomas et al. [56]. In general the equations for such systems become difficult to solve in greater than one dimension, where the electrical potential gradient is nonzero in multiple directions. Here, we make use of the numerical solver COMSOL®, and combine results from finite element analysis (FEA) with those from conformal mapping to provide insights on dependence of an interdigitated porous electrode cell's electrical behavior on its geometric characteristics.

4.2 Theory and Results

Interdigitated Geometry

For an electrical cell comprised of two conducting terminals separated by some dielectric or conductive medium of permittivity ϵ or conductivity σ, it is possible to find the capacitance (C) or resistance (R) of the cell, respectively, via the following relations:

$$R = \frac{\Delta V}{|\iint_S \sigma \vec{E} \cdot d\vec{S}|} \tag{4.1}$$

$$C = \frac{|\iint_S \epsilon \vec{E} \cdot d\vec{S}|}{\Delta V} \tag{4.2}$$

Here, ΔV is the voltage difference between the two terminals, $\vec{E}$ is the electric field as a function of position, and S is the surface of one of the terminals. For an ideal parallel plate capacitor (with no fringe fields) of plate area A and plate separation d, these integrals are easily evaluated when ϵ and σ are constants in space:

$$R = \frac{d}{\sigma A} \tag{4.3}$$

$$C = \frac{\epsilon A}{d} \tag{4.4}$$

Therefore, if the (possibly nontrivial) cell geometry of interest can be transformed into a geometry resembling a parallel plate configuration in such a way that preserves the orthogonality of electric field lines and equipotential lines (as demanded by the solution to

Laplace's equation which specifies the voltage at every point in the cell), then that transformation will easily provide the desired values of resistance and capacitance. Conformal mappings, or transformations of the 2D plane which preserve right angles, can be used to this end. Specifically, the Schwarz-Christoffel equation maps the upper half of the plane to any arbitrary polygon with specified interior angles [6]. Olthius et al used this method to derive the dependence of capacitance on the ratio of electrode width to electrode spacing for interdigitated, two-dimensional electrodes of specified number and length, assuming an infinitely thick medium above the electrodes [57]. Here, we investigate in addition the effects of finite electrode and electrolyte layer heights. Following the assumptions made in that paper, we take the electrodes to be of a sufficient length, L, that fringe effects at the top and bottom buses in figure 4.1a due to the gap δ can be ignored. We also assume the number of electrode couples, N, is large enough that fringe effects at either end of the device may also be neglected. This establishes a single symmetry unit as the basis of analysis, as shown in figure 4.1b. Comments on the magnitude of error introduced by these assumptions are given at the end of the section.

If we denote R_{unit} and C_{unit} as the resistance or capacitance (respectively) per unit length derived from the single cell, then the resistance or capacitance of the overall device will be:

$$R_{device} = \frac{R_{unit}}{NL} \tag{4.5}$$

$$C_{device} = NLC_{unit} \tag{4.6}$$

Mappings from the upper half-plane to both the desired geometry and the equivalent parallel plate geometry are shown qualitatively in figure 4.2. Colored dots in that figure show the vertices specified in the Schwarz-Christoffel mapping.

If we specify the coordinates of the original upper half-plane as z, those of the desired cell geometry as z', and those of the equivalent parallel plate geometry as z'', then the mathematical transformations are given as:

$$z' = \int \frac{\sqrt{z^2 - B^2} \quad dz}{\sqrt{z^2 - A^2}\sqrt{z^2 - C^2}\sqrt{z^2 - D^2}} \tag{4.7}$$

$$z'' = \int \frac{dz}{\sqrt{z^2 - A^2}\sqrt{z^2 - C^2}} \tag{4.8}$$

The integral in equation 4.8 can be transformed into an elliptic integral via a change in variables [57]. Unfortunately the integral in equation 4.7 does not simplify to a well-known form, but it can similarly be transformed into an expression which allows integration between points of discontinuity (See Appendix). Since the integrals in equations 4.7 and 4.8 are not analytically solvable, it is not possible to start with a desired cell geometry and from there derive its capacitance and resistance parameters. Instead, both integrals were evaluated numerically using the 'integral' function in MATLAB® for a wide range of combinations of values for (A, B, C, D), giving corresponding values (A', B', C', D') and (A'', C'') for the two

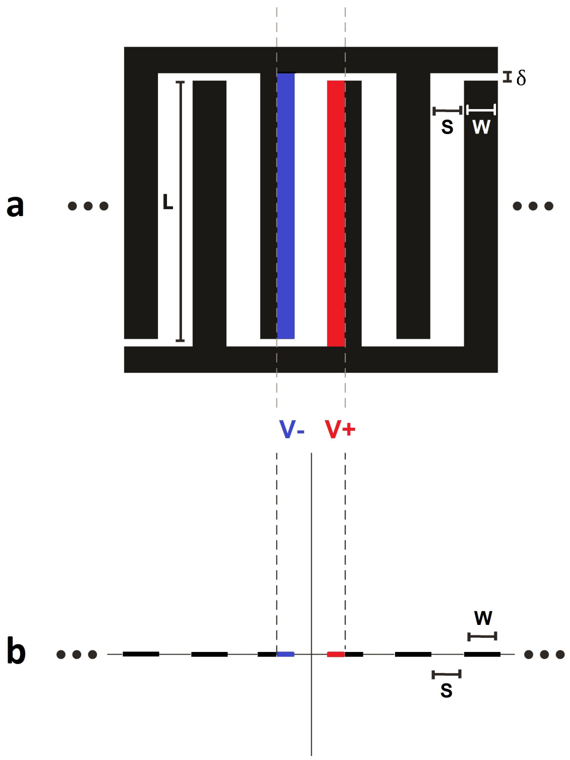

Figure 4.1: Symmetry unit for interdigitated electrode model. Top view shown in (a); cross section (which is the two-dimensional plane treated in this model) is shown in (b). Dashed lines denote symmetry planes, which are equivalent to insulated boundaries.

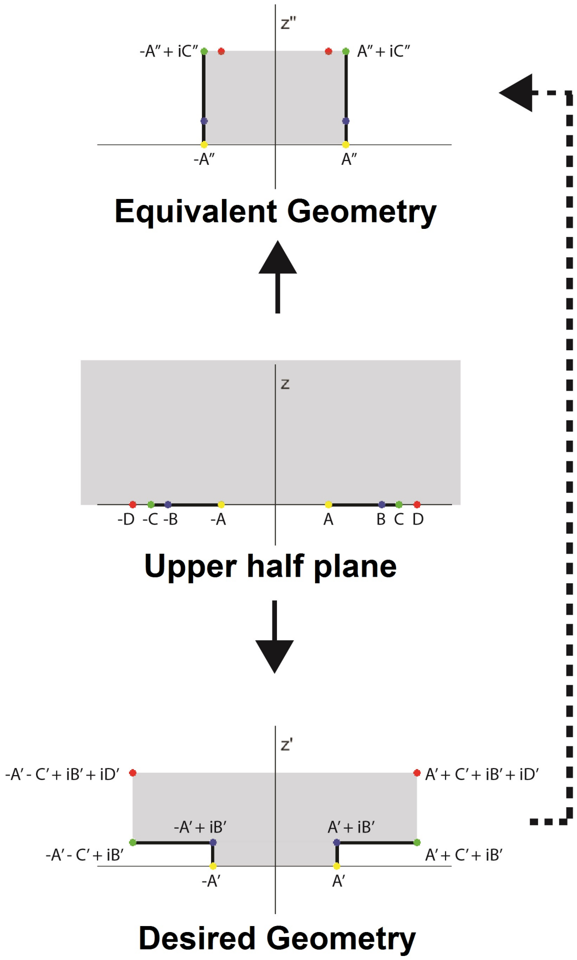

Figure 4.2: Qualitative description of maps to model cell with finite electrode and electrolyte layer heights. Electrodes shown in solid black lines, with shading showing map boundaries.

different mappings. This produced a "database" of geometries which could be searched for a given cell geometry of interest, with corresponding R_{unit}, C_{unit} given by:

$$R_{unit} = \frac{1}{\sigma}\frac{2A''}{C''} \tag{4.9}$$

$$C_{unit} = \epsilon\frac{C''}{2A''} \tag{4.10}$$

It should be noted that although the mapping given by equation 4.7 produces a unique result (A', B', C', D') for any single (A, B, C, D), that result may be scaled by any constant factor without affecting its C_{unit}.

The effects of each parameter in the four-dimensional parametric space were visualized by selecting several different baseline geometries in the z' space, as shown in figure 4.3. For each of the geometries, the effect of varying electrode spacing, electrode height, electrode width, and electrolyte layer height (or A', B', C', and D', respectively) in isolation is shown in the graphs in figure 4.4 (The quantities A' and B' correspond to $\frac{S}{2}$ and $\frac{W}{2}$ given in figure 4.1). Each color represents the corresponding baseline geometry in figure 4.3. Normalized capacitance is given by $\frac{C"}{A"}$, and normalized dimensions are given as a fraction of the sum of all dimensions; for example, the normalized A' dimension, A'_{norm}, is $\frac{A'}{A'+B'+C'+D'}$. Numerical dimensions of the geometries in figure 4.3 are given in table 4.1. As would be expected, capacitance increases with increasing electrode height (B) and width (C), although the latter dependence is weak, and decreases with electrode spacing (A). The topmost geometry in figure 4.3 is considered in greater detail for the remainder of the paper.

Results were verified using FEA in COMSOL®, to excellent agreement. A comparison of electric field maps between the two methods is shown in figure 4.5. For the particular geometry shown, the unit capacitance of the cell with a vacuum dielectric was found to be 3.3619 pF/m and 3.3585 pF/m via the conformal mapping and FEA methods, respectively.

Geometry Number	$\mathbf{A'_{norm}}$	$\mathbf{B'_{norm}}$	$\mathbf{C'_{norm}}$	$\mathbf{D'_{norm}}$	$\mathbf{\frac{C''}{A''}}$
1	0.215712	0.019963	0.567358	0.196967	2.630157
2	0.097103	0.028724	0.422054	0.452118	4.346442
3	0.245172	0.389903	0.026211	0.338714	0.106909
4	0.142953	0.206697	0.499157	0.151193	3.491749
5	0.208292	0.321670	0.167863	0.302175	0.805904
6	0.140269	0.040866	0.383906	0.434960	2.736934
7	0.050161	0.092347	0.671559	0.185933	13.388147
8	0.098238	0.647375	0.101144	0.153243	1.029588
9	0.333296	0.117959	0.252491	0.296254	0.757558
10	0.067187	0.090877	0.660140	0.181796	9.825378

Table 4.1: Normalized dimensions corresponding to geometries in figure 4.3.

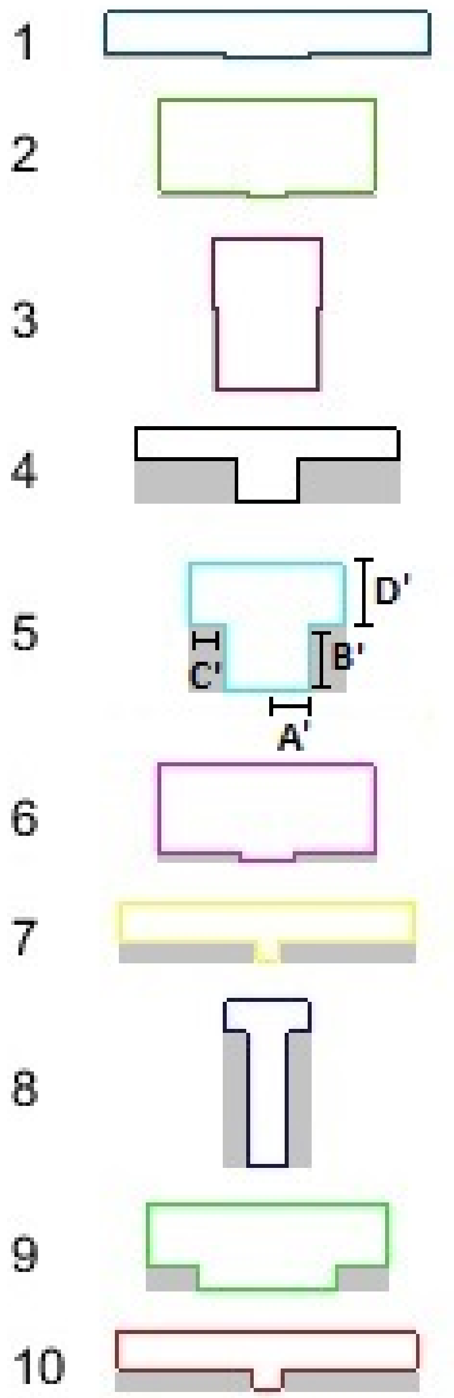

Figure 4.3: Baseline geometries. Geometry #1 (topmost) is treated in detail in all subsequent models. Dimensions are labeled in geometry #5 for clarity. Electrode regions are shaded in gray.

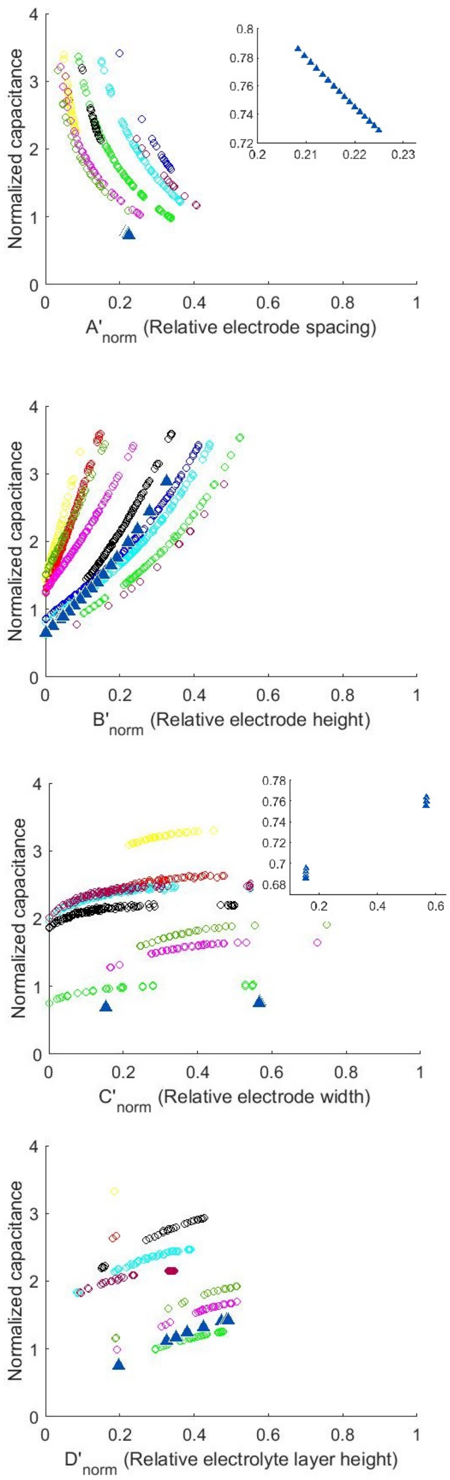

Figure 4.4: Effect of dimensions on cell capacitance. Colors correspond to geometries shown in figure 4.3. Data for geometry #1 in figure 4.3 are shown with triangle markers and also expanded in insets for clarity.

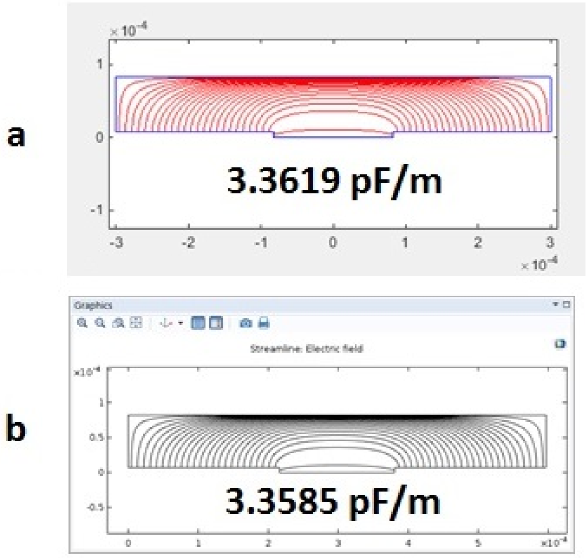

Figure 4.5: Electric field line map and cell capacitance values obtained from (a) conformal mapping and (b) FEA in COMSOL®.

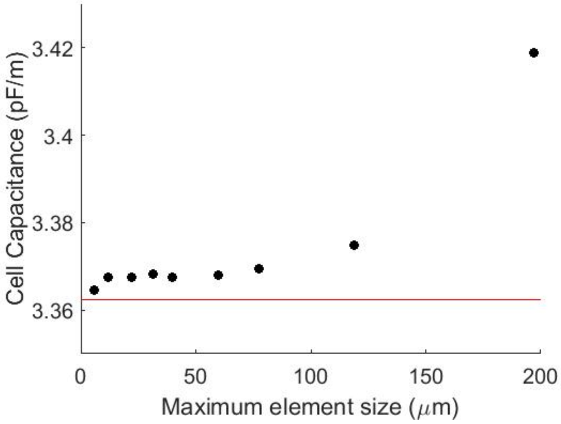

Figure 4.6: Convergence of FEA-derived cell capacitance values versus mesh size and mathematically-derived cell capacitance for comparison in red.

One advantage of conformal mapping over numerical analysis is the degree of precision to which cell capacitance/resistance values can be calculated. As shown in figure 4.6, decreasing the mesh size of the numerical simulation results in calculated capacitance values which converge to that found via numeric integration in MATLAB®. The numerically integrated values were constant to full available precision for a wide range of specified tolerances, which means the functions of interest are smooth enough to be calculated with minimal error. Furthermore, the time required to perform the transformation integrals for a single cell geometry on MATLAB® is on the order of 50 ms, whereas the equivalent calculation takes roughly ten times that on COMSOL® (both performed on a PC with an Intel(R) Core(TM) i7-6800K 3.40 GHz CPU and 32.0 GB memory). Therefore, in a situation where it is desirable to systematically analyze the general dependence of a cell's electrical parameters on its dimensions (for example as shown in figure 4.4), this method is far more efficient.

The mapping given by equation 4.6 assumes the electric field to be completely confined to the electrolyte layer, which becomes true in the limit where

$$\epsilon_{electrolyte}/\epsilon_{air} \to \infty$$

A simulation was carried out in COMSOL® to assess the magnitude of the error resulting from this approximation, and it was found that the true capacitance (accounting for imperfect confinement of the electric field to the electrolyte layer) decreased by 14% with a $\epsilon_{electrolyte}/\epsilon_{air}$ ratio of 10 for the geometry shown in figure 4.5. However, the calculation for

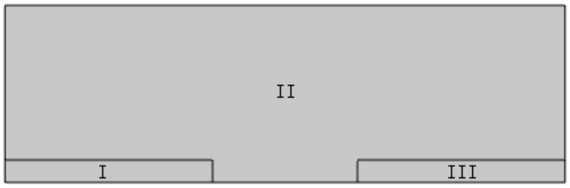

Figure 4.7: Model geometry. Equation 4.15 applies in regions I and III; equation 4.11 applies in region II.

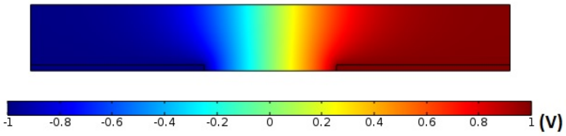

Figure 4.8: Potential distribution at t = 0 in the electrolyte.

cell resistance remained quite accurate when the surrounding medium was non conductive (as would be the case in many applications).

Additional sources of error in the model described above come from the neglect of fringe capacitance. This occurs at the two electrodes on the far ends of the whole device, as well as the end of each leg (shown by the gap δ in figure 4.1a). Based on the weak dependence of normalized capacitance on C'_{norm} observed in figure 4.4, we expected the former effect to be insignificant. This was confirmed by simulating a unit cell in COMSOL® with one electrode region being twice the length of the other (as would be the case at device ends). The change in capacitance was less than 0.1%. This result suggests that equations 4.5 and 4.6 might be more accurately expressed by replacing N with $(N-1)$, with the resulting fractional error depending on N. It also suggests that the fractional error due to the approximation of infinitely long electrodes can be reasonably estimated in the case that $\delta \approx S$ as $\approx \frac{W}{W+L}$. For the devices in [43] we estimate that this will be roughly on the order of 10%.

4.3 Porous Electrodes

In what follows we make the usual assumption that the matrix phase of the electrode and the electrolyte therein can be treated as two superimposed continua with macroscopically uniform properties [55]. We further assume that conduction in the matrix obeys Ohms law with some effective conductivity. Finally, we assume that conduction in the electrolyte will also obey Ohms law. This last assumption is made because we are primarily interested in electrolytes that are ionic liquids consisting of one cation, one anion and no solvent; consequently, electroneutrality mandates there can be no concentration gradients, outside double layers, and therefore conduction in the electrolyte is only by migration. The assumption is also valid for electrolytes, with a solvent, that are well supported electrolytes. The assumption would be an approximation in other cases.

We are considering a simple, 2-dimensional cross section of an interdigitated electrode as shown in figure 4.7. We continued to study the geometry shown in figure 4.5 since it approximates that of a real device of interest, for example as fabricated in [43].

Regions I and III are treated as a two-phase system consisting of an ionic liquid electrolyte and a "perfectly conducting" matrix of porous material. Both are assumed to be continuous throughout the regions so that current may flow at any point either in the x or y directions in the electrolyte phase, or into the electrode phase. Region II is the bulk electrolyte. In that region we assume no accumulation of charge, and therefore the potential obeys Laplace's equation:

$$\nabla^2 \Phi_e = 0 \tag{4.11}$$

For the electrodes, we consider the matrix/electrolyte interface to be purely capacitive (no faradaic or leakage current), and therefore the transfer of current from electrolyte to matrix at any point in the region is proportional to the time derivative in voltage difference between those two phases. Specifically, the current density in the electrolyte is:

$$\begin{aligned} \vec{J}_e &= \sigma \vec{E}_e && (4.12) \\ &= -\sigma \nabla \Phi_e && (4.13) \end{aligned}$$

And therefore,

$$\nabla \vec{J}_e = -\sigma \nabla^2 \Phi_e = C_{spec} \frac{\partial(\Phi_e - \Phi_m)}{\partial t} \tag{4.14}$$

Where C_{spec} is the capacitance per unit volume of the matrix material and σ is the effective conductivity of the electrolyte within the matrix. We make the simplifying assumption that the matrix material is highly conductive, such that its potential is independent of position. Furthermore we suppose that the potential applied to the electrodes remains constant over time (for t $>$ 0), and thus equation 4.11 simplifies to a PDE in one variable:

$$\nabla^2 \Phi_e = -K \frac{\partial \Phi_e}{\partial t} \tag{4.15}$$

The constant K is now equal to $\frac{C_{spec}}{\sigma}$. For porous carbon-based materials, values cited in the literature for specific capacitance vary from 35 F/cm^3 to 112 F/cm^3 but are generally on the order of 100 F/cm^3 [71]. The conductivities of the ionic liquid electrolytes of interest in our investigation also vary, but are generally on the order of 1 S/m for salts with imidazolium-based cations, which are commonly used in devices of interest for this study [29]. These values were used to obtain the results below.

Spatial boundary conditions specify no component of the electric field perpendicular to outer boundaries, which are either electrically insulated (top and bottom) or symmetry planes (sides):

$$\nabla \Phi_e \cdot \hat{n} = 0 \tag{4.16}$$

The initial voltage distribution at t = 0 was obtained by setting Φ_e to 0 V and 1 V in the two electrodes, and solving for the stationary voltage distribution in the bulk electrolyte. To examine this, consider the voltage of the matrix to be switched on instantaneously so that the expression $\frac{\partial(\Phi_e-\Phi_m)}{\partial t}$ equals $\delta(t = 0)$. At any point in the electrode regions, the charge can either move in the cross-sectional plane (equivalent to an infinite number of differential resistors in parallel), or to the boundary with the matrix phase (equivalent to a differential capacitor in parallel with the resistors). Because the "frequency" of the delta function is infinite, the capacitor will "look" to the charge like a short, and all current in the region will go to charging the capacitor in that instant. Therefore there will be no voltage drop in the cross-sectional plane (since the capacitor is initially uncharged), and we can set $\Phi_e = \Phi_m$ at t = 0 within the electrodes. The initial distribution is shown in figure 4.8.

The electric field strength (directly proportional to current density norm by Ohm's Law) is shown as a function of time over the discharging of the capacitor in figure 4.9. It is clear that most of the current is concentrated at the vertical edges of the electrodes, which corroborates the steep increase in capacitance versus electrode height observed in figure 4.4.

Equivalent Circuit Model for Porous Interdigitated Electrodes

Of interest in this study is whether, and to what extent, a simplified equivalent circuit model can describe the behavior of the porous interdigitated electrode system. In order to investigate this, the parameters for electrolyte conductivity and electrode specific capacitance were varied over a range encompassing the baseline values of 1 S/m and 100 F/cm^3 (respectively), and exponential curves were fitted to the FEA output for current through the cell versus time. For the equivalent circuit shown in figure 4.11, which includes two capacitive and resistive elements (roughly representing the porous electrode matrices and the electrolyte in the electrode, respectively) in series with a third resistive element (roughly representing the resistance of the bulk electrolyte in the cell), the time constant would be given as:

$$\tau = \frac{(2R_1 + R_2) * C}{2} \tag{4.17}$$

because the capacitors add reciprocally in series. As a first estimate, C was taken as the specific capacitance of the electrode material times the area of the electrode region. R_2 was found using the conformal mapping methods described in 3.1 (for non-porous electrodes at a fixed potential difference of 2V). This left R_1 as an unknown parameter to be determined by the simulation results. Two cases were examined: (1) In which the conductivity of the electrolyte was taken to be equal in both the bulk region (II in figure 4.7) and in the wetted electrode (I and III in figure 4.7); and (2) In which the resistivity of the electrolyte in the wetted electrode was specified as two orders of magnitude greater than that in the bulk region, as found in recent experiments [25].

Figure 4.12 shows results from the first case, which confirm simple RC-circuit behavior within the range of electrolyte resistivities and electrode specific conductances examined, *viz.* linear dependence of the decay time constant on those parameters. Regression lines were constrained to pass through the origin in order to give a semiqualitative description of how well the simulation data conformed to equation 4.17. The values of R_1 and R_2, calculated

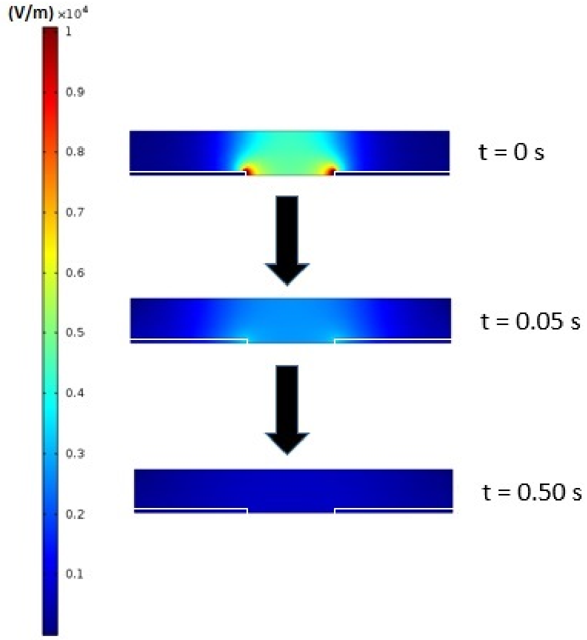

Figure 4.9: Electric field strength over the course of simulated discharge of capacitor in COMSOL. Edges of electrodes outlined in white.

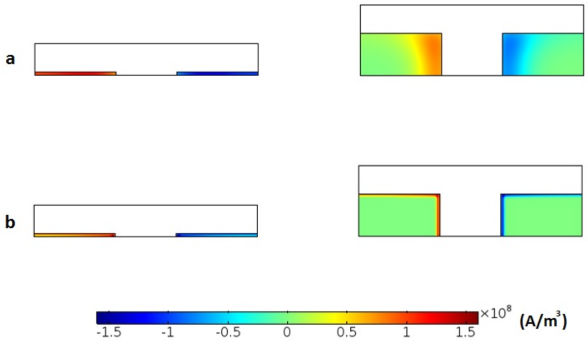

Figure 4.10: Surface maps of divergence of current density for (a) equal electrolyte resistivity in all regions, and (b) resistivity of the electrolyte 100 times greater in the electrode region. The electrode heights on the right have been increased by a factor of 15 from the original geometry, shown for comparison on the left.

as described above, are both found to equal 3.3 $\Omega \cdot m$, which indicates that resistance of the bulk electrolyte and electrolyte within the electrode contribute in equal measure to the cell's equivalent series resistance.

Figure 4.13 shows results from the second case. Although the decay time constant still varies nearly linearly with electrolyte resistivity and electrode specific conductance, the coefficient of determination for the linear regression is notably lower, which suggests deviation from the simplified equivalent circuit model. However, the calculated value of R_1 is 5.6 $\Omega \cdot m$, indicating that even the drastic increase in resistance of the electrolyte in the electrode region does not increase the overall estimated series resistance at a comparable scale.

The difference observed between the two cases may be due in part to non-uniform charging/discharging throughout the electrode when the conductivity of the electrolyte in that region is severely limited. Figure 4.10 shows surface maps of charge/discharge current density throughout the cell generated by FEA simulations. These maps confirm that this phenomenon indeed occurs, even for a relatively small electrode height.

We lastly investigated the effects of varying only the electrode height (given by B') on the

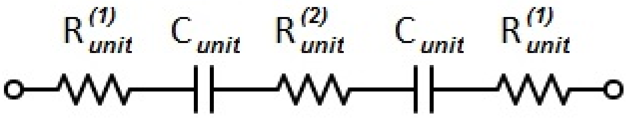

Figure 4.11: Simple equivalent circuit model proposed for the porous interdigitated electrode.

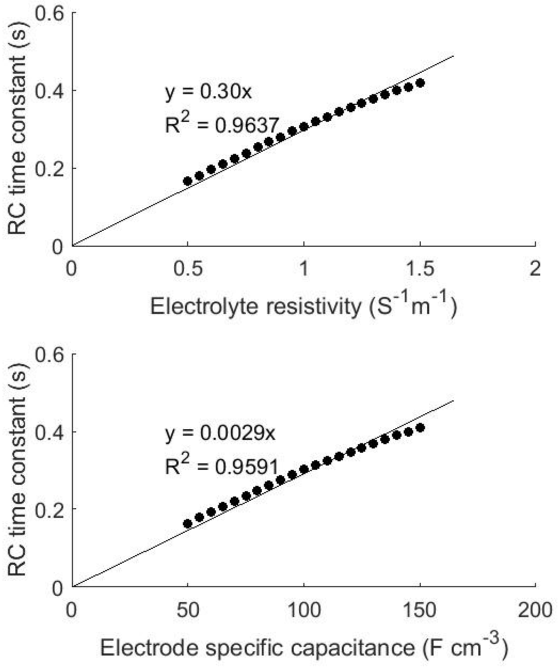

Figure 4.12: Variation of cell decay time constant with (a) electrolyte resistivity (C_{spec} constant at 100 F/cm^3) and (b) electrode material specific capacitance (Electrolyte resistivity constant at 1 $S^{-1}m^{-1}$), where the resistivity of the electrolyte is uniform in all regions. Data points from FEA and line from linear regression.

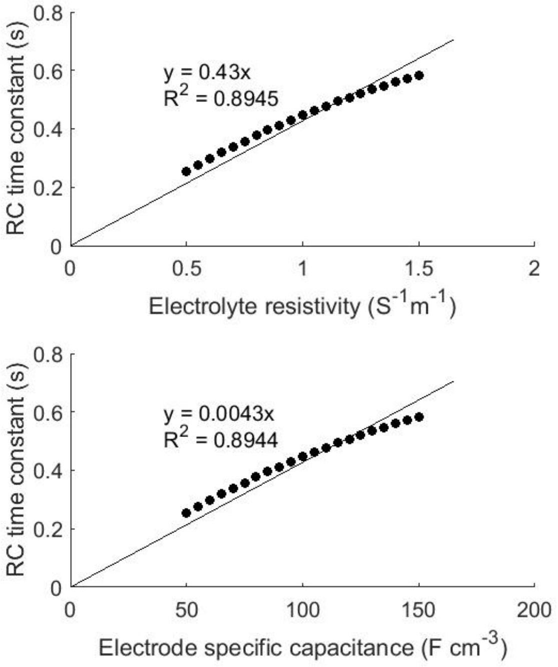

Figure 4.13: Variation of cell decay time constant with (a) electrolyte resistivity in the bulk region (C_{spec} constant at 100 F/cm^3) and (b) electrode material specific capacitance (Electrolyte resistivity in the bulk region constant at 1 $S^{-1}m^{-1}$), where the resistivity of the electrolyte is 100 times greater in the electrode region. Data points from FEA and line from linear regression.

charge/discharge time constant of the cell. This dimension was swept along a range of values from 5 to 150 μm, from an original value of 10 μm. This simulation was again performed for the same geometry, in the two cases outlined above for conductivity of the electrolyte in the electrode. Results are shown in figures 4.14 and 4.15.

Close to the original value of B', the time constant varies approximately linearly with B',

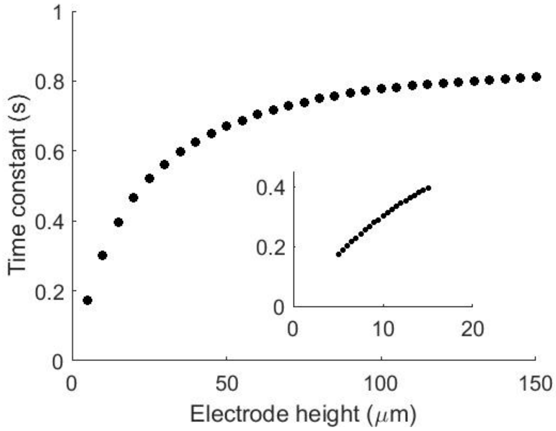

Figure 4.14: Variation of cell decay time constant with electrode height (baseline height being 10 μm), where resistivity of the electrolyte is uniform in all regions. Inset shows linear regime of variation.

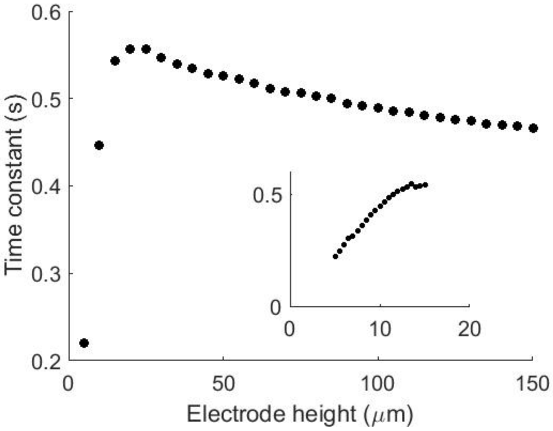

Figure 4.15: Variation of cell decay time constant with electrode height (baseline height being 10 μm), where the resistivity of the electrolyte is 100 times greater in the electrode region. Inset shows the near linear regime of variation.

but at larger electrode heights the relationship appears asymptotic and even shows a negative correlation for the case of decreased conductivity of the electrolyte in the electrode. This behavior can be rationalized by the fact that the height of the electrode in the geometry of interest is quite small relative to the other dimensions of the cell, and therefore its normalized value B'_{norm}, given by $\frac{B'}{A'+B'+C'+D'}$, does not vary significantly (in absolute terms) with B'. For example, for the linear regime displayed in the inset of figure 4.10, B'_{norm} varies from roughly 1% to 3%. Upon examination of figure 4.4, it is clear that the cell constant does not vary significantly in this range. The main effect on the time constant, then, comes from the change in cross-sectional area of the porous electrode, which affects C and R_1 only. However, as B'_{norm} increases past this linear regime, the effects of decreased R_2 in addition to increased R_1 and C result in a leveling-off of the time constant dependence on electrode height. We hypothesize that the negative slope beyond the linear regime in figure 4.15 is due to a restriction of capacitative behavior to the edges of the electrode (Figure 4.10), which means that C does not scale as rapidly as the area of the electrode with increasing electrode height.

4.4 Conclusion

The Schwarz-Christoffel conformal mapping can be used to analyze the relationship between a cell's capacitance/resistance and its geometric parameters (electrode height, width, and spacing, and electrolyte layer height) for an interdigitated electrode configuration. Results from this mathematical technique are confirmed by - and even show signs of improvement in speed and accuracy over - FEA. Therefore, given specific practical constraints (for example on cell volume, amount of electrode material to be used, etc.), one can optimize the cell's electrical characteristics.

By combining the results of the above model with concepts from porous electrode theory, we showed that in many circumstances, a supercapacitor made of porous interdigitated electrodes can be effectively modeled using a simple equivalent circuit, even in the realistic scenario of greatly reduced electrolyte conductivity within the porous matrix of the electrode. Furthermore, FEA simulations in which electrode height is varied in isolation provide results which agree with qualitative predictions from conformal mapping, and also suggest a point of diminishing return with regard to maximizing the cell's effective RC time constant. Overall, our models provide quantitative metrics which can be used to inform the design and fabrication of porous interdigitated electrode supercapacitors in order to achieve optimal performance.

Chapter 5

System Integration using Photovoltaics

5.1 Indoor Photovoltaic Energy Harvesting

Organic solar cells (OSC) currently achieve more than 10% of power conversion efficiency (PCE) under 1-sun conditions [33, 9] and can be stable over several years [60, 30]. The materials involved in their fabrication require low processing temperatures, compatible with many plastic substrates [22, 23]. They can also be completely printed [1, 31], allowing the use of large area, high throughput, low cost manufacturing processes such as roll-to-roll printing. As a result, full-scale outdoors demonstrations have already been successfully performed [38, 2].

The combination of flexibility, low-cost and short energy payback time makes OSC particularly interesting as an energy harvester for autonomous low-power devices, such as wearables or wireless sensor nodes (WSN) for the Internet of Things. In these new applications, lightness and flexibility become highly desirable and milder operating conditions alleviate materials stability concerns. Typically, WSN are designed as very low-power systems able to gather data from their environment, connect to a network and perform minimal computation tasks, and are self-powered [44, 34]. In order to minimize energy consumption WSN operate in cycles, alternating long periods of sleep with very short active periods (of the order of hundreds of milliseconds) during which they perform their tasks. Typically, $10-100\ mW$ are needed under active mode, while this range falls to $1100mW$ during the sleeping mode [45, 68, 66]. WSN are expected to operate in a wide variety of environments, including indoors, where the available light differs significantly from the conventional 1-sun illumination for which solar cells are usually designed. In contrast to outdoors, there are no clearly defined

---

Work reported on in this section has been published as "Organic solar cells and fully printed supercapacitors optimized for indoor light energy harvesting" in the June 2016 article of the Journal Nano Energy by authors Balthazar Lechene, Martin Cowell, Adrien Pierre, James W. Evans, Paul K. Wright, and Ana C. Arias. This work is included with permission.

standards to test solar cells in low or indoor lighting conditions, which are typically more varied both in terms of spectrum and intensity. Outdoors, the spectrum is always that of the sun and the intensity usually ranges between $100mW/cm^2$ and $1mW/cm^2$. For indoors, it has been reported that, near windows, the light is dominated by the daylight sun spectrum [65]. In places with no access to sunlight, the spectrum of indoor light depends largely on the type of light source used. Earlier work by Minnaert et al. [54] suggests that artificial indoor lighting can be sorted into three categories of spectra, corresponding to incandescent light bulbs, sunlight-type light bulbs such as high temperature compact fluorescent lights (CFL) and all other light sources such as LEDs. Indoor light intensity varies greatly, depending on the type of room, the position, orientation and proximity to the light source. While the intensity right below a lamp or through a window can exceed 1 mW/cm^2, the intensity in poorly lit rooms can fall under 10 $\mu W/cm^2$ [26]. Indoor light intensity is usually described by its illuminance, a measure relating the human eye's sensitivity to the light's spectrum. Conversion of illuminance (ϕ, in $lux = lm/m^3$) to irradiance (P, in W/m^3) per unit wavelength λ is given by:

$$\phi(\lambda) = K_m V_m(\lambda) P(\lambda) \tag{5.1}$$

Where K_m, the maximum photopic luminous efficacy, equals 683 lm/W and V_m is the spectral luminous efficiency function (Figure 5.1). Thus, the illuminance is very dependent on the light spectrum. Previous studies on solar cells for indoor conditions have used $400-500lx$ as a reference illuminance [54, 18] or light intensity ranging from 1 mW/cm^2 to below 60 $\mu W/cm^2$ [26, 69]. Several countries establish standards regarding the minimum indoor lighting requirements (such as the IESNA illuminance recommendations in the U.S. or the European Norm 12464-1). In Europe and America, the lowest legal illuminance in buildings (transit areas) is $50-100lx$, and the minimum allowed in offices and commercial buildings usually ranges between 200 and 500 lx. From these considerations, three ranges of indoor illuminances are defined: poor lighting (from 0 to 200 lx), typical lighting ($200-500lx$) and excellent lighting (superior to 500 lx). Converted to irradiance with the AM1.5 spectrum, those illuminance categories correspond respectively to $0-180mW/cm^2$; $180-450mW/cm^2$ and $> 450mW/cm^2$. To generate the 100 μW needed for the sleep mode operation of a WSN in an environment with 450 mW/cm^2 of light power available, 2.2 cm^2 of a solar cell with 10% of PCE would be enough. To power the active mode of WSN ($10-100mW$), the area of the solar cell would need to be $0.22-2.2m^2$. Such a big area is not practical for most indoor applications. To overcome that limitation, one strategy is to take advantage of the cyclical operation of WSN by storing excess energy produced during their sleep period and using it to power the active mode. Super-capacitors are able charge and discharge very rapidly, can withstand many cycles of operation and do not require charge/discharge management electronics. They can be fully printed and made mechanically flexible, thus presenting the same manufacturing advantages as OSC [84, 86]. OSC and super-capacitors can be combined to form a system able to simultaneously generate and store energy, called a photo-rechargeable system [70]. Such combinations have previously been demonstrated as part of a complete electronic system [7], as two separate devices connected together [20, 11, 12], or as a stack forming a single device [79, 78, 13, 85, 83, 72, 10]. Single-stacks reduce the footprint and the internal series resistance of the system compared to separated solar cells and super-capacitors externally connected [79].

Most of the earlier reports on photo-rechargeable systems use dye-sensitized solar cells (DSSC),[11, 13, 85, 83, 88] while a few groups investigate organic solar cells [12, 79]. Moreover, all these reports dealt exclusively with outdoor light conditions, with only one [72] investigating intensities between 10% and 100% of 1-sun. A metric to consider for photo-rechargeable systems is the energy conversion and storage efficiency (ECSE) of the system. Measured during a charge-discharge cycle, the ECSE is defined as the ratio between the electrical energy that can be extracted from the super-capacitor and the total light energy received by the solar cell during the charging step. To the best of our knowledge, the highest reported ECSE of photo-rechargeable systems to date is 5.12% with DSSC and 0.82% for organic solar cells [70].

In this work, we demonstrate that an OSC integrated with a super-capacitor can provide enough energy to power the active mode of WSN operating under indoor light. In addition, we show that optimization of OSC for low light intensity is different from the 1-sun case and we establish that the ratio of the 1-sun short circuit current over the dark current the current flowing through the cells when biased in the dark is a critical parameter to control. The best solar cells for 1-sun achieve 6.2% of PCE under 100 mW/cm^2 and 5.2% under 310 $\mu W/cm^2$ (typical indoor light), while the solar cells optimized for low light reach 5.7% under 100 mW/cm^2 and 7.6% under 310 $\mu W/cm^2$. Fully-printed super-capacitors are developed with a maximum capacitance of 130 mF/cm^2, maximum power of 9.8 mW/cm^2, and maximum energy of 31 $\mu W - hr/cm^2$. A photo-rechargeable system comprising a 0.475 cm^2 OSC (optimized for indoor conditions) externally connected with a super-capacitor achieves an ECSE of 1.57% under 1-sun light, and an ECSE of 2.92% under simulated indoor light (310 $\mu W/cm^2$).

Experimental

Solar cell fabrication

ITO-covered glass (from Thin Film Devices) were sequentially cleaned in acetone, isopropanol and water, then passed under UV ozone plasma treatment for 30 min. PEDOT:PSS (Heraeus Clevios VPAI 4083, 40 nm) was spin-coated and baked at 180 $°C$ for 10 min. After transfer in a glovebox, an active layer of poly[N- 9- heptadecanyl-2,7-carbazole-alt-5,5-(4,7-di-2-thienyl-2,1,3-ben- zothiadiazole)] (PCDTBT) and and [6,6]-phenyl-C71-butyric acid methyl ester (PC71BM) in solution (1:3.7 in ortho-dichlorobenzene with 5% dimethyl sulfoxide) was spin-coated above (80 nm). PCDTBT was purchased from Saint-Jean Photochimie and PC71BM from Solaris. Finally, PEIE (Sigma Aldrich) diluted to 0.048 wt% or 0.024 wt% in ethanol was also spin-coated and the whole device was annealed at 70 $°C$ for 10 min. All PEIE layers were too thin to be accurately measured with conventional profilometry methods, suggesting

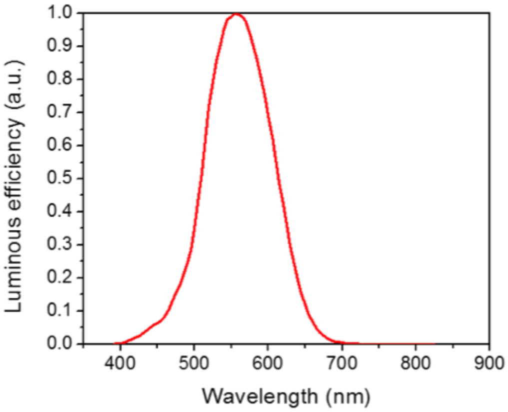

Figure 5.1: CIE 1988 modified 2° spectral luminous efficiency function

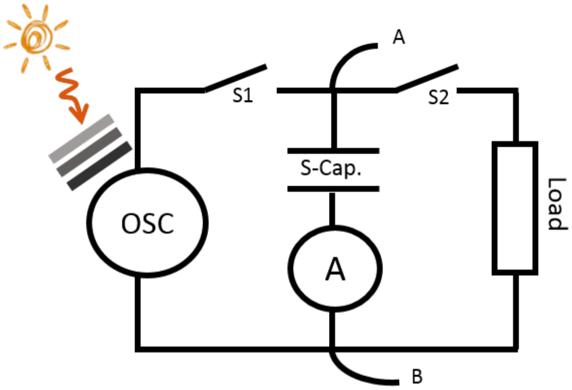

Figure 5.2: Setup used to for the charge-discharge experiments of the photo-rechargeable system. The Solar cell (OSC), super-capacitor (S-Cap) and Load (120 Ω resistor) are connected in parallel. Two switches (S1 and S2) allow to isolate the components from each others. The current is measured with a amp-meter (sourcing 0 V) in series with the super-capacitor and points A and B indicate where the voltmeter is connected.

a thickness value below 5 nm. 200 nm of aluminum were thermally evaporated to complete the devices.

Supercapacitor fabrication

The super-capacitor were fully dispenser printed. First the polymer binder was dissolved in N-Methyl-2-pyrrolidone (NMP) and the carbon powder mixture suspended in the resulting gel, producing the electrode ink. Then, a 1 cm^2 layer of electrode ink was deposited on a stainless steel foil substrate. This wet ink layer was briefly dried in an oven at 60 $°C$ for 15 min. This does not cure the ink completely, but thickens it in preparation for deposition of the next layer. The gel polymer electrolyte layer was deposited next, with its dimensions extending beyond the region covered by the first electrode layer to ensure adequate electrical isolation between electrodes. Both the electrode and electrolyte inks were deposited wet, but solidified once their common NMP solvent was removed. This two layer stack was therefore partially dried in an oven at 60 $°C$ for 30 min again to thicken the top layer in preparation for the final electrode layer. The final electrode was deposited on top of the GPE layer shadowing the dimensions of the bottom electrode. This stack was dried in the oven at 60 $°C$ for 15 min and finally cured at 20 $°C$ for 96 hr until all the NMP was fully evaporated. The resulting wafer readily separated from the stainless steel substrate and was soaked in BMIMBF4 until saturated. The supercapacitor electrode surfaces were coated in a thin layer of AB powder to reduce interfacial resistance. Stainless steel foils were applied to the AB coated electrode surfaces to act as current collectors during experiments. All super-capacitors in this work had a 1 cm^2 area.

Electrical characterization

For the solar cells, JV curves were acquired using a Keithley 2400 precision current and voltage Source Measurement Meter. Voltage measurements were obtained with a Tektronix TDS 5034 oscilloscope. Current measurements in the Results section were obtained using a Keithley 2400 in current sense-mode while sourcing exactly 0 V. For the supercapacitor, power and energy values were acquired using Neware BTS. Calculation of capacitance, series DC resistance, and Coulombic efficiency was done with data from the Neware BTS. Leakage currents of the super-capacitors were measured with a Keithley 2400 held at constant voltage.

Light sources

For the sun spectrum, a solar simulator from Newport Oriel Sol1A (xenon lamp). The power was calibrated with a Newport System V reference silicon solar cell. Neutral density filters from Newport (FBS family, ND04, ND05, ND10, ND20 and ND30) were used to dim the light coming from the solar simulator. The light bulbs used to represent indoor lighting were: GE Softwhite 2800 K (incandescent), GE Energy Smart Daylight CFL 6500 K (CFL) and Feit Electric Dimmable A19 LED 3000 K. The light spectra were measured using a Thorlab CSS200 spectrophotometer. The powers of the lamps were adjusted to represent 300 lx with a Hamamatsu S238766R silicon photodiode. The expected current of the photodiode was calculated based on its photoresponsivity, the lamp spectrum and the photopic luminous efficacy function.

Results and Discussion

Fabrication, characterization, and optimization of organic solar cells

OSC used in this work are fabricated on glass, with a classic architecture (shown in Fig. 5.19) using PEDOT:PSS as the hole transport layer, polyethylenimine ethoxylated (PEIE) as the electron transport layer, and an active layer of PCDTBT:PC71BM. PCDTBT is used because of its known operational stability [60]. All the fabrication steps were optimized until the cells achieved PCEs on par with previously published works [59]. Under 1-sun, our cells yield 6.2 ±0.2% PCE with open circuit voltage $V_{oc} = 924 \pm 3mV$, short circuit current density $J_{sc} = 12.1 \pm 0.1mA/cm^2$ and fill factor $FF = 56 \pm 2\%$ over an area of 0.475 cm^2.

Table 5.1: Light power corresponding to 300 lux illuminance emitted by three representative types of light bulbs (LED 3000 K, CFL 6500 K and incandescent bulbs 2800 K), and light power of a standard AM 1.5 G sun-light spectrum dimmed to 340 lux. Power generated by our organic solar cell exposed to these different light sources and the corresponding PCE, open-circuit voltage, short-circuit current and fill factor.

Light source and illuminance $[lux]$	**Corresponding light power** $[mW/cm^2]$	**Power generated by solar cell** $[\mu W/cm^2]$	**PCE** [%]	V_{oc} $[mV]$	J_{sc} $[\mu A/cm]$	**FF** [%]
Sun (340)	0.31	15.2	4.9	704	4.7	45
LED (300)	0.104	9.0	8.7	702	28.0	46
CFL (300)	0.18	20.7	11.5	738	53.5	53
Incandescent bulb (300)	0.633	3.8	0.6	645	16.5	34

Simulating indoor light

Throughout this work, light intensity is varied by inserting neutral density filters of known transmittance between the 1-sun (AM 1.5, 100 mW/cm^2) calibrated solar simulator and the solar cells. A power of 310 $\mu W/cm^2$ is used to represent indoor light. This power corresponds to 340 lx falling in the middle of the typical indoor illuminance range defined in the introduction. We compare the performance of a solar cell under 340 lx of AM 1.5 simulated light and under 300 lx light (since indoor light intensity is characterized by illuminance and not power) from light bulbs of the three different categories determined by Minnaert et al.: one incandescent light bulb of color temperature 2800 K, one 6500 K CFL bulb and one LED with 3000 K color temperature. The spectra of those four light sources and the absorption of the PCDTBT:PC71BM based cells are shown in Fig. 5.18. The performance of the solar cell under the different light sources are summarized in Table 5.1. The efficiency of the solar cell under the CFL and the LED is higher (11.5% and 8.7% respectively) than under dimmed sunlight (4.9%). In the case of the incandescent light bulb, the efficiency is significantly lower (0.6%) since a large part of the emitted light spectrum is out of the absorption range of the polymer blend. However, the absolute power generated by the solar cell under the four light sources are much closer. The lowest power per solar cell area is obtained for the incandescent light bulb (3.8 $\mu W/cm^2$) while the highest is obtained for the CFL (20 $\mu W/cm^2$). The incandescent light bulb emits a lot more power (0.63 mW/cm^2) to provide 300 lx of light, so despite the lower PCE of the solar cell under this source, the overall output power is similar to the others. Under 340 lx sunlight the cell generates 15.2 $\mu W/cm^2$ and has an efficiency of 4.9%, falling between the CFL and incandescent bulb. Based on these results, the 340 lx sunlight is used in the remainder of this work to represent indoor lighting.

Optimization of solar cells for indoor light

Previous studies on the operation of organic solar cells under low light intensity suggested that an important parameter to control is the shunt resistance. Proctor and Nguyen [64] report that for a shunt resistance (R_{sh}) lower than 1 $M\Omega - cm^2$ the JV characteristics of solar cells can be significantly affected by para- sitic leakage current for lights between 100 mW/cm^2 and 2 mW/cm^2. Steim et al. [75] show that a shunt resistance of at least 85 $k\Omega - cm^2$ is needed for operation under 1000 lx of a fluorescent lamp and that, overall, the performance of the solar cells under low light increases with higher shunt resistance. Zhou et al. [90] have also developed a solar cell which performs well under room light and exhibits a $R_{sh} = 10^8 \Omega cm^2$. Here, the thickness of the PEIE layer is varied in order to control the shunt resistance and optimize the organic solar cells for indoor light. Previous studies [89, 50] have shown that PEIE is an insulator which can modify the series resistance and the work function of the cathode as a function of its thickness. PEIE thickness has also been shown to influence the reverse bias saturation dark current in organic photodiodes [61]. Three sets of cells are made with three different PEIE thickness (thin, medium and thick) and their operation is compared under light intensities ranging from 100 mW/cm^2 to 10 $\mu W/cm^2$. A PEIE solution concentrated at 0.048 wt% in ethanol and spin-coated at 5000 rpm (medium thickness) was found to give optimal conditions under 1-sun light intensity, so the other PEIE thicknesses are chosen below (thin: 0.024 wt% solution of PEIE at 5000 rpm) and above (thick: 0.048 wt% solution at 1250 rpm) this optimal point. The exact thicknesses of the PEIE layer was not measured because its dimension is on the nm scale and would require extensive investigation to quantify. Instead, the concentration and rotation speed is used as a proxy for thickness. Figures 5.3-5.6 give the variation of the V_{oc}, J_{sc}, FF and PCE of representative cells from each group, while figures 5.8 through 5.10 give their JV characteristics for 1-sun, simulated indoor light (310 $\mu W/cm^2$) and in dark conditions. The shunt resistances, as extracted from the dark JV characteristics, are 3.3 $k\Omega - cm^2$ for the thin PEIE cell, 32 $k\Omega - cm^2$ for the medium PEIE, and 500 $k\Omega - cm^2$ for the thick PEIE cell. All cells have PCE falling between 5% and 6% under 1-sun (the medium thickness is the optimal one, Fig. 5.8), as they have similar V_{oc} and J_{sc} (respectively within 10 mV and 0.2 mA/cm^2 of each other). The only difference comes from their FF which can be linked to variations in the series resistance of the devices: the medium and thick PEIE have similar FF, 55% and 53% respectively and the thin PEIE FF equals only 48%.

The series resistance value of the thin PEIE cell is close to that of a device with no PEIE (direct contact between the active layer and aluminum). Therefore, it can likely be attributed to a less than optimal charge extraction due to too thin of a layer [50]. On the other hand, the thick PEIE cell has a slightly higher series resistance than the medium PEIE cell, suggesting that the insulating nature of the PEIE starts to be impactful. Under this light intensity, the difference in shunt resistances between the three cells has a negligible impact on the FF and the PCE. Overall, varying the thickness of PEIE has a limited effect over the cell efficiency under 1-sun. But the evolution of their PCE differs considerably when light weakens.

Under 1 mW/cm^2 of light, the thin PEIE shows a PCE of 2.1%, the medium PEIE a PCE of 7.4% and the thick PEIE a PCE of 8.0%. The medium PEIE cell has an R_{sh} lower than both minimal values recommended by Proctor et al. and Steim et al., and shows a high PCE under 1 mW/cm^2 of sunlight (1000 lx). This observation suggests that, because of variations from system to system, the shunt resistance may not be a criterion reliable

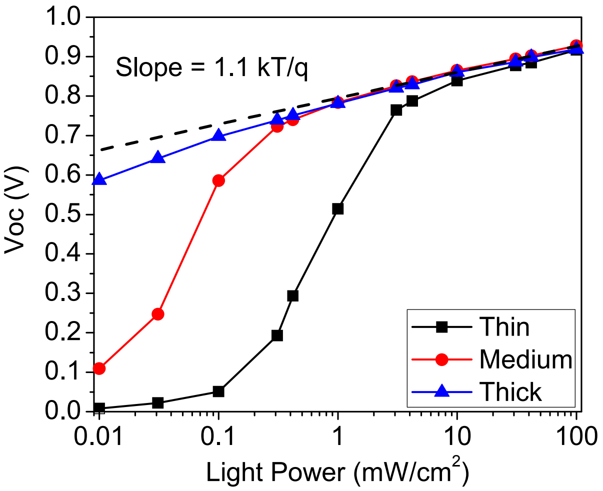

Figure 5.3: a

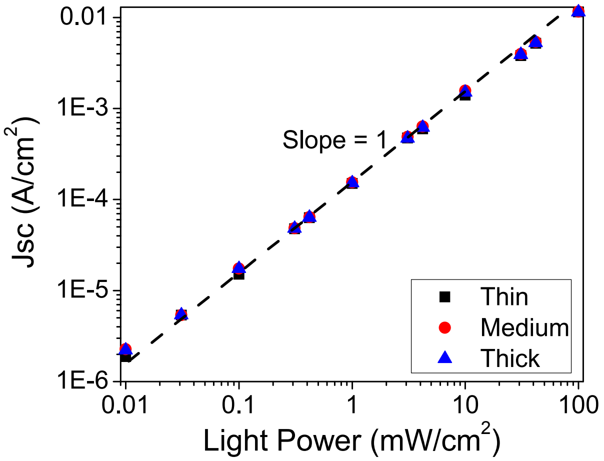

Figure 5.4: b

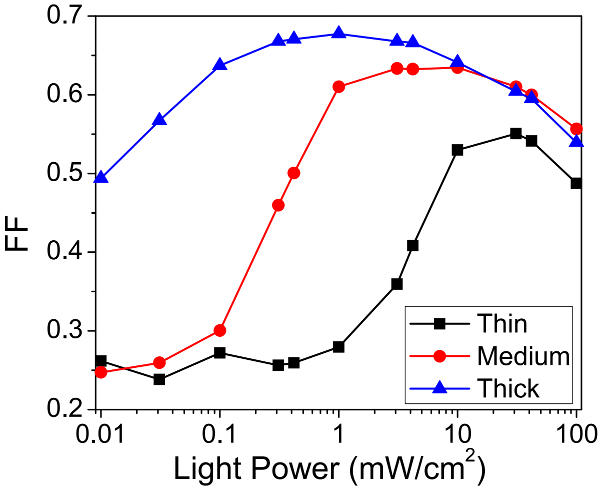

Figure 5.5: c

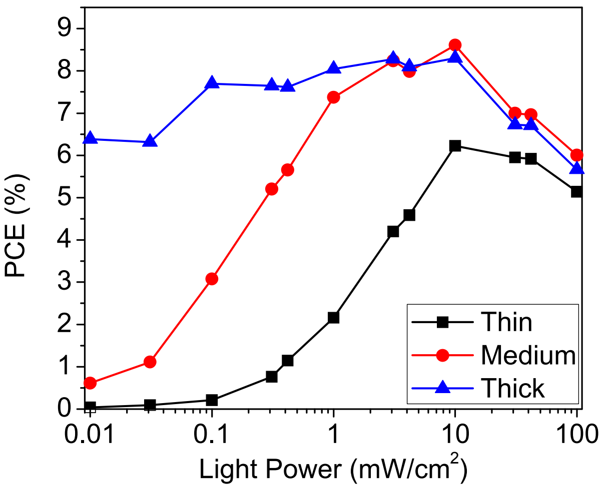

Figure 5.6: d

Figure 5.7: Dependence as a function of light intensity of a) the open-circuit voltage, b) short-circuit current, c) fill factor and d) PCE of solar cells with three different PEIE thickness(Thin, Medium, and Thick). The dotted lines represent linear trends with the indicated slope.

enough to determine how a device will perform under low light intensity. Under typical indoor light (310 $\mu W/cm^2$), the PCEs of the thin, medium and thick PEIE solar cells are respectively 0.7%, 5.2% and 7.6%. The discrepancy of operation under indoor light of the three cells is well seen in their JV characteristics (Fig. 5.9): the thin PEIE JV characteristic is dominated by leakage current resulting in low efficiency, the medium PEIE cell still has a regular diode characteristic but with significant leakage current, while the thick PEIE cell

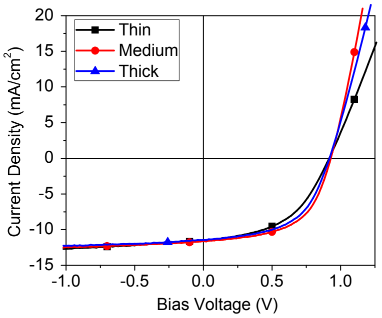

Figure 5.8: a

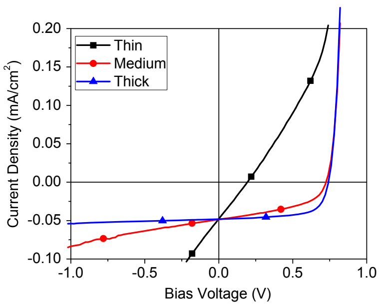

Figure 5.9: b

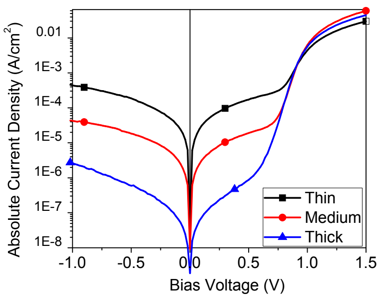

Figure 5.10: c

Figure 5.11: J-V characteriscics of three cells with varying PEIE thickness a) under 1-sun illumination, b) under simulated indoor light and c) in the dark.

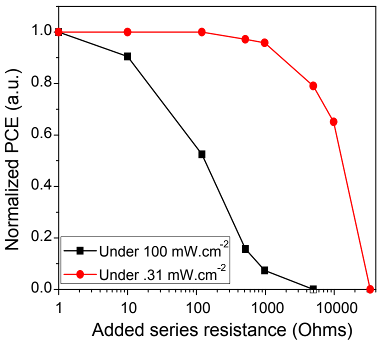

Figure 5.12: a

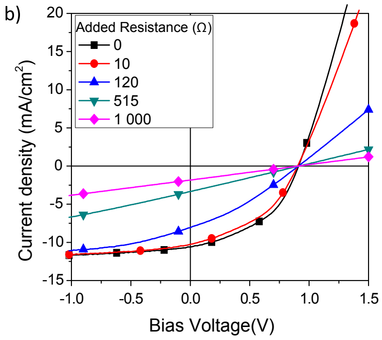

Figure 5.13: b

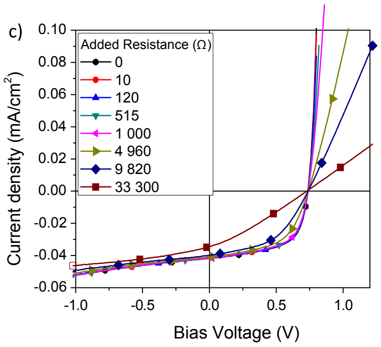

Figure 5.14: c

Figure 5.15: Effects of adding increasing values of resistance in series with an organic solar cell under 1-sun and simulated indoor light. a) Dependence of the PCE as a function of the resistance value. Because of the log-scale, the 1 Ω data points correspond to no added resistance. The black squares are data for 1-sun while the red dots are for indoor light. B) JV characteristics of the solar cell for different added resistance values under 1-sun and c) under simulated indoor lighting. (For interpretation of the references to color in this figure legend, the reader is referred to reference [48])

displays a diode curve with a high FF (superior to 60%). The short circuit current (figure 5.4) of all cells follow a linear decrease as a function of light power with a slope close to 1. The PCE variations with light power originate from the changes in V_{oc} and FF. The V_{oc} of all cells measured under 1-sun is 920 mV and first decline linearly with the logarithm of light power, with a slope that corresponds to an ideality factor of 1.1 [81]. The V_{oc} (figure 5.3) of the thin PEIE and medium PEIE cells do not follow the linear scenario at light intensities of 1-5 mW/cm^2 and 0.1-0.5 mW/cm^2 respectively. Similarly,the FF (figure 5.5) of the thin PEIE and medium PEIE cells decline sharply at the same light levels as for the V_{oc}. For both thin and medium PEIE, the V_{oc} and FF decreases occur at the light intensities for which the J_{sc} generated by the cells reaches the same order of magnitude as their dark currents (Fig. 5.10): the thin PEIE cell has a dark current of about $3 * 10^{-4} A/cm^2$ (at 0.5 V of bias) and the decline onset in V_{oc} and FF occurs for a light power (4.2 mW/cm^2) at which the cell's J_{sc} equals $6 * 10^{-4} A/cm^2$. Similarly for the medium PEIE cell, the decline occurs at a light power between 1 and 0.4 mW/cm^2, where the J_{sc} is between 15 and $6 * 10^{-5} A/cm^2$ while the dark current equals $2 * 10^{-5} A/cm^2$ (at 0.5 V). The thick PEIE cell has a dark current of $6 * 10^{-7} A/cm^2$ and does not show any significant decline in either V_{oc} or FF, even when the light falls as low as $10 \mu W/cm^2$, for which the J_{sc} is 2 $\mu A/cm^2$. These results demonstrate that solar cells intended for indoor operation need to be specifically optimized for these conditions. These results also suggest that the value of the dark current can be used to determine the minimal light power below which a cell's JV characteristic will start being significantly affected by the dark current, and therefore below which its efficiency will decrease dramatically. Assuming a 1:1 proportional decrease of the cell's current with light intensity [5], the ratio between the dark current (Jdark) and the J_{sc} under 1-sun should roughly equal the ratio between the minimal light power (P_{min}) and 100 mW/cm^2 (P_{1-sun}):

$$\frac{J_{dark}}{J_{sc}} = \frac{P_{min}}{P_{1-sun}} \tag{5.2}$$

The ratio of J_{dark} over J_{sc} is a more comprehensive criterion than the shunt resistance to control the performance of the solar cells under low light. For example, a solar cell with a 1-sun J_{sc} of 20 mA/cm^2 needs to have a dark current lower than 20 $\mu A/cm^2$ to be efficient under 0.1 mW/cm^2, which corresponds to a minimum R_{sh} of 25 $k\Omega - cm^2$. However, a cell generating only 2 mA/cm^2 under 1-sun needs a dark current lower than 2 $\mu A/cm^2$, or a R_{sh} higher than 250 $k\Omega - cm^2$ to be efficient under 0.1 mW/cm^2. The leakage/short-circuit current ratio criterion provides a useful tool to evaluate the indoor operation potential of solar cells already published. For example, the record cell of He and coworkers [33] has a dark current of approximately $10^{-4} mA/cm^2$ and a J_{sc} under 1-sun of 17 mA/cm^2. Therefore, the cell's performance should be significantly limited by dark current at a light power below 0.1 mW/cm^2. Steim and colleagues suggest that solar cells should have a series resistance lower than 50 $\Omega - cm^2$ for operation under lights of 1000 lx. Here, a solar cell with thick PEIE and 0.475 cm^2 of area is connected in series with external resistances ranging from 10 Ω to 33 $k\Omega$ (respectively 4.7 $\Omega - cm^2$ and 15.6 $k\Omega - cm^2$) and the JV characteristics for each resistance is recorded under 1-sun and 310 $\mu W/cm^2$. Fig. 5.12 shows normalized PCE as a function of added series resistance. Fig. 5.13 and 5.14 show the JV characteristics obtained under the 1-sun and simulated indoor lighting. Under 1-sun, the PCE shows a high dependence with series resistance, as it decreases rapidly with the increase of resistance, falling to less than 20% of its initial value at 515 Ω. Under simulated indoor-light however, the PCE is less dependent on series resistance. For a 1 Ω load (475 $\Omega - cm^2$), the PCE is above 95% of its value with no load, and it remains at 80% for 4.9 $k\Omega$ (2.3 $k\Omega - cm^2$), and at 65% for 9.8 $k\Omega$ (4.7 $k\Omega - cm^2$). Thus, under indoor-light, series resistance between 475 $\Omega - cm^2$ and 2.3 $k\Omega - cm^2$ do not influence the performance of the OSC. This implies that a different set of

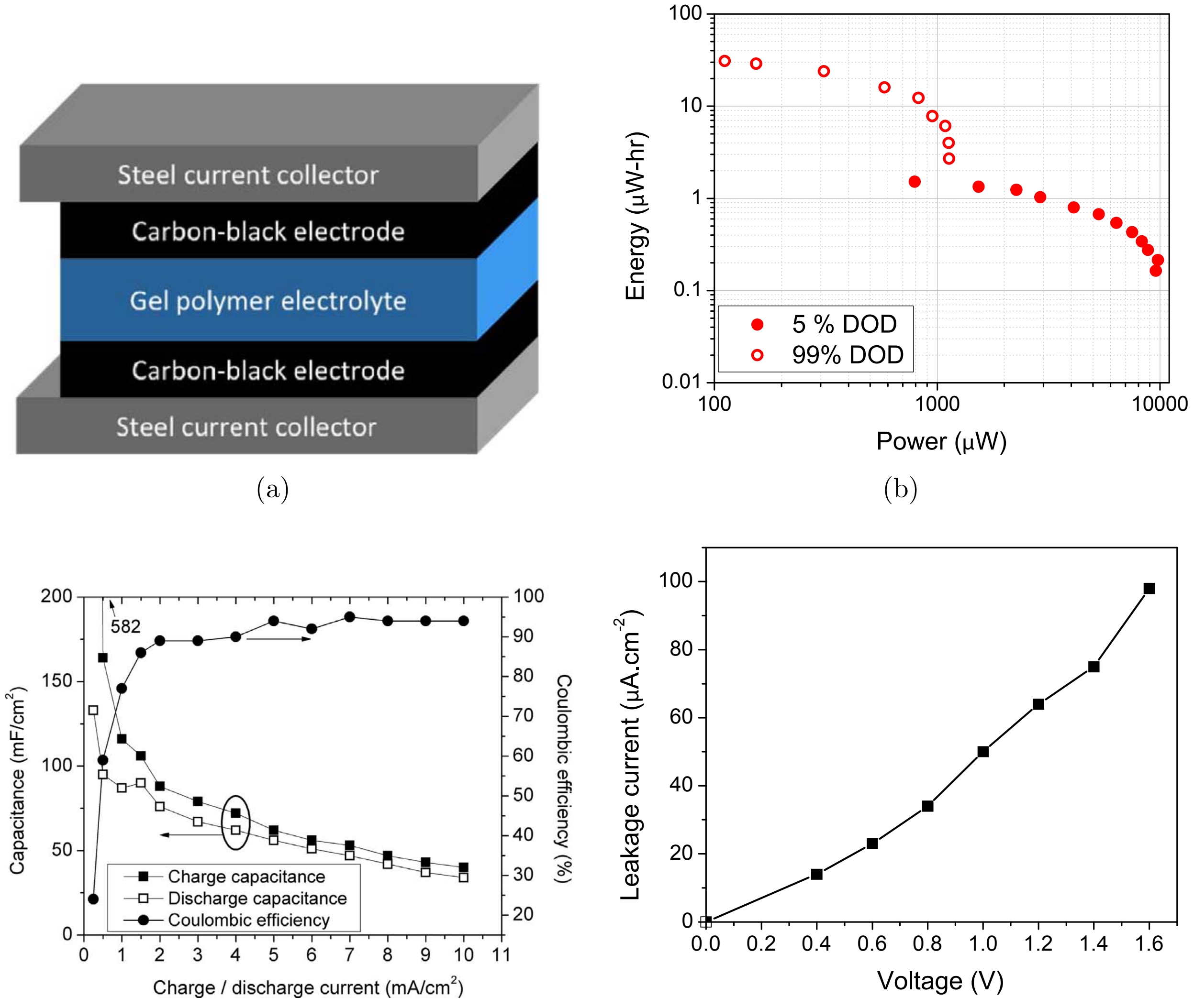

(a) (b) (c) (d)

Figure 5.16: a) Structure of the super-capacitor along with its b) Ragone plot, c) capacitance and coulombic efficiency as a function of the charge/discharge ccurrent and d) dependence of the leakage currents as a function of bias voltage.

criteria can be suitable for transparent electrodes. Under low light, optical transparency is more important than low resistivity, thus indium tin oxide (ITO) may not be the best choice anymore, as carbon based materials, for example, can offer better light transmittance [21, 58].

Fabrication and characterization of the super-capacitors

The super-capacitor needs to have certain qualities in order to be relevant for the specific application considered. First, it needs to store enough charges to power the WSN and be able to withstand many charge-discharge cycle. Ideally, it would also have the same advantages as the OSC, mainly printability and potential flexibility, and a comparable area. Here, the super-capacitors are all-printed. They consist of composite carbon electrodes sandwiching a gel polymer electrolyte as depicted in Fig. 5.16a with a 1 cm^2 area. The gel polymer acts as a porous separator between the electrodes and houses the ionic liquid electrolyte butyl-methyl-imidazolium tetrafluoroborate (BMIM BF4) allowing ion migration. The electrodes consist of a threefold composite of activated carbon (AC) (42.5 wt%), acetylene black (AB) (2.5 wt%), and graphite (GR) (5 wt%) held in a polymer binder of poly(vinylidine fluoride-co- hexafluoropropylene) (PVDF-HFP) (50 wt%). The constituents of these electrodes are chosen to provide both good electrical conductivity and mechanical strength. The high surface area of AC acts as the main component to support the electric double layer phenomenon responsible for the high-energy storage in super-capacitors. AB provides electrical pathways between AC grains and improves electrical conductivity within the electrodes. AB is present at the critical fraction to engender markedly improved electrical conductivity. Graphite's large repeating structural flakes provide mechanical strength and electrical conductivity within the electrode. Finally, the PVDF-HFP binder fraction lends mechanical flexibility to the super-capacitor, and its fraction must be considered a tradeoff between electrical performance and mechanical flexibility.

Performance testing of the super-capacitor is carried out before coupling with the solar cell to parameterize the response char- acteristics of the energy storage medium. Constant current charge and discharge is used while tracking the voltage response to determine the super-capacitor capacitance, series resistance, cycle energy and power. Characterization is done over the voltage range of 1.7 to 0.01 V. This voltage range provides insight about depths of discharge (DoD) up to 99.4% and fractions thereof. The super-capacitor was discharged at currents between 0.25 and 10 mA/cm^2 with higher discharge currents producing higher power, lower energy data points. The performance of the super- capacitors are constant even after a hundred thousand cycles, as previously reported [16]. The super-capacitor's series DC resistance is calculated to be approximately 40 Ω during charge and discharge transitions. The supercapacitor's energy and power relationship can be seen in the Ragone plot Fig. 5.16b, where discharging at varying powers and DoD influences the total energy that can be extracted. The 99% DoD curve is seen at about ten times higher energy than the 5% DoD, peaking at 31 $\mu W - hr$ (111.6 mJ). Meanwhile, the 5% DoD curve exhibits higher power by about an order of magnitude, maximizing at 9.8 mW.

Fig. 5.16c shows the capacitance and the coulombic efficiency (ratio of the discharged vs charged amount of charge) of the super-capacitors as a function of the charge and discharge current densities. The highest discharge capacitance, 130 mF/cm^2, was observed for a charge/discharge rate of 0.25 mA/cm^2. The capacitance increases when the currents are weaker because ions have more time to find optimal packing along the surface of the porous electrode and move deeper into the surface convolutions, in ac- cordance with the porous electrode theory [55]. While the coulombic efficiency remains above 90% for much of the current range, it drops sharply for current densities lower than 1 mA/cm^2, likely because of leakage. Super-capacitors inherently show leakage currents when a voltage exists between

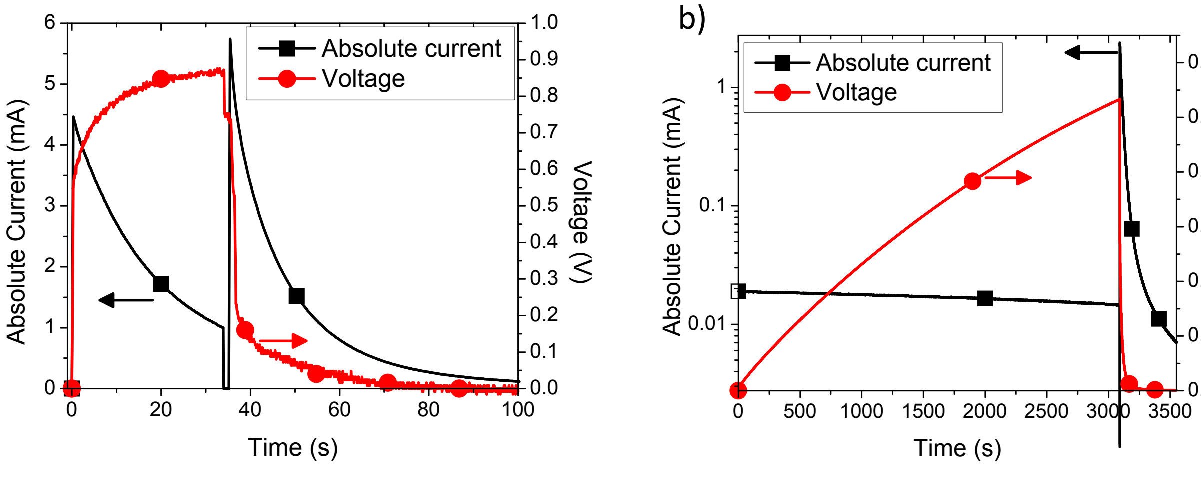

(a)

(b)

Figure 5.17: Typical variations of the absolute current flowing through the super-capacitor (black squares) and voltage across it (red dots) during the charge discharge experiment of a photo-rechargeable system comprising a solar cell optimized for indoor operation and a super-capacitor. a) Under 1-sun light, where the charge stops after 35 s and b) under simulated indoor light, where the charge stops after 3090 s. (For interpretation of the references to color in this figure legend, the reader is referred to reference [48])

the super-capacitor's electrodes. Leakage current increases with increasing voltage often approximated as a resistor in parallel with the super-capacitor electrodes [91]. The leakage characteristics of our printed super-capacitors are measured by holding them at a constant voltage and measuring the corresponding current at steady state. The leakage current as a function of bias voltage can be seen in Fig. 5.16d. As expected, the leakage current increases almost linearly with voltage, for a high value of almost 0.1 mA/cm^2 for 1.6 V of bias, which corresponds to a resistance of 16 $k\Omega - cm^2$.

Overall, these super-capacitors offer a wide range of operation in terms of power and cycle energy, in line with the power and energy needs of the low-power autonomous devices identified in the introduction. Their low leakage current and high capacitance make them suitable for integration with the OSC developed in the previous section.

Characterization of the energy harvester system

To demonstrate the potential for energy harvesting of a photo-rechargeable system combining the OSC and super-capacitors, charge-discharge experiments are performed under 1-sun and indoor light. A solar cell (0.475 cm^2) either with medium or thick PEIE, a super-capacitor and a 120 Ω resistance are connected in parallel (Fig. 5.2). Switches allow isolation of each component. The current flowing through the super-capacitor and the voltage across it are recorded in real time throughout the experiment. At the start, the super-capacitor is fully discharged. In the first phase, only the OSC and the super-capacitor are connected. Light of either 100 mW/cm^2 (1-sun) or 310 $\mu W/cm^2$ (typical indoor) is shone on the solar cell.

When the system starts to saturate, the super-capacitor is disconnected from the OSC, briefly isolated and connected to the resistive load for discharge. Identical experiments performed with 1 Ω, 10 Ω were compared with the 120 Ω and did not yield any significant difference in the results (about 2% Table 5.2). The total amount of charge extracted are calculated by integrating the discharge current over time. The effective capacitance of the super-capacitor is calculated as the ratio of extracted charges and the maximum voltage V_{max} of the isolated super-capacitor after charge. The stored energy is then derived as $E = \frac{CV_{max}^2}{2}$. The maximum power extracted is calculated as the product of current and voltage at the very beginning of the discharge. Finally, the ECSE is calculated as the ratio of stored energy and light energy received during the charge phase. Fig. 5.17 shows the voltage and current flowing through the super-capacitor during a typical charge-discharge experiment under 1-sun (Fig. 5.17a) and simulated indoor light (Fig. 5.17b) using the solar cell with thick PEIE. In both cases, the voltage starts at 0 V and the current is the short-circuit current of the solar cell. As the voltage rises, the output current of the solar cell corresponds to its JV characteristic.

In the 1-sun case, the voltage quickly saturates, reaching 870 mV in 28 s, 50 mV below the V_{oc} of the solar cell. Simultaneously, the current decreases from 4.5 mA (the short-circuit current) to below 1 mA. As a result, the charge is stopped after 35 s. A visible voltage drop occurs when stopping the charge (from 870 mV to 740 mV), indicating an equivalent series resistance of 130 Ω, three times higher than expected from the earlier characterization of the super-capacitor. The current peaks at the start of the discharge phase, reaching 5.7 mA, and very quickly decreases, as does the voltage. It should be noted that more than 70% of the total amount of charge are extracted during the first second of discharge.

Under simulated indoor light, the system behaves quite differently. Over a charge period of 3000 s, the voltage rises steadily while the current is mostly stable, between 18 and 15 mA. When charging stops, the final voltage is 530 mV, well below the V_{oc} of 740 mV and no voltage drop is visible. In this case, the limiting factor is the leakage current of the super-capacitor, estimated to reach approximately 15 μA at 500 mV of bias voltage. During discharge, 50% of the total stored charges are extracted within 1 s and more than 90% after 2 s. The trends identified here are representative of all the other charge/discharge experiments performed in this work. These observations suggest several guidelines for improving the system's operation: under strong light, it is preferable to have as high a V_{oc} as possible (possibly with cells connected in series or using a tandem) [79] in order to maximize the amount of energy stored in the super-capacitor. At lower light intensity however, the priority should be to increase the current of the solar cell (by improving the EQE or the absorption, or using tandem cells connected in parallel for example). Minimizing the leakage current and series resistance of the super-capacitor is also paramount to maximize energy harvesting.

To investigate the influence of the solar cell efficiency on the ECSE, such charge-discharge experiments in the two lighting conditions are performed three times each using either a medium PEIE solar cell (optimal under 1-sun) or thick PEIE one (optimal for indoor light). Table 5.3ab summarizes the performances of the two systems. The charging time under 1-sun is 35 s, while it is kept at 900 s in indoor conditions to ensure that the super-capacitor's leakage current does not impact the results. Under 1-sun, the systems with the two cells perform nearly identically. The total energy extracted is 26 mJ for both of them at a maximum power of 4 mW. These energy and power levels are exactly in the range needed to power the active mode of the WSN ($110mJ$ and $110mW$). The ECSE of the two systems reach 1.56%, the highest to date for photo-rechargeable systems using OSC. When the two systems are compared under indoor light for 900 s, the ECSE amounts to 1.07% for the system with the medium PEIE and to 1.21% with the thick PEIE. Using the solar cell optimized for indoor light thus yields a 15% improvement in the ECSE of the photo-rechargeable system and this improvement is passed on to the other metrics, as the maximum power and extracted energy also boast a 15% improvement. However, the extracted energy and power are an order of magnitude lower than under 1-sun. This can partially be explained because after 900 s, the voltage across the super-capacitor is still very low ($< 200mV$) and the energy stored into a super-capacitor varies with the square of the voltage. Moreover, work by Xu and co-workers [83] suggests that the ECSE of a given system (and thus the stored energy) depends highly on the charging time.

To verify if charging for a long time under indoor light would allow the storage of similar levels of energy and power as the 1-sun scenario, the charging time is increased to 3090 s (Table 5.3c). The maximum voltage attained is 530 mV, the extracted energy is 13.3 mJ and the maximum power 1.26 mW. These levels are of the same order of magnitude as under 1-sun and are therefore suitable for low-power applications. It is noteworthy that, between those two experiments, the light power was decreased 300-fold and the charging time only increased 88-fold, yet the energy stored in the indoor scenario is half that of the 1-sun scenario. If the system had behaved linearly, only one-third would have been expected. This is promising for indoor-applications: photo-rechargeable systems behave in a non-linear manner that narrows the gap between high and low light intensity. This will be critical to reduce the charging time needed under low-light. As a result, the ECSE reaches 2.92%. Interestingly, the coulombic efficiency (calculated by comparing the quantity of charges that flowed into and out of the super-capacitor during the charge and discharge steps) in these experiments equals 95%, suggesting that the leakage current of the super-capacitor is much lower than anticipated. Overall, these results demonstrate that OSC coupled with super-capacitors are well-suited to cover the energy needs of low-consumption devices, even when operating in low-light environments such as indoors. This opens up new, industrially-significant, perspectives of applications for organic solar cells, where the constraints are considerably different from the usual outdoor photovoltaic installations.

Conclusion

In conclusion, organic solar cells for indoor operation need to be specifically optimized for these conditions. Particularly, achieving a low dark current is essential to maintaining a high

Table 5.2: Comparison of charge-discharge experiments of a 1 cm^2 OSC under 1-sun and a super-capacitor with three different discharge loads: 1 Ω, 10 Ω and 120 Ω. The super-capacitor is charged until its voltage is within 30 mV of the OSCs V_{oc} and the delivered current is lower than 100 μA. As a result, even if the charges generated are a bit different, the charges extracted vary less than 2%.

Load [Ω]	**Charging Time** [s]	**Maximum V** [mV]	**Charge Generated** [mC]	**Charge Extracted** [mC]
1	30.2	895	56.8	52.4
10	26.9	900	55.3	51.2
120	26.3	900	53.2	52.1

Table 5.3: Comparisons of the photo-rechargeable systems using either a solar cell optimized for 1-sun operation (medium PEIE) or for indoor operation (thick PEIE), under either 1-sun light (100 mW/cm^2) or simulated indoor light (0.31 mW/cm^2). Indication of the charging time, the maximum voltage across the super-capacitor at the start of discharge, the total quantity of charges, total energy and maximum power extracted from the super-capacitor during discharge. Energy conversion and storage efficiency of the whole photo-rechargeable system calculated from the previous values.

	Solar cell	**Light power** [mW/cm^2]	**Charging time** [s]	**Maximum voltage** [mV]	**Extracted charge** [mC]	**Extracted energy** [mJ]	**Maximum power** [mW]	**ECSE** [%]
a	Medium PEIE	100	35.1 ± 0.1	730 ± 5	71.2 ± 0.2	26.0 ± 0.2	4.06 ± 0.07	1.56 ± 0.01
	Thick PEIE	100	35.1 ± 0.1	730 ± 5	71.7 ± 0.2	26.2 ± 0.2	4.16 ± 0.04	1.57 ± 0.01
b	Medium PEIE	0.31	900 ± 0.2	160 ± 5	18.2 ± 0.1	1.42 ± 0.06	0.19 ± 0.01	1.07 ± 0.04
	Thick PEIE	0.31	900 ± 0.1	170 ± 5	19.0 ± 0.1	1.61 ± 0.06	0.22 ± 0.01	1.21 ± 0.04
c	Thick PEIE	0.31	3090 ± 0.1	530 ± 5	50.0 ± 0.3	13.3 ± 0.2	1.26 ± 0.02	2.92 ± 0.02

PCE under low light intensities. Optimizing the thickness of the PEIE layer is an efficient way of controlling the dark current and cells with PCE of 7.6% under simulated indoor light were demonstrated. The ratio of dark current over short-circuit current was identified as a reliable indicator of the minimal light power below which a cell's efficiency decreases sharply. Fully-printed super-capacitors were developed, showing a maximum discharge capacitance of 130 mF/cm^2, and provided a maximum power of 9.8 mW/cm^2, and maximum energy of 31 $\mu W - hr/cm^2$. Those super-capacitors were integrated with OSC to form photo-rechargeable systems. Under 1-sun light, such systems had 1.56% of ECSE and generated 26 mJ of energy and up to 4 mW of power. Under simulated indoor light, photo-rechargeable systems using OSC optimized for indoor operation yielded 15% more energy per cycle than those using OSC optimized for 1-sun. The indoor-optimal photo-rechargeable system charged under indoor light for 3090 s provides energy and power levels similar to the 1-sun scenario, and reaches 2.92% of ECSE. Overall, these results suggest that organic solar cells have a good potential to power autonomous applications in various light environments.

5.2 Demonstration: Indoor Light, Single Reservoir, Voltage Triggering Algorithm

Indoor ambient light is a readily available source of energy for microelectronic devices, but its low power density has typically meant it is not considered for wireless sensor node (WSN) applications [76]. We extend prior literature on indoor photovoltaic energy harvesting by fabricating and demonstrating a wireless sensor node in which a spectrum-tailored organic solar cell is used to charge a supercapacitor, which in turn intelligently powers a radio payload using a state-based control strategy.

Application Environment

Because solar cells are generally optimized for outdoor use, their performance is traditionally measured under 1-sun standard irradiance of 100 mW/cm^2 with AM 1.5G spectrum. However, indoor conditions differ considerably from this conventional scenario. First, indoor light intensity is characterized in illuminance, as seen by the human eye. Standard indoor illumination at 300 lux corresponds to $100 - 500$ $\mu W/cm^2$ irradiance depending on the light source. Second, the light spectrum is very different than the sun. The absorption spectrum of organic photo-active materials is well-suited to absorb indoor light spectra, so they are a natural solution for indoor light harvesting. Figure 5.18 illustrates that the solar cells absorption spectra overlaps well with high fractions of LED and CFL emission spectra. By tailoring the energy harvester to the intended environment, we are able to operate in very low power-availability environments.

Indoor lighting intensity in workspaces and industrial settings is internationally regulated and must be above a minimum threshold [19, 74]. This lighting level is adequate to power our WSN with a periodicity below one minute, a frequency applicable for intermittent sensing applications like environmental monitoring.

Our system

Harvesting with organic solar cells

Organic solar cells (OSC) currently achieve more than 10% power conversion efficiency (PCE) under 1-sun conditions [76, 19] and can be stable over several years [74, 48]. The materials involved in their fabrication can be completely printed on flexible substrates, allowing the use of large- area, high-throughput, low-cost manufacturing processes such as roll-to-roll

---

Work reported on in this section has been published as "Wireless sensor node demonstrating indoor-light energy harvesting and voltage-triggered duty cycling" in the 2016 article of the Journal of Physics: Conference Series 773 by authors Martin A. Cowell, Balthazar P. Lechene, Pierluigi Raffone, James W. Evans, Ana C. Arias, and Paul K. Wright. This work is included with permission.

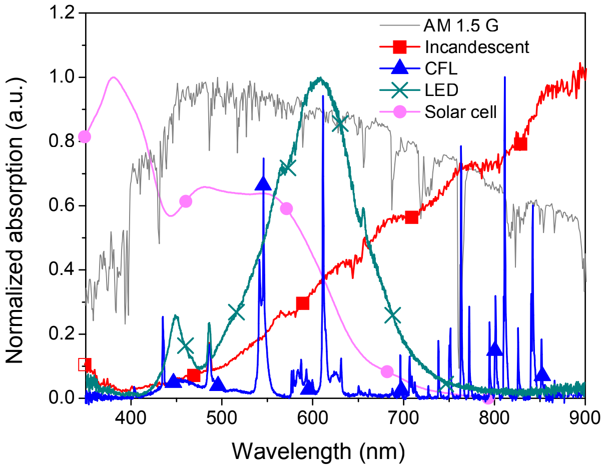

Figure 5.18: Normalized power spectra of the different light sources studied: 1-sun AM 1.5 G (line), incandescent light bulb 2800 K (red squares), CFL 6500 K (blue triangles), LED 3000 K (green crosses), and the normalized absorption spectrum of the solar cell (pink dots).

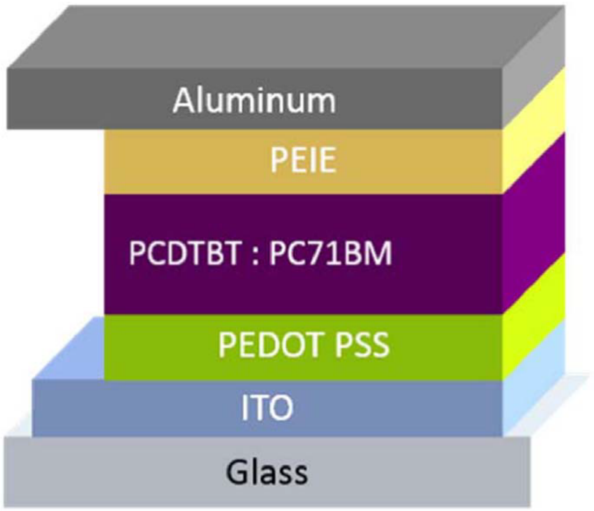

Figure 5.19: Architecture of the solar cells used in this work.

printing. Here, OSCs based on the blend of poly[N-9-heptadecanyl-2,7-carbazole-alt-5,5-(4,7-di-2-thienyl- 2,1,3-benzothiadiazole] (PCDTBT) and [6,6]-phenyl-C71-butyric acid methyl ester (PC71BM) (1:3.7 in ortho-dichlorobenzene with 5% dimethyl sulfoxide) are chosen. The architecture of the cell is shown in figure 5.19 and the fabrication followed the procedure described in [48]. We leverage spectrum-tailored OSCs to make the best use of indoor ambient energy, and are able to continuously harvest 20 $\mu W/cm^2$ [48].

For a given light source, the light power (P_{min}) at which a solar cell will stop performing well can be linked to its short circuit current (J_{sc}) under $P_{100} = 100\ mW/cm^2$ by: $J_{dark}/J_{sc} \approx P_{min}/P_{100}$. In order to optimize OSCs for indoor light, it is critical to maintain their dark current as low as possible. Control of the dark current can be achieved by varying the thickness of the top polyethylenimine ethoxylated (PEIE) layer. Figure 5.20 shows the evolution of the PCE of PCDTBT:PC71BM solar cell under an AM1.5G light source and a standard LED light source for varying light intensities. The cells have a dark current of 2 $\mu A/cm^2$ at a bias of -0.5 volts, while their J_{sc} under 1-sun is 12 mA/cm^2. As a result, they achieve more than 4% of power conversion efficiency under 10 $\mu W/cm^2$ of AM 1.5G light, from 5.4% under 100 $\mu W/cm^2$. Moreover, because of the adequacy of the absorption spectrum of PCDTBT:PC71BM, those solar cells under an LED light source demonstrate PCEs between 7% and 15%. Figure 5.21 shows the typical J-V curve of the PCDTBT based solar cells under typical indoor conditions: 340 lux of either AM1.5G light (corresponding to 310 $\mu W/cm^2$) and LED light (corresponding to 124 $\mu W/cm^2$ of power). The maximum power produced by this cell is 15.75 $\mu W/cm^2$ under LED light and 19.6 $\mu W/cm^2$ under AM 1.5G. Despite the almost three-fold difference in light power, the solar cell provides similar amounts of power under them.

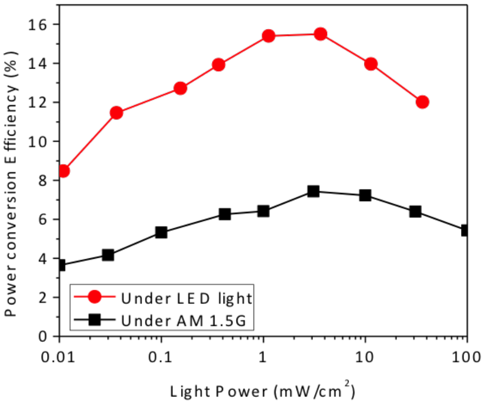

Figure 5.20: Evolution of PCE for the solar cell under LED and AM1.5G sources.

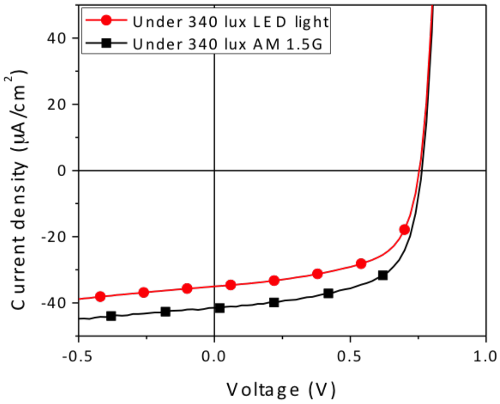

Figure 5.21: JV curve of our solar cell under 340 lux from LED and AM1.5G sources.

Supercapacitor

To meet these power demands, energy harvested from the OSC accumulates in the high-power energy reservoir of a printed carbon supercapacitor [16, 47] for use during radio transmission. Figure 5.22 shows our reservoir is able to supply 9.8 mW/cm^2 of reservoir footprint, and therefore a minimum supercapacitor footprint of 2.2 cm^2 is necessary to meet the radio power demands. It is important to avoid oversizing the supercapacitor in this low-power harvesting environment to mitigate leakage currents. An excessively leaky reservoir can quickly make the WSN inoperable in low-power harvesting environments. We leverage printed supercapacitor manufacturing because it enables the energy storage parameters to be tailored by controlling footprint geometry, layer thickness, and parallel or series inter-cell connections.

Load Demand: Radio and Sensor

We selected Nordic Semiconductors Bluetooth low energy radio NRF51822 for its low peak-power demands. This 2.4 gigahertz transceiver is seen transmitting 56 packets in figure 5.24 while drawing 6.9 mA peak current at 3.2 volts. The peak power of these transmissions is therefore 22 mW, nearly 1000 times the available power from the OSC. The radios sleep current is 3 μA. Additionally, we avoid energy-costly handshaking protocols by transmitting data using advertising packets. NRF51822 can operate at voltages from 1.8 to 3.6 volts. To measure accelerations, we used the low power 10 bit accelerometer ADXL345 from Analog

Devices sensing at 200 Hz with 145 μA current consumption. By leveraging these low operating and sleep currents, were able to best mitigate the costs of performing our sensing and transmission protocols.

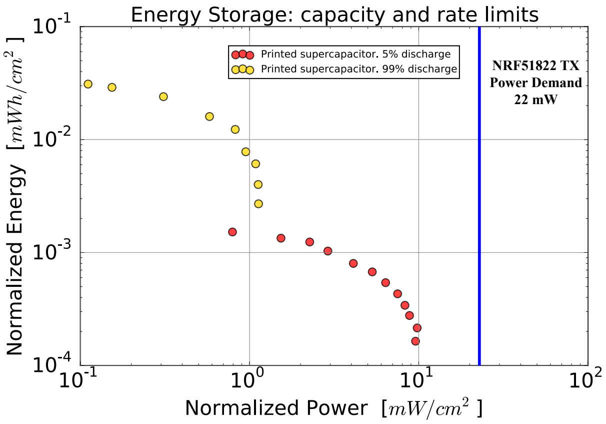

Figure 5.22: Ragone plot: power capabilities of printed supercapacitor. NRF51822 max power requirement is blue vertical line.

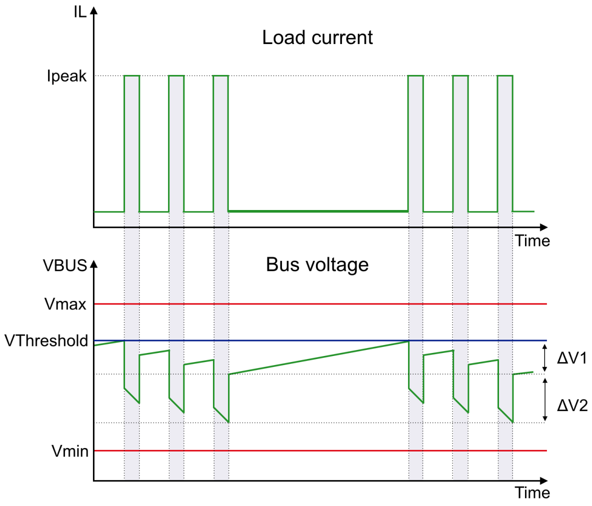

Figure 5.23: Acquisition and transmission is triggered once the threshold voltage is reached.

Triggering Algorithm

We implement a triggering algorithm wherein the WSN lies dormant until the energy stored in the supercapacitor is adequate to power sensing and transmission protocols. The WSN cold-starts when the radio's low voltage bound is reached at 1.8 volts and immediately enters a sleep state. The supply voltage continues to scale linearly as the supercapacitor accumulates charge. The WSN wakes periodically to measure the reservoir's bus voltage (V_{bus}). Once (V_{bus}) exceeds a threshold voltage, the WSN senses from the accelerometer and transmits via advertising packet. The triggering voltage must be above the cold start voltage plus the worst case voltage drop $\Delta V1 + \Delta V2$ seen in figure 5.23.

In our tests, the coulombic cost of acquisition and transmission are calculated to be 2.2 mC. This provides a $\Delta V1$ voltage drop of 55 mV for a supercapacitance of 40 mF. Our peak current of 6.9 mA produces a $\Delta V2$ Ohmic drop of 280 mV. These voltage drops sum to 335 mV. To provide an adequate safety factor for our demonstration, we set the triggering voltage to 2.3 volts, 500 mV above our cold-start voltage.

Demonstration

We show a functional WSN in figure 5.25 that integrates a printable organic solar cell and printed supercapacitor to power the WSN in indoor light. Power is managed with a simple voltage-based triggering algorithm that only enables data acquisitions and transmission once the supercapacitor is adequately charged. This demonstration shows time-series acceleration data being transmitted to a base station where it is processed to view the frequency response.

Conclusion

With this work we demonstrate a wireless sensor node capable of running exclusively on indoor light, illustrating feasibility for nodes that can operate autonomously in low-light and indoor environments.

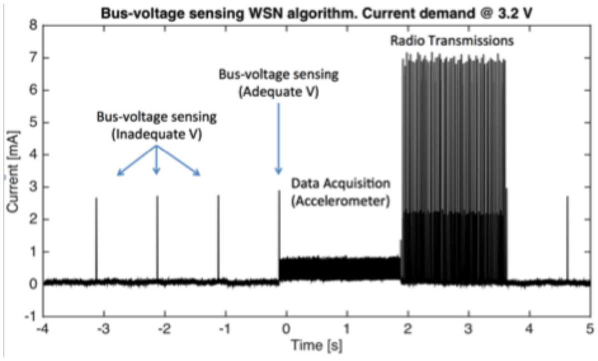

Figure 5.24: Voltage-dependent triggering protocol. Sensing and transmission only occurs when bus-voltage threshold is reached.

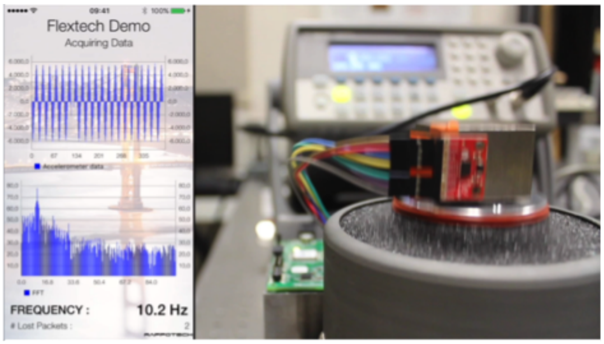

Figure 5.25: Frequency processing of data acquired from sensor mounted on voice coil oscillating at 10.2 Hz.

Chapter 6

System Modeling of Energy Harvesting Sensor Node

6.1 Energy and Information Flows

The operation of an energy-autonomous wireless sensor node (EAWSN) relies on careful consideration of the energy flow within the device. Following the energy flow seen in figure 6.1 illustrates the distribution of energy from the power management unit (PMU) to the functional devices of the WSN: the microcontroller unit (MCU), the sensor, and the radio. The functional devices are the final sink of energy within the system. Tracing the energy

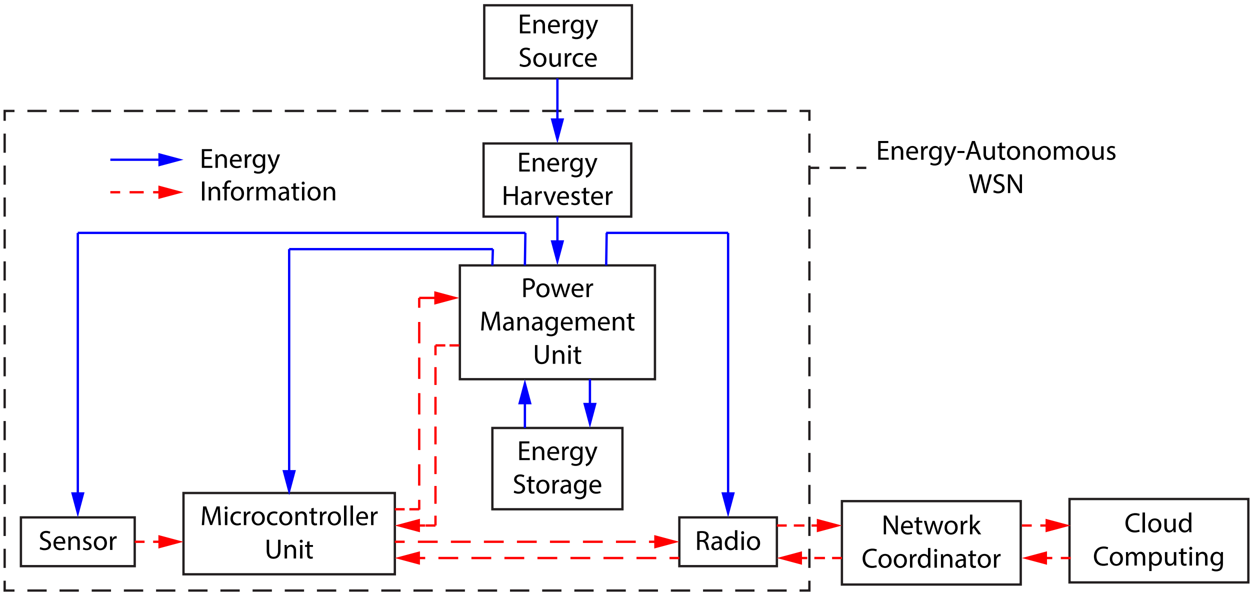

Figure 6.1: Energy flow and information flow diagram of an energy-autonomous wireless sensor node operating in a coordinated network and reporting to the cloud.

flows backward, we see that the WSN's electrical energy is generated at the energy harvester and can be stored in and withdrawn from the energy reservoir. All the transactions between harvester, storage, and functional devices are managed by the PMU.

The purpose of the WSN is to collect sensor data and transmit it to the cloud. This function is managed by the MCU which queries the sensor, stores the data, and packages it for the radio to transmit. Via the radio, the data passes out of the WSN to the network coordinator which then passes the data on to cloud computing. The function of the WSN is simple and straight forward, but its operation in a finite energy environment requires monitoring and planning to implement effectively.

To perform in a variable harvesting energy environment, the energy-autonomous WSN must understand time varying nature of its energy availability. To monitor energy availability, the MCU collects information about the time varying nature of the energy source from the PMU and transmits energy metrics to the cloud for analysis. Machine learning techniques can be performed on the cloud and transmitted back to the WSN which allow the WSN to understand features and foresee predictable characteristics of the energy source. Observing the nature of the energy source with this off-line technique, the WSN can adjust its behavior to be more aggressive or more conservative across future time.

The reliability of individual nodes within a network can also be determined as a function of time as nodes report their time dependent energy availability and the characteristics of their energy storage reservoirs. Predicting reliability of networked nodes enables improved planning for more reliable networked communication.

Properly sizing energy harvesting and reservoir components is an important consideration when designing WSNs to operate in time varying energy environments. While oversizing these components can provide higher node reliability in some cases, oversizing can also extend start-up time while rechargeable reservoirs fill from empty, and oversized energy components contribute to higher device cost. Undersizing energy components can result in poor power reliability, and in the extreme case, complete failure to operate. To identify the optimal size of energy harvesters and reservoirs, two approaches are considered below.

6.2 Optimal Sizing: Dynamic Programming

This study focuses on creating a tool for optimized system design of centimeter scale, printed, flexible wireless sensor nodes. Current work uses printed Sb_2Te_3 and Bi_2Te_3 thermoelectric generators [53] for energy harvesting, rechargeable printed Zn and MnO_2 batteries [35] for energizing a low-power Firestorm microcontroller, and printed composite carbon supercapacitors [16] for high power communications via a Nordic radio. These components have been characterized individually, but their integration into a single device as a unified power platform is not optimized - resulting in over sized components and excess device footprint. The design tool discussed here examines current work as described above but can be easily extended beyond this specific system, allowing node designs that harvest energy from light, motion, or others, and sense temperature, light intensity, chemical presence, humidity,

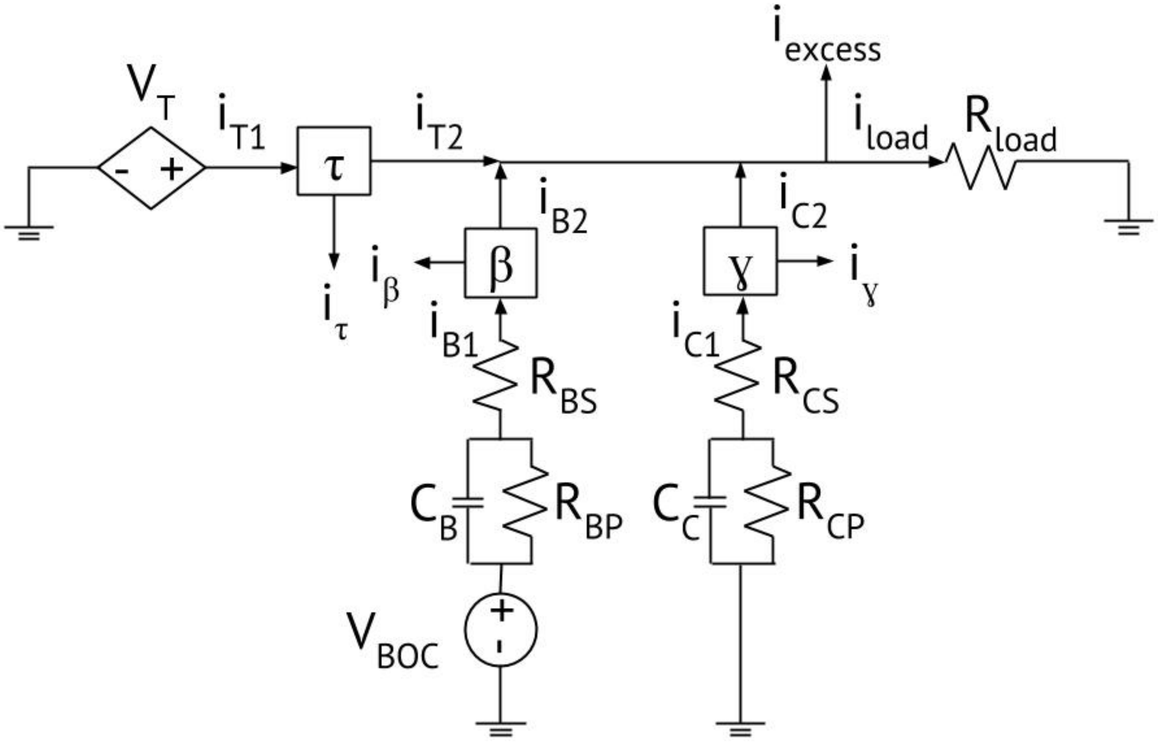

Figure 6.2: First-order equivalent circuit model of dual reservoir energy harvesting system. Lossy voltage regulators ensure the bus voltage is met by each reservoir and harvester.

vibration, or others. Microcontroller, sensor, and radio duty cycles all contribute to the power demands of a wireless sensor node, so this novel design tool will allow for engineered exploration of the node feasibility space using printed electronics for energy harvesting and storage. Modeling the first-order equivalent circuits that describe sub-components within the wireless node provides insight into the transient behavior of the power platform. Understanding this transient behavior is important in ensuring that current and potential at the load node never move outside the design specifications required by the load.

Unfortunately, by including these equivalent circuits the system becomes complex to the point of eluding a problem description that is fully explained by convex mathematics. Without a convex form, this problem must be solved with Dynamic Programming (DP) and therefore becomes computationally intensive and time consuming. The simplified model see in figure 6.3 has removed the circuit diagrams in favor of basic tank reservoirs for the

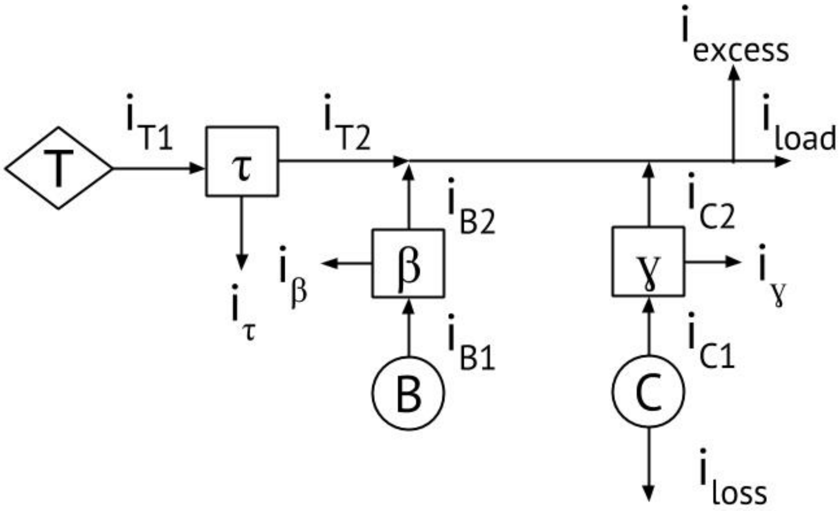

Figure 6.3: Simplified energy flow diagram of dual reservoir harvesting system. Energy stored in leaky reservoirs is transfered via lossy regulators.

battery and supercapacitor. The leakage current of the supercapacitor is taken into account with i_{loss} and uses parallel resistor values found in lab testing. Before optimizing the size of the generation and reservoirs, the optimal current dispatch must be determined for a given time-series load demand. This deterministic load demand is fed into the DP to determine the optimal current dispatch.

Dynamic Programming achieves optimal current dispatch by observing all possible combinations of reservoir charge states and reservoir currents for the entire time domain in the load demand and selecting the control action that minimizes the magnitude of the cost of proceeding from the first time step to the end. The cost in this case is the magnitude of charge transferred from the excess source/sink. For a given generation and reservoir size, the current i_{T2} is constant and the currents i_{B2} and i_{C2} are limited. These limitations demand that an excess current term be defined for Kirchhoffs current law to be upheld at the node leading into the load. If the current generated exceeds the sum of currents that can be ab-

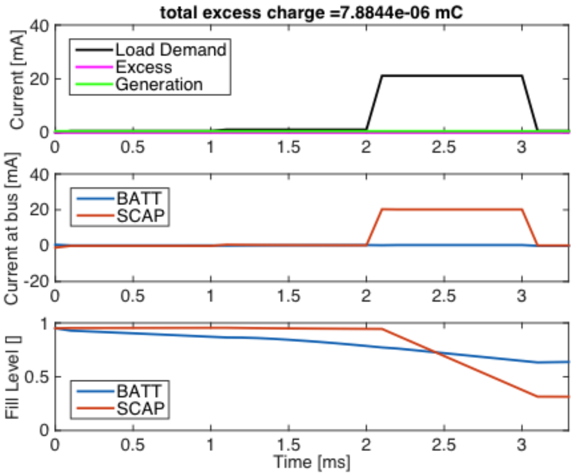

Figure 6.4: Testing oversized reservoirs

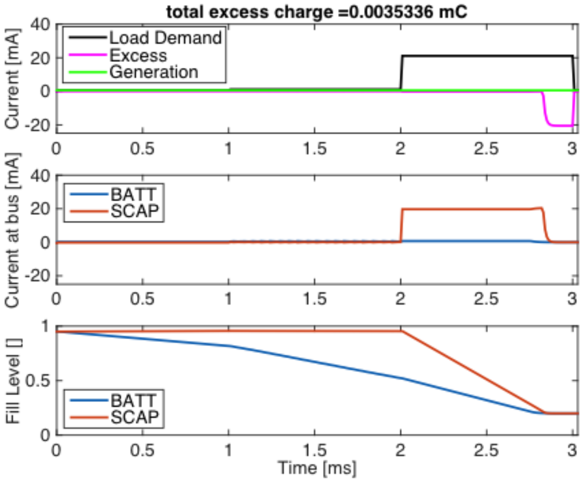

Figure 6.5: Testing undersized reservoirs

sorbed by the reservoirs and the load, then the excess current is positive. If the load current cannot be met by the sum of generation and reservoir currents then the excess current is negative.

At each time step, lower and upper bounds are placed on the control variables (i_{B2} and i_{C2}) in accordance with their rate limitations and their minimum and maximum charge capacities as seen in lab testing. Bi-directional voltage regulators are seen in figure 6.3 as boxes τ, β, and γ are assumed to have constant efficiency losses in the form of current losses. Once the DP finds the full feasible control (current) and state (charge) space, a simulation is given initial conditions, stepping forward in time to provide the optimal control actions at each time step. To illustrate the change in reservoir charge state over the tested load regime, the current limitation density of the reservoirs $[mA/cm^2]$ found in lab experiments were replaced with an absolute current limit [mA]. While this is not representative of a real-world printed energy reservoir, this allowed the capacity of the reservoirs to be tailored independently of their current limitation for testing purposes. Once the reservoir behavior is verified to be accurate to the model, the current limitation density is reinstated in the model returning system accuracy to the model. The load demand in figures 6.4 and 6.5 is representative only in magnitude to that expected from the radio described above while the peak durations are shortened to one millisecond for initial testing purposes.

In figure 6.4 the supercapacitor (SCAP) and battery (BATT) reservoirs are over sized. The SCAP discharges from 95% full to 31% full over the course of the 3 ms load regime, while the BATT discharges from 95% full to 64% full over the same period. In figure 6.5 the reservoirs are undersized, resulting in their lower charge limit being reached at a time of 2.8 ms. The excess current source supplies the remaining load because the generation and reservoirs are not able to meet demand. This model finds optimal current dispatch and can easily be modified to find the optimal generator and reservoir sizes by wrapping the

Table 6.1: Component characteristics - experimentally determined

	Current Limit mA/cm^2	Capacity C/cm^2
TEG	0.1084	N/A
BATT	0.0900	1.087
SCAP	10.00	0.1020

Table 6.2: Load demand

	Load Demand mA	Duration ms
Sleep	0.1084	Varies
Data Acquisition	0.0900	1.087
Transmission	10.00	0.1020

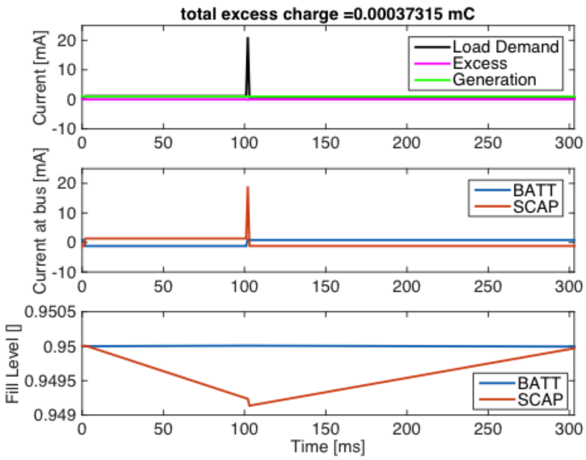

Figure 6.6: Simulation representative of printed generation, printed reservoirs, and loads of interest

Table 6.3: Component sizes providing indefinite load stability

Component	Size
TEG	10 (50 leg devices)
BATT	12.5 (cm^2)
SCAP	2.11 (cm^2)

DP in reservoir and generator size grids and minimizing excess charge transfer and the sum of reservoir footprints. This will increase the computational time by a factor equal to the number of grid points in the three- dimensional generation and reservoir matrix. With the results from figure 6.4 and figure 6.5 indicating that the DP model is capable of achieving optimal current dispatch, the model is put to the test by including lab- based capacity and current limit parameters for generation and reservoir components. The quantities found through experimentation are listed in table 6.1.

Note, the TEG current limit was found for a temperature difference of 35 $^{\circ}C$ and is representative of a single 50 leg device as described in [8], while the supercapacitor parameters are calculated from continued work described in [16]. Additionally, the leakage currents seen in the SCAP reservoir are characteristic of a parallel resistance of 20 $kOhm$. The load demand curve used in the subsequent tests is described in table 6.2. With these parameters and load demands, the DP finds the optimal current dispatch for a printed sensor node as described in the Focus of this Study section on page 2.

The top plot in figure 6.6 shows the time series load demand of a node power cycle from sleep through data acquisition and transmission. Excess current is minimized, and its integral is expressed at the top as 373 nC over the 302 ms cycle. The second plot indicates the current contribution from the BATT and SCAP at the load bus. The SCAP supplies current during data acquisition and transmission, and charges during the sleep period following transmission. The BATT reservoir is seen following the opposite charge regime charging during data acquisition and transmission, and discharging during sleep. The bottom plot emphasizes the overly large capacity of both the BATT and SCAP reservoirs. The SCAP current limit of 10 mA/cm^2 requires the SCAP area to be 2.11 cm^2, but this SCAP area produces an enormous charge capacity that is only depleted by 0.1% over the course of the transmission cycle. The BATT reservoir charges during data acquisition and transmission and discharges during sleep. The printed battery was initially included in the power platform to provide current during data acquisition, but this current demand is instead met by the supercapacitor. This observation indicates that the printed battery component may be superfluous for this load demand case.The minimum cycle time in this simulation as just over 300 ms. After this length of sleep following a load cycle described in table 6.2, the SCAP reservoir is back to its initial fill level of 0.95 and can undergo a duplicate load cycle while achieving zero net energy.

The reservoir fill levels return to their initial state at the end of simulation indicating that the load cycle can be repeated indefinitely with component sizing seen in table 6.3. The model examined above has provided enormous insight into the current dispatch capabilities of a dual reservoir power platform for wireless sensor node applications and provides a baseline for sizing the printed reservoir and generation components for continued research efforts. As it stands today, the model lays a foundation for two further studies. The first opportunity is to build a non-convex model that monitors voltage as a node state for critical nodes seen in the first order equivalent circuit model of figure 6.2. An advanced model like this leverages the mathematical relationships seen in the following section Equivalent circuit models, and should first assume of constant model parameters to further inform the power platform designer. The second opportunity builds on the non- convex model described above by incorporating non-linear parameters for the circuit elements in figure 6.2. These non-linear parameters include:

C_C dependence on i_{C1}

R_{CP} dependence on VCC

V_{BOC} dependence on SOC

V_T - dependence on i_{T1}

Voltage regulator efficiency dependence on ΔV and i

Equivalent circuit models

The equivalent circuit model of a semiconductor-based thermoelectric generator is described as a variable voltage source in series with a resistor [51]. Five physical processes dictate the performance of the variable voltage source:

Kirchhoff's Voltage Law

$$V_{TEG} = IR_m + \alpha_m \Delta T \tag{6.1}$$

Heat conduction

$$q = -\frac{\Delta T}{2\Theta} \tag{6.2}$$

$$\Theta = \frac{L}{2kA} \tag{6.3}$$

$$\Theta_m = \frac{\Theta}{N} \tag{6.4}$$

Where:

q is heat transfer in a leg

ΔT is temperature difference across leg couple

Θ is thermal resistance of leg couple

L is length parallel to heat transfer

k is thermal conductivity constant

A is cross s ection of the leg

Θ_m is total thermal resistance in a device

N is number of legs in a device

Joule Heating (Resistive Losses)

$$R = \rho \frac{2L}{A} \tag{6.5}$$

$$R_m = RN \tag{6.6}$$

Where:

R is electrical resistance of couple

R_m is electrical ressitance of device

ρ is material resistivity [Ohm-meter]

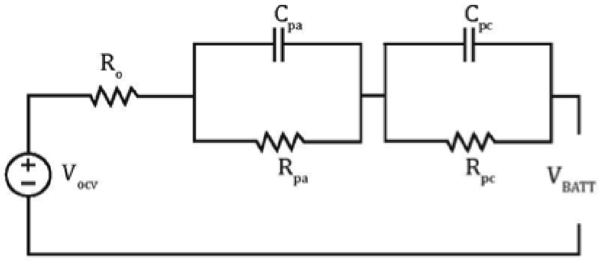

Figure 6.7: Second order equivalent circuit of battery reservoir.

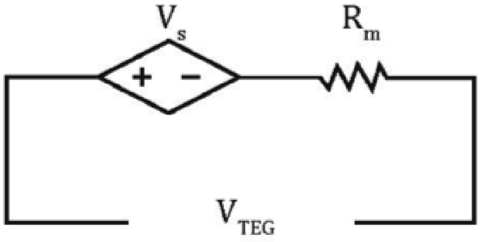

Figure 6.8: Equivalent circuit diagram of thermoelectric generator

Seebeck Power Generation

$$\pi = \alpha T \tag{6.7}$$

$$\alpha_m = \alpha N \tag{6.8}$$

These physical properties allow for a fully dynamic model to be derived. A few assumptions can be made to simplify the list of equations necessary. First, the hot and cold side temperatures can be assumed to be constant. This eliminates the need for the heat transfer equations listed above, reducing our equations to Kirchhoffs voltage law, joule heating, and Seebeck effect.

Battery

Battery polarization voltage is characterized by two phenomena the concentration and electrochemical polarizations [42]. This second order RC model accounts for these two phenomena separately. Using Kirchhoffs laws, two current nodes and one voltage loop can be used to determine the characteristic equations for a battery.

$$\frac{V_{pa}}{R_{pa}} = i - C_{pa}\frac{dV_{pa}}{dt} \tag{6.9}$$

$$\frac{V_{pc}}{R_{pc}} = i - C_{pc}\frac{dV_{pc}}{dt} \tag{6.10}$$

$$V_{BATT} = V_{OCV} - iR_o - V_{pa} - V_{pc} \tag{6.11}$$

Where subscripts $_{pa}$ represent electrochemical polarization characteristics, and subscripts $_{pc}$ represent polarization characteristics due to concentration. While this model provides resolution of two distinct physical phenomena, a simplified first order model is likely accurate enough to describe the system for our purposes. Such a first order model will remove one capacitor/resistor pair, and reduce the number of Kirchhoffs equations necessary to define the system by one.

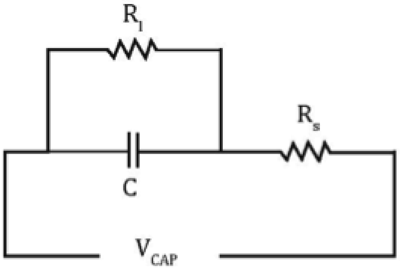

Figure 6.9: First order equivalent circuit diagram of supercapacitor reservoir.

Supercapacitor

Non-ideal supercapacitors are represented by an ideal capacitor in series and parallel with resistors that represent real-world phenomena. Series resistance accounts for ion adsorption time dependence and internal electrical resistances, while the parallel resistor accounts for leakage currents across the supercapacitors electrolyte layer. Kirchhoffs laws are similarly used to describe the equivalent circuit.

$$\frac{V_c}{R_l} = i - C\frac{dV_c}{dt} \tag{6.12}$$

$$V_{CAP} = iR_s + V_c \tag{6.13}$$

Experimental Data

Supercapacitor Discharge Range: Single printed supercapacitors of 1 cm^2 footprint have been manufactured in our lab and subjected to constant current charge/discharge regimes over a range of currents from 1 to 10 mA. The capacitor is subjected to 30 cycles of each current regime to aid in statistical relevance. Figure 6.10 illustrates the supercapacitors capacitance dependence on charge and discharge current. Such non-constant parameters are rarely considered in system modeling. These laboratory results can be used to elucidate the non-constant capacitance to be used in the advanced equivalent circuit model.

Supercapacitor Leakage

Leakage current tests have been performed on the above-mentioned printed supercapacitor over the expected range of the supercapacitor (see figure 6.11).

These tests will elucidate the non-linear relationship of the parallel resistance parameter.

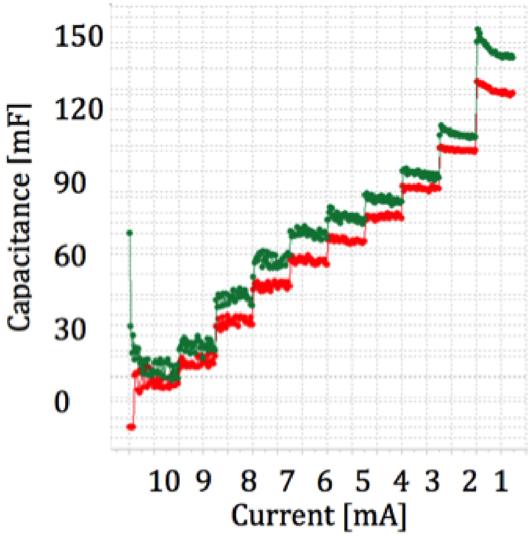

Figure 6.10: Supercapacitor capacitance dependece on charge and discharge rate (non-constant)

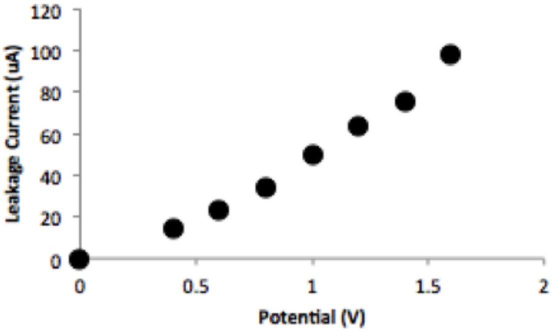

Figure 6.11: Voltage dependence on leakage current in supercapacitor reservoir

Discussion

The DP developed in this model gives the system designer the ability to peer into the time-series response of the energy reservoirs of the power platform for printed wireless sensor nodes. Collected lab data is used to identify parameters of the printed supercapacitor, printed battery, and printed thermoelectric generator. As the model exists now, it forgoes state and control dependent parameterization, however further opportunities have been identified for including these real device nonlinearities. Identification of the equivalent circuit models for individual components and their characteristic equations is outlined herein. The diagrams electrical connections within the power platform and the system of equations that describes the power platform is the basis of this model.

Summary

The project produces an optimal current dispatch tool that informs printed wireless sensor node design and lays the foundation for a device footprint optimization tool. Such a tool empowers the Industrial Internet to bring about global abundance. Understanding the feasibility space of application-specific sensor nodes enables optimized system design and leads to footprint reduction on the scale necessary for economic ubiquitous sensor networking. The original deliverables for this project highlighted system integration modeling to identify optimum system requirements for tailored printed sensor designs and to ascertain simplified use configurations. The power platform model discussed here achieves these goals and has already obviated a simple use case wherein the battery reservoir is eliminated. Two topics are identified for further modeling: First, the inclusion of the node voltage state space for key nodes in the power platform (referred to as the equivalent circuit model). Second, the expansion of the equivalent circuit model via non-constant and nonlinear parameterization of circuit elements will be further modeled. This second topic is made possible with laboratory test data from the Advanced Manufacturing for Energy Lab at UC Berkeley.

6.3 Optimal Sizing: Particle Swarm Optimization

Energy management systems for wireless sensor nodes must deliver reliable power and voltage while being small and low-cost. In prior literature, power reliability is maintained by using active energy management components (voltage regulators, DC/DC converters), but these impose efficiency losses [41] while increasing device cost and size [77, 32]. While the use of an active energy management system allows for a convex formulation of the optimal sizing problem in a two-reservoir battery/capacitor system [39], the passive energy management problem is nonconvex and has not been explored in prior literature.

Building on previous work developing flexible printed batteries [46], capacitors [16], and generators [8, 48] we propose a design which eliminates the need for active power management, and instead passively maintains device performance through optimal sizing of generators, batteries, and supercapacitors. To overcome the nonconvexity in this problem, we employ a Particle Swarm Optimization (PSO) algorithm to identify an optimal design [63], and are able to demonstrate a significant reduction in system size while meeting all payload power requirements.

Novel Contributions

This work extends prior literature on energy management in energy harvesting systems in the following ways:

- Demonstrates a method for designing a passive energy management system without the use of voltage regulators or DC/DC converters, and
- Applies particle swarm optimization to microelectronic energy management system design.

Work reported on in this section has been published as "Optimal component sizing in a two-reservoir passive energy harvesting system" in the 2016 article of the Journal of Physics: Conference Series 773 by authors Eric Munsing, Martin A. Cowell, Scott Moura, and Paul K. Wright. This work is included with permission.

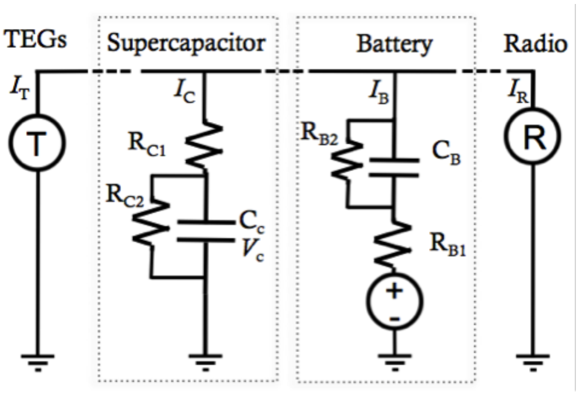

Figure 6.12: Equivalent Circuit Model; the design can be adjusted by changing the number of TEG elements in series in each string, or adding parallel TEG strings, supercapacitors, or batteries in parallel.

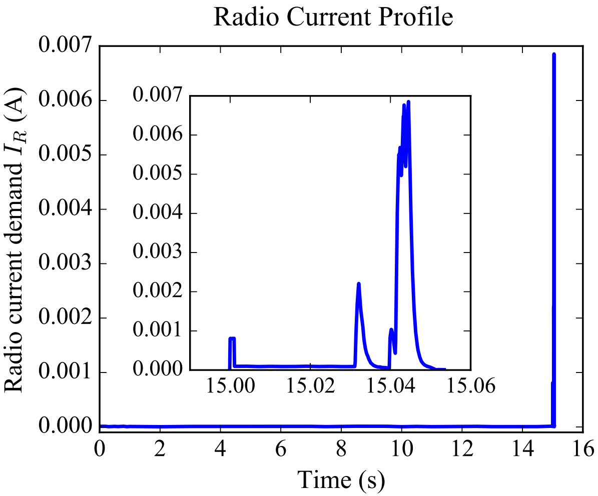

Figure 6.13: Radio power draw, with inset detail of the data acquisition/transmission period.

System Model

We consider a circuit model shown in figure 6.12 in which power is harvested through strings of thermoelectric generator cells (TEGs) in series; the approach we consider can also accommodate photovoltaics or other energy harvesting modes [48]. Charge is stored in parallel banks of supercapacitors and batteries; the components are linked by a main bus at voltage V. A radio is attached to the bus, and is modeled as a current sink with 15-second cycles with a deterministic current profile. The radio current draw I_R is shown in figure 6.13: a 15-second inactive period is followed by a 50 ms data acquisition and transmission load. We seek to design an energy management system which can repeat this load cycle indefinitely.

The system designer chooses the number of TEG elements in series s, number of TEG strings in parallel p, number of batteries b, and number of capacitors c. As the batteries have a low current capacity and supercapacitors have low energy capacity, we expect that an optimal design may include both storage reservoirs. We assume that each component has a constant per-unit cost, captured in the TEG unit cost α, battery unit cost β, and supercapacitor unit cost γ; the net system cost is thus $\alpha ps + \beta b + \gamma c$.

The system dynamics can be derived through the application of Kirchoff's Current and Voltage Laws (KCL and KVL) and a simple battery model where open circuit voltage OCV is linearized within the acceptable ranges of State Of Charge $\mathrm{SOC}_{\mathrm{min}}$ and $\mathrm{SOC}_{\mathrm{max}}$. These governing equations and limits on variables are captured below, where italic fonts are used to denote optimization variables:

$$\min \quad \alpha ps + \beta b + \gamma c \tag{6.14}$$

$$\text{Subject to:} \qquad \text{KCL for circuit:} \quad pI_T + cI_C + bI_B = \mathrm{I_R} \tag{6.15}$$

$$\text{TEG dynamics:} \quad I_T + \frac{1}{s} V\zeta = \mathrm{T_0}\Delta\mathrm{K} \tag{6.16}$$

$$\text{KVL in Capacitor:} \quad V + I_C\mathrm{R_{C1}} - V_C = 0 \tag{6.17}$$

$$\text{KCL in Capacitor:} \quad \dot{V}_c + \frac{1}{\mathrm{C_c}} I_C + \frac{1}{\mathrm{C_c R_{C2}}} V_C = 0 \tag{6.18}$$

$$\text{KVL in Battery:} \quad V + I_B\mathrm{R_{B1}} - V_B - OCV = 0 \tag{6.19}$$

$$\text{KCL in Battery:} \quad \dot{V}_B + \frac{1}{\mathrm{C_B}} I_B + \frac{1}{\mathrm{C_B R_{B2}}} V_B = 0 \tag{6.20}$$

$$\text{Battery OCV linearization:} \quad OCV - \nu SOC = \mathrm{V_0} \tag{6.21}$$

$$\text{Battery Charging/Discharging:} \quad I_B - I_{BC} - I_{DC} = 0 \tag{6.22}$$

$$\text{Battery State of Charge Conservation:} \quad S\dot{O}C + \frac{\eta}{\mathrm{Q}} I_{BC} + \frac{1}{\eta \mathrm{Q}} I_{DC} = 0 \tag{6.23}$$

$$\text{Inequality Constraints:} \quad b, c, s, p \geq 0 \quad , \qquad \mathrm{V_{cutoff}} \leq V \leq \mathrm{V_{max}} \tag{6.24}$$

$$\mathrm{I_{Cmin}} \leq I_C \leq \mathrm{I_{Cmax}}, \quad \mathrm{I_{Bmin}} \leq I_B \leq \mathrm{I_{Bmax}}, \qquad \mathrm{I_{Bmin}} \leq I_{BC} \leq 0 \quad , \qquad 0 \leq I_{BD} \leq \mathrm{I_{Bmax}} \tag{6.25}$$

System Design

Conventional Engineering Calculations

We expand on the methods in [77, 32, 49, 73] to provide a baseline estimate of system design using conventional engineering calculations.

To calculate the number of TEG elements in series within each string, and number of TEG strings in parallel, we use the linear TEG dynamics found in equation (3) and consider a constant temperature difference $\Delta\mathrm{K} = 20$. We determine the number of TEGs in series by dividing the nominal bus voltage by the midpoint voltage of the TEG output curve found in [8]. Similarly, we calculate the necessary number of parallel TEG strings by dividing the average WSN current demand by the midpoint current of a single TEG module.

We calculate the number of supercapacitors required to ensure that maximum payload current $\mathrm{I_{max}}$ can be satisfied without violating $V \geq \mathrm{V_{cutoff}}$. We estimate the minimum number of parallel supercapacitors by dividing $\mathrm{I_{max}}$ by the maximum current a single supercapacitor is able to deliver, $\mathrm{I_{Cmax}}$. We then verify that the combination of coulombic voltage drop and Ohmic voltage drop at $\mathrm{I_{max}}$ will not depress the bus voltage below $\mathrm{V_{cutoff}}$.

Because the current limit of the batteries is 2.5% that of the supercapacitors, the battery's contribution to the radio's current demand during peak discharge is assumed to be negligible.

Instead, the battery is sized such that it will be able to provide a nominal baseload power, here considered as 10% of $\mathrm{I_{max}}$, and has sufficient capacity to trickle charge the supercapacitor over the cycle should the TEG power drop.

Particle Swarm Optimization

Particle Swarm Optimization is a nonlinear optimization method in which a large number of particles explore the parameter space to identify a low-cost solution [63]. We consider an optimization space in the state variables $SOC(0)$, $V_C(0)$, and $V_B(0)$ in addition to the design variables variables p, s, b, and c. We provide a brief description of our implementation below; additional details can be found in [63] and associated references.

We assign a set of n particles to random locations and velocities in the optimization space, and use the equations above to simulate the system dynamics at each particle's coordinates. If constraints are violated a high penalty is assigned, and the total cost (penalty plus the value of the objective function) is saved for that point. After simulating the system at each particle's location, the location of the lowest-cost point is broadcast to all particles in the swarm. The velocities of all particles are then updated as the weighted sum of the particle's own velocity and the vector to its own best location and the swarm's overall best location. The process is repeated until the swarm converges on a low-cost point, though this may not be the global optimum.

Results

The results for both design methods are shown in table 6.4 and the resulting bus voltage during the data transmission period is shown in figure 6.14. We assume that a constant per-unit cost for each component, $\alpha = \beta = \gamma = 1$. We see that both designs are feasible, though the nonlinear optimization method converges on a solution which does not use batteries and more closely tracks the system constraints. This contributes to a 55% decrease in the number of components required to power the payload. Note, this figure assumes the value of each type of component is the same and does not account for differences in size between the geometry of the TEG and the supercapacitor. Also note, this does not account for the monetary cost difference between the three types of components. To account for the difference in material costs, the normalized cost per unit area should be applied for each component by changing the weighting coefficients α, β, and γ.

A number of other demand profiles were considered, including those in which the TEGs were not able to produce power for a portion of the load cycle. In these scenarios, the nonlinear optimization resulted in a design in which batteries are added to maintain bus voltage through the drop in generation.

We note that the convergence rate of the nonlinear optimization is dependent on the penalty function, and was found to slow significantly for longer study periods.

	Engineering Calculations	Nonlinear Optimization
Battery Cells	3	0
Supercapacitors	2	3
TEGs in series	50	22
TEG strings	1	1
Total units	55	25

Table 6.4: System designs resulting from conventional engineering and optimization-based approaches; a 55% decrease in cost is shown.

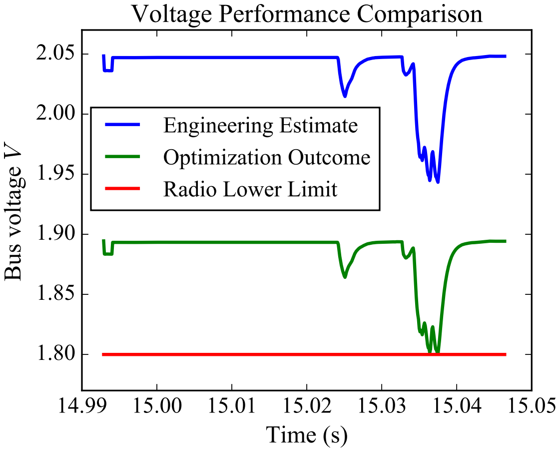

Figure 6.14: Bus voltage during radio dispatch, showing how the nonlinear optimization reduces costs by operating closer to system bounds.

Conclusions

We demonstrate a method for energy management in a wireless sensor node which does not require the use of voltage regulators or DC-DC converters, instead satisfying payload requirements through optimal component sizing. Using particle swarm optimization, we find a design with significant reductions in system cost relative to conventional engineering calculations. While this nonlinear optimization technique does not guarantee a globally optimal design, it can be readily applied to other demand profiles and generation/storage technologies and we expect that similar results may be found in other energy management problems.

6.4 Stochastic Modeling (necessitated by real-world conditions)

To understand and predict the variability of available energy for solar harvesting, we examine a dataset of solar irradiance collected in the field. The data are available from NRELs South Park field station and cover a period of 13.8 years from 2003 to present. Representative data are collected on five-minute intervals, which provide resolution to observe short-term events like cloud cover (fig 6.15), medium-term events like the diurnal cycle of the sun (fig. 6.15), and long-term events like season changes. By examining daily cycles and binning into seasons we are able to examine the five-minute mean and variance of solar irradiance for the four seasons. By considering this seasonal five-minutely data, we create a probability density function that obeys the mean and variance of the dataset (fig. 6.16,6.17). With this

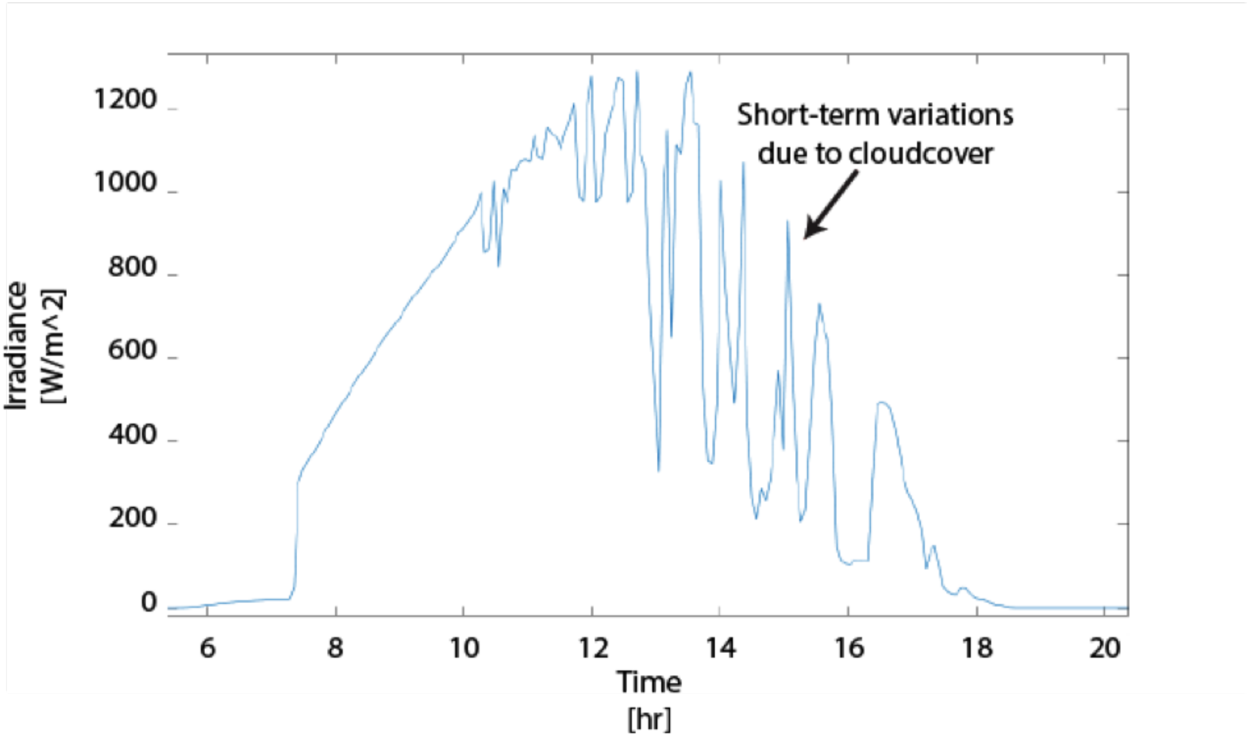

Figure 6.15: Example summer day from NREL's South Park CO field station.

time-series probability density function we are able to create random days that obey the statistical nature of the dataset (fig. 6.18).

6.5 Reliability metric

By feeding temporally varying energy availability into the equivalent circuit model of the WSN and applying the voltage triggering algorithm, we have a model that predicts the behavior of our energy autonomous WSN over the course of a day. Because the model applies the voltage triggering algorithm described in the system integration chapter, this model is able to dynamically adjust its duty cycle to adapt to the input energy availability. Starting the day before sunrise and with a depleted energy reservoir, the WSN is completely off. As the sun rises, the photovoltaic system begins to create a net positive energy flow and the energy reservoirs begin to charge. At the first threshold voltage, the system enters sleep mode and periodically wakes to check the power bus voltage. Once the second threshold voltage is reached, the system has adequate stored energy to undergo a data acquisition and transmission procedure followed by power bus voltage measurement and sleep.

Because this model accepts solar availability as its input, we are able to observe the sensor node responding to periodic cloud cover throughout the day. By considering the ratio of the WSN's actual up time to the length of the day, we are able to find the fraction of

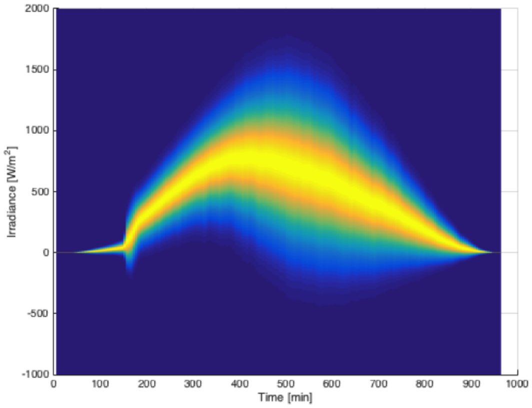

Figure 6.16: Aggregate summer days over 13.8 year period at South Park field station

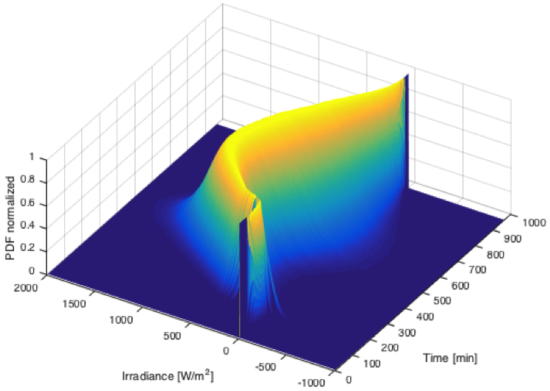

Figure 6.17: Probability density function of solar intensity during summer day

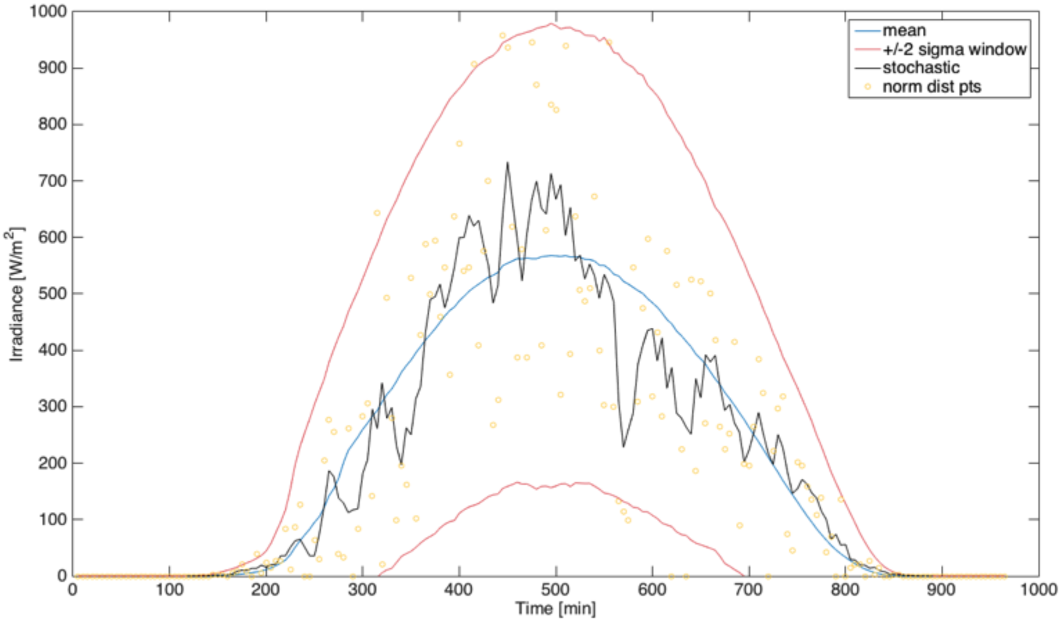

Figure 6.18: Mean, variance bounds, and example stochastic day constructed from randomized progression and probability density function

the day in which the WSN operates. This is a measure of the WSN's reliability, with a perfectly reliably WSN achieving 100% up time. By including larger energy harvesters and more energy reservoirs, we are able to improve the operation of the simulated WSN toward 100% reliability.

Chapter 7

Conclusion

7.1 Supercapacitors as Energy Storage

Recognizing and understanding the phenomena of electrostatic energy storage, the supercapacitor builds on the mechanism of parallel plate capacitance to store considerable energy in a small volume. By affecting the charge separation distance and available surface area we greatly improve the capacitor's energy storage density and the total quantity of charge stored. While supercapacitors can store larger amounts of energy than parallel plate ancestors, they are comparatively more power limited because they contain liquid electrolytes and must obey diffusive speed limits while charging and discharging. Relative to batteries, however, supercapacitors provide greater power density and can cycle many more times because they don't rely on faradaic charge processes to store energy. These high power density and medium energy density properties make supercapacitors excellent candidates when considering pulsed electrical demands like those found in radio communication. Extending beyond microscale devices, supercapacitors are well tailored for high power demands like regenerative vehicle braking, utility-scale power regulation,

7.2 Experimental Work

Cell Manufacturing

The manufacturing process of our experimental supercapacitors has transitioned from pneumatic dispenser printing to screen printing, and we have used composite carbon-based inks for both techniques. Beginning with dispenser printing, we examined ink composition to improve cell performance. Previous ink compositions from our lab focused on mesocarbon microbeads as functional electrodes. These microbeads were embedded in a polymer binder to form symmetric electrodes around a porous polymer separator layer. An ionic liquid electrolyte permeated all three of these layers to ensure ion availability. Our work used a nearly identical cell architecture, but replaced the mesocarbon microbeads with a composite carbon mixture of activated carbon, acetylene black, and graphite. By simply changing to this improved carbon material, we improved the cell capacitance by more than 100 times.

With an improved ink composition that was proven with dispenser printing, we set our attention on increasing manufacturing throughput by using screen printing to produce cells. Repeatability is hypothesized to improve with screen printing because layer thickness is a function of the screen's design parameters. By carefully selecting the screen parameters we designed a screen to reduce the spread of the output cell's capacitance and produced 96 cells in a single print. This screen design produced a grid of cells that were electrically configurable to form any combination of series and parallel connection.

Integration

Combining energy storage manufactured in our labs with energy harvesting fabricated in the labs of our collaborators, we demonstrate the viability of a printed power platform to support wireless sensor node operation. By matching the voltage capabilities of organic photovoltaics with those of supercapacitors, we are able to fabricate a power management system which operates autonomously and dynamically adjusts its duty cycle as energy availability fluctuates. By intelligently monitoring stored energy levels and keeping processing and communication protocols dormant as often as possible, the sensor node is able to autonomously manage its power reservoirs.

Solar cells fabricated in this work were tailored to function most efficiently in indoor environments, where light spectra and intensities make silicon solar cells impractical. In these low intensity environments, the organic solar cell's dark current performance is one of the most important characteristics. Because the solar cell's output current is lower in low light environment, the supercapacitor's charge time is proportionally longer in low light. Mitigating leakage losses during this extended charge time is paramount for ensuring the supercapacitor is able to gain a net positive charge during harvesting. The combination of the solar cell and supercapacitor enables the system to supply high peak currents for radio transmission even if the sensor node is harvesting from extremely low power light.

7.3 Device Modeling

The performance of supercapacitor cells is highly dependent on the geometry of the cell's architecture. Whether cells are printed or manufactured through other means, the mechanism of ion migration through porous media can be applied to any electrochemical cell. By combining studies of porous electrodes and the geometry of interest, we are able to create an analytical model of the capacitive behavior of our supercapacitors. We compare the closed form solution to the FEA solution determined with COMSOL multiphysics and see excellent agreement while reducing computation time. The speed of the closed form solution enables investigators to explore a range of cell geometries to find the optimal geometry for the electrochemical cell of interest.

7.4 System Modeling and Optimal Sizing

In the context of powering a wireless sensor node, we consider sizing the energy harvesting components for a high power and low duty cycle power demand. In designing for the application's power demand, an engineer aims to avoid improperly sizing components - to small and the system has inadequate voltage and current capabilities; too large, and the system will incur detrimentally large leakage currents during periods of inadequate harvesting.

First, we consider a Dynamic Programming approach which searches the entire solution space over the specified number of energy reservoirs and power generators. This model uses first order circuit models on a dual reservoir system which includes batteries and supercapacitors. For the observed load demand and period, the Dynamic Programming model identifies the optimal solution which obviates the battery reservoir. This use case is feasible over short periods where generator power is constant, although including a battery reservoir would extend the operation of the WSN beyond energy harvestable hours.

Second, we consider Particle Swarm Optimization for examining the optimal component sizes in a dual reservoir sensor node. This method is able to explore a nonconvex solution space by populating that space with example particles with position and velocity. Leveraging swarm knowledge of the best known solution, and each particle's best solution, the swarm explores the space and converges at a local optima. After instantiating this swarm with many different starting seeds, the particle swarm optimization converges on an optimal solution. We compare this optimal solution to a solution based on engineering calculations and expected ranges of component sizes and find the PSO to achieve a 55% reduction in total component size.

7.5 Integration with Other Power Systems

Throughout this work we have examined and demonstrated the feasibility of energy harvesting systems in support of wireless sensor nodes. We primarily considered harvesting energy from DC power sources like photovoltaics and thermoelectric generators, but the concepts of energy storage needs, system modeling, and optimal sizing are all concepts that can be applied to broader system design. First, we can consider harvesting energy from an alternating source like piezoelectric vibrations, electric generator coupling, or even electromagnetic coupling from wireless power transfer. To include AC harvesting, the only necessary change is to include AC/DC conversion between the harvester and electrical storage. AC/DC converting ICs are available commercially, and the accompanying passive components (resistors, capacitors, inductors, and diodes) could be printed by using the techniques described in the experimental section and screen design sections of this work.

PZT, Electromagnetic

Piezoelectric energy harvesting is another readily available power source at the microscale. Work by Pit Pillatch, Lindsay Miller, and Professor Eric Yeatman [62, 27] show promising work in harvesting low power vibration energy using piezoelectric beams. This work highlights the feasibility of harvesting AC power from vibrational sources at the microscale, and could be readily adapted for DC power conversion with small AC rectifiers.

Electromagnetic power generation at the microscale represents another widely available power source for distributed computing. Work at Imperial College London [37] by Professor Eric Yeatman and Professor Andrew Holmes have made great strides in creating microscale energy harvesters from micro wind turbines. Micro wind turbines can generate power on the order of whole milliwatts with wind speeds between six and ten meters per second. These wind speeds are seen in myriad locations from industrial, agricultural, urban, and rural settings. Just like piezoelectric energy harvesting, electromagnetic energy harvesting would require AD-DC conversion to support the DC power demands of wireless sensor nodes.

7.6 Network Reliability

We discussed the reliability of energy harvesting nodes subject to environments of variable power availability. By modeling the power flows within a single node we were able to predict the startup time and operation duration of that node over the course of a day. This work gives insight into the behavior of a single node and leads to the question of the reliability of networks of such nodes.

7.7 Stochastic Harvesting: Machine learning

Looking forward at opportunities for robust sensor node design, it is apparent that understanding the energy availability in varied environments will be critical for ensuring reliable operation of distributed computing in the wild. While engineers are capable in designing energy harvesting systems with adequate safety margins to provide operation in known environments, the enormous variation in energy availability on a spacial and temporal level is difficult to address with a single hardware solution. Enter machine learning. By observing the variations in energy availability across an enormous spacio-temporal dataset, techniques in machine learning may be able to predict pathways of robust network communication in real time and adjust node behaviors at the individual level. Only by considering the network as a whole while controlling individual nodes, will truly robust sensor networks be achieved.

Chapter 8

Appendix

8.1 Integral Transformations

Although the integral in equation 4.7 is divergent at the desired boundaries of integration, it diverges at those points more rapidly than z^{-1}, which means the integrals converge to a finite value. The following transformations were performed in order to calculate the definite integrals numerically:

$$
\begin{aligned}
A' &= -\int_0^A \frac{\sqrt{B^2-z^2}\quad dz}{\sqrt{A^2-z^2}\sqrt{C^2-z^2}\sqrt{D^2-z^2}}\\
&= -\int_0^{\frac{\pi}{2}} \frac{\sqrt{B^2-A^2sin^2\theta}\quad d\theta}{\sqrt{C^2-A^2sin^2\theta}\sqrt{D^2-A^2sin^2\theta}}
\end{aligned}
$$

$$
\begin{aligned}
B' &= -i\int_A^B \frac{\sqrt{B^2-z^2}\quad dz}{\sqrt{z^2-A^2}\sqrt{C^2-z^2}\sqrt{D^2-z^2}}\\
&= -i\int_0^{\frac{\pi}{2}} \frac{(B^2-A^2)sin^2\theta\quad d\theta}{\sqrt{B^2-(B^2-A^2)sin^2\theta}\sqrt{(C^2-B^2)+(B^2-A^2)sin^2\theta}\sqrt{(D^2-B^2)+(B^2-A^2)sin^2\theta}}
\end{aligned}
$$

$$
\begin{aligned}
C' &= -\int_B^C \frac{\sqrt{z^2-B^2}\quad dz}{\sqrt{z^2-A^2}\sqrt{C^2-z^2}\sqrt{D^2-z^2}}\\
&= -\int_0^{\frac{\pi}{2}} \frac{(C^2-B^2)sin^2\theta\quad d\theta}{\sqrt{B^2+(C^2-B^2)sin^2\theta}\sqrt{(B^2-A^2)+(C^2-B^2)sin^2\theta}\sqrt{(D^2-B^2)-(C^2-B^2)sin^2\theta}}
\end{aligned}
$$

$$
\begin{aligned}
D' &= -\int_B^C \frac{\sqrt{z^2-B^2}\quad dz}{\sqrt{z^2-A^2}\sqrt{z^2-C^2}\sqrt{D^2-z^2}}\\
&= -i\int_{\frac{\pi}{4}}^{\frac{\pi}{2}} \frac{\sqrt{(D^2-B^2)-(D^2-C^2)sin^2\theta}\quad d\theta}{\sqrt{(D^2-A^2)-(D^2-C^2)sin^2\theta}\sqrt{D^2-(D^2-C^2)sin^2\theta}}\\
&- i\int_{\frac{\pi}{4}}^{\frac{\pi}{2}} \frac{\sqrt{(C^2-B^2)-(D^2-C^2)sin^2\theta}\quad d\theta}{\sqrt{(C^2-A^2)+(D^2-C^2)sin^2\theta}\sqrt{C^2+(D^2-C^2)sin^2\theta}}
\end{aligned}
$$

The mapping between z and z” coordinates in equation 4.8 is given in [57].

Bibliography

[1] Thomas R Andersen et al. “Scalable, ambient atmosphere roll-to-roll manufacture of encapsulated large area, flexible organic tandem solar cell modules”. In: *Energy and Environmental Science* 7 (Aug. 2014), pp. 2925–2933.

[2] Dechan Angmo and Frederik C Krebs. “Over 2 Years of Outdoor Operational and Storage Stability of ITO-Free, Fully Roll-to-Roll Fabricated Polymer Solar Cell Modules”. In: *Energy Technology* 3.7 (June 2015), pp. 774–783.

[3] Michel Armand et al. “Ionic-liquid materials for the electrochemical challenges of the future”. In: *Nature materials* 8.8 (July 2009), pp. 621–629.

[4] L C J Blystad, E Halvorsen, and S Husa. “Piezoelectric MEMS energy harvesting systems driven by harmonic and random vibrations”. In: *Ultrasonics, Ferroelectrics, and Frequency Control, IEEE Transactions on* 57.4 (Apr. 2010), pp. 908–919.

[5] Benjamin Bouthinon et al. “Impact of Blend Morphology on Interface State Recombination in Bulk Heterojunction Organic Solar Cells”. In: *Advanced Functional Materials* 25.7 (Jan. 2015), pp. 1090–1101.

[6] James Brown and Ruel Churchill. “Complex Variables and Applications”. In: *McGraw-Hill Higher Education* (Jan. 2008), pp. 1–482.

[7] Davide Brunelli et al. “Design of a Solar-Harvesting Circuit for Batteryless Embedded Systems”. In: *IEEE Transactions on Circuits and Systems I: Regular Papers* (2009).

[8] A Chen et al. “Dispenser-printed planar thick-film thermoelectric energy generators”. In: *J. of Micromechanics and Microengineering* 21.10 (Sept. 2011), pp. 104006–9.

[9] Chun-Chao Chen et al. “An Efficient Triple-Junction Polymer Solar Cell Having a Power Conversion Efficiency Exceeding 11 percent”. In: *Advanced Materials* 26.32 (July 2014), pp. 5670–5677.

[10] Tao Chen, Zhibin Yang, and Huisheng Peng. “Integrated Devices to Realize Energy Conversion and Storage Simultaneously”. In: *ChemPhysChem* 14.9 (Apr. 2013), pp. 1777–1782.

[11] Tao Chen et al. “An Integrated Energy Wire for both Photoelectric Conversion and Energy Storage”. In: *Angewandte Chemie International Edition* 51.48 (Oct. 2012), pp. 11977–11980.

[12] Chih-Tao Chien et al. "Graphene-Based Integrated Photovoltaic Energy Harvesting/Storage Device". In: *Small* 11.24 (Feb. 2015), pp. 2929–2937.

[13] Adam P Cohn et al. "All Silicon Electrode Photocapacitor for Integrated Energy Storage and Conversion". In: *Nano letters* 15.4 (Apr. 2015), pp. 2727–2731.

[14] International Electrotechnical Commission. "62391-1: Fixed electric double-layer capacitors for use in electric and electronic equipment". In: (2006).

[15] M A Cowell et al. "Wireless sensor node demonstrating indoor-light energy harvesting and voltage-triggered duty cycling". In: *Journal of Physics: Conference Series* 773 (Dec. 2016), pp. 012033–5.

[16] M Cowell et al. "Composite carbon-based ionic liquid supercapacitor for high-current micro devices". In: *Journal of Physics: Conference Series* 557.1 (Dec. 2014), pp. 012061–5.

[17] Jacob M Crosthwaite et al. "Phase transition and decomposition temperatures, heat capacities and viscosities of pyridinium ionic liquids". In: *The Journal of Chemical Thermodynamics* 37.6 (June 2005), pp. 559–568.

[18] G Dennler et al. "A self-rechargeable and flexible polymer solar battery". In: *Solar Energy* 81.8 (Aug. 2007), pp. 947–957.

[19] D DiLaura et al. *DiLaura: The Lighting Handbook 10th Edition: Reference... - Google Scholar*. Illuminating Engineering Society of . . ., 2011.

[20] Pengcheng Du et al. "Self-Powered Electronics by Integration of Flexible Solid-State Graphene-Based Supercapacitors with High Performance Perovskite Hybrid Solar Cells". In: *Advanced Functional Materials* 25.16 (Mar. 2015), pp. 2420–2427.

[21] Klaus Ellmer. "Past achievements and future challenges in the development of optically transparent electrodes". In: (Nov. 2012), pp. 1–9.

[22] CJM Emmott et al. "" In: *Global Organization Photovoltaic GOPV Confederation Hangzhou China* 97 (2012), pp. 14–21.

[23] N. Espinosa et al. In: *Energy and Environmental Science* 5 (2012), pp. 5117–5132.

[24] J Euler and W Nonnenmacher. "Stromverteilung in Porosen Elektroden". In: *Electrochimica Acta* 2 (1960), pp. 268–286.

[25] Alexander C Forse et al. "Direct observation of ion dynamics in supercapacitor electrodes using in situ diffusion NMR spectroscopy". In: *Nature Energy* 2.3 (Feb. 2017), pp. 16216–7.

[26] Monika Freunek, Michael Freunek, and Leonhard M. Reindl. "Maximum efficiencies of indoor photovoltaic devices". In: *IEEE Journal of Photovoltaics* (2013).

[27] H Fu and E M Yeatman. "A Miniature Radial-Flow Wind Turbine Using Piezoelectric Transducers and Magnetic Excitation". In: *Journal of Physics: Conference Series* 660 (Dec. 2015), pp. 012058–6.

[28] Kjartan Furset and Peter Hoffman. *High pulse drain impact on CR2032 coin cell battery capacity.* Tech. rep. Nordic Semiconductor, Energizer, Nov. 2011.

[29] Maciej Galinski, Andrzej Lewandowski, and Izabela Stepniak. "Ionic liquids as electrolytes". In: *Electrochimica Acta* 51.26 (Aug. 2006), pp. 5567–5580.

[30] SA Gevorgyan et al. "" In: *Advanced Energy Materials* (2015).

[31] Fei Guo et al. "ITO-Free and Fully Solution-Processed Semitransparent Organic Solar Cells with High Fill Factors". In: *Advanced Energy Materials* 3.8 (Apr. 2013), pp. 1062–1067.

[32] Adnan Harb. "Energy harvesting: State-of-the-art". In: *Renewable Energy* 36.10 (2011), pp. 2641–2654. DOI: `10.1016/j.renene.2010.06.014`. URL: `http://dx.doi.org/10.1016/j.renene.2010.06.014`.

[33] Zhicai He. "Single-junction polymer solar cells with high efficiency and photovoltage". In: *Nature Photonics* 9.3 (Feb. 2015), pp. 174–179.

[34] M. Healy, T. Newe, and E. Lewis. "Wireless Sensor Node hardware: A review". In: *IEEE Sensors* (2008).

[35] C C Ho, J W Evans, and P K Wright. "Direct write dispenser printing of a zinc microbattery with an ionic liquid gel electrolyte". In: *Journal of Micromechanics and Microengineering* 20 (Sept. 2010), 9pp.

[36] Christine C Ho et al. "Tailoring Electrochemical Capacitor Energy Storage Using Direct Write Dispenser Printing". In: 16.1 (Dec. 2008), pp. 35–47.

[37] Andrew Holmes. "Turbine Energy Harvester". In: *Imperial College London* (Sept. 2012), pp. 1–5.

[38] M Hosel et al. "" In: *Advanced Energy Materials* 4 (2014).

[39] Xiaosong Hu et al. "Comparison of three electrochemical energy buffers applied to a hybrid bus powertrain with simultaneous optimal sizing and energy management". In: *IEEE Transactions on Intelligent Transportation Systems* 15.3 (2014), pp. 1193–1205. DOI: `10.1109/TITS.2013.2294675`.

[40] Rui Igreja and C J Dias. "Analytical evaluation of the interdigital electrodes capacitance for a multi-layered structure". In: *Sensors and Actuators A: Physical* 112.2-3 (May 2004), pp. 291–301.

[41] Maxim Integrated. "Linear Regulators in Portable Applications". In: *Application Note* (Aug. 2012), number 751.

[42] Yan Jiang et al. "Modeling charge polarization voltage for large lithium-ion batteries in electric vehicles". In: *Journal of Industrial Engineering and Management* 6.2 (June 2013), pp. 1–12.

[43] Maher F El-Kady and Richard B Kaner. "Scalable fabrication of high-power graphene micro-supercapacitors for flexible and on-chip energy storage". In: *Nature Communications* 4 (2013), pp. 1475–9.

[44] F Karray et al. “A review on wireless sensor node architectures”. In: *2014 9th International Symposium on Reconfigurable and Communication-Centric Systems-on-Chip (ReCoSoC)*. IEEE, May 2016, pp. 1–8.

[45] Junaid Ahmed Khan, Hassaan Khaliq Qureshi, and Adnan Iqbal. “Energy management in Wireless Sensor Networks: A survey”. In: *Computers and Electrical Engineering* 41.C (Jan. 2015), pp. 159–176.

[46] B Kim et al. “Layer-by-layer fully printed Zn-MnO2 batteries with improved internal resistance and cycle life”. In: *JP:CS* 660.1 (2015), p. 012009.

[47] R Kötz and M Carlen. “Principles and applications of electrochemical capacitors”. In: *Electrochimica Acta* 45.15-16 (May 2000), pp. 2483–2498.

[48] Balthazar P Lechêne et al. “Organic solar cells and fully printed super-capacitors optimized for indoor light energy harvesting”. In: *Nano Energy* 26 (Aug. 2016), pp. 631–640.

[49] D Lee, G Dulai, and Vassili Karanassios. “ Survey of energy harvesting and energy scavenging approaches for on-site powering of wireless sensor- and microinstrument-networks”. In: *SPIE Defense* (May 2013), 87280S–87280S–9.

[50] Ping Li et al. “High-efficiency inverted polymer solar cells controlled by the thickness of polyethylenimine ethoxylated (PEIE) interfacial layers”. In: *Physical Chemistry Chemical Physics* 16 (Oct. 2014), pp. 23792–23799.

[51] Simon Lineykin and Sam Ben-Yaakov. “Modeling and Analysis of Thermoelectric Modules”. In: *IEEE* (Dec. 2004), pp. 2019–2023.

[52] Jing-Quan Liu et al. “A MEMS-based piezoelectric power generator array for vibration energy harvesting”. In: *Microelectronics Journal* 39.5 (May 2008), pp. 802–806.

[53] Deepa Madan et al. “Dispenser printed composite thermoelectric thick films for thermoelectric generator applications”. In: *Journal of Applied Physics* 109.3 (Feb. 2011), pp. 034904–7.

[54] Ben Minnaert and Peter Veelaert. “A Proposal for Typical Artificial Light Sources for the Characterization of Indoor Photovoltaic Applications”. In: *Energies* 7.3 (Mar. 2014), pp. 1500–1516.

[55] John S Newman and Charles W Tobias. “Theoretical Analysis of Current Distribution in Porous Electrodes”. In: *Journal of The Electrochemical Society* 109.12 (Dec. 1962), pp. 1183–1191.

[56] John S Newman et al. “Modeling of lithium-ion batteries”. In: *Journal of Power Sources* 119-121 (June 2003), pp. 838–843.

[57] W Olthuis, W Streekstra, and P Bergveld. “Theoretical and experimental determination of cell constants of planar-interdigitated electrolyte conductivity sensors”. In: *IEEE Sensors and Actuators* (1995), pp. 1–5.

[58] Aminy E Ostfeld et al. "Single-walled carbon nanotube transparent conductive films fabricated by reductive dissolution and spray coating for organic photovoltaics". In: *Applied Physics Letters* 105.25 (Dec. 2014), pp. 253301–5.

[59] Sung Heum Park et al. "Bulk heterojunction solar cells with internal quantum efficiency approaching 100 percent". In: *Nature Photonics* 3.5 (Apr. 2009), pp. 297–302.

[60] Craig H Peters et al. "High Efficiency Polymer Solar Cells with Long Operating Lifetimes". In: *Advanced Energy Materials* 1.4 (Apr. 2011), pp. 491–494.

[61] Adrien Pierre et al. "High Detectivity All-Printed Organic Photodiodes". In: *Advanced Materials* 27.41 (Sept. 2015), pp. 6411–6417.

[62] P Pillatsch et al. "Self-tuning behavior of a clamped-clamped beam with sliding proof mass for broadband energy harvesting ". In: *Journal of Physics: Conference Series* 476.1 (Dec. 2013), pp. 012123–6.

[63] Riccardo Poli, James Kennedy, and Tim Blackwell. "Particle swarm optimization An overview". In: *Swarm Intelligence* 1 (2007), pp. 33–57. DOI: `10.1007/s11721-007-0002-0`.

[64] Christopher M Proctor and Thuc-Quyen Nguyen. "Effect of leakage current and shunt resistance on the light intensity dependence of organic solar cells". In: *Applied Physics Letters* 106.8 (Feb. 2015), pp. 083301–5.

[65] Jeffery Quill et al. *Quantifying the Indoor Light Environment.* Tech. rep. May 2007.

[66] N H Reich et al. "A solar powered wireless computer mouse: Industrial design concepts". In: *Solar Energy* 83.2 (Feb. 2009), pp. 202–210.

[67] J A Rogers, T Someya, and Y Huang. "Materials and Mechanics for Stretchable Electronics". In: *science* 327.5973 (Mar. 2010), pp. 1603–1607.

[68] L. Roselli et al. "Smart Surfaces: Large Area Electronics Systems for Internet of Things Enabled by Energy Harvesting". In: *IEEE Proceedings* (2014).

[69] Karola Ruhle et al. "Evaluating Crystalline Silicon Solar Cells at Low Light Intensities Using Intensity-Dependent Analysis of I-V Parameters". In: *IEEE Journal of Photovoltaics* (2007).

[70] Daniel Schmidt, Martin D Hager, and Ulrich S Schubert. "Photo-Rechargeable Electric Energy Storage Systems". In: *Advanced Energy Materials* 6.1 (Oct. 2015), pp. 1500369–11.

[71] Patrice Simon and Andrew Burke. "Nanostructured Carbons: Double-Layer Capacitance and More". In: *The Electrochemical Society Interface* (Mar. 2008), pp. 38–43.

[72] Magdalena Skunik-Nuckowska et al. "Integration of solid-state dye-sensitized solar cell with metal oxide charge storage material into photoelectrochemical capacitor". In: *Journal of Power Sources* 234.C (July 2013), pp. 91–99.

[73] Venkat Srinivasan and John Weidner. “Mathematical Modeling of Electrochemical Capacitors”. In: *Journal of The Electrochemical Society* 146.5 (Nov. 1999), pp. 1650–1658.

[74] European Standard. “12464-1 : The Lighting of Workplaces”. In: (2003).

[75] Roland Steim et al. “Organic photovoltaics for low light applications”. In: *Solar Energy Materials and Solar Cells* 95.12 (Dec. 2011), pp. 3256–3261.

[76] Sampo Tuukkanen et al. “Behaviour of one-step spray-coated carbon nanotube supercapacitor in ambient light harvester circuit with printed organic solar cell and electrochromic display”. In: *Nature Publishing Group* (Mar. 2016), pp. 1–9.

[77] R. J M Vullers et al. “Micropower energy harvesting”. In: *Solid-State Electronics* 53.7 (2009), pp. 684–693. DOI: `10.1016/j.sse.2008.12.011`. URL: `http://dx.doi.org/10.1016/j.sse.2008.12.011`.

[78] Xianfu Wang et al. “Flexible Energy-Storage Devices: Design Consideration and Recent Progress”. In: *Advanced Materials* 26.28 (June 2014), pp. 4763–4782.

[79] Grace Wee et al. “Printable photo-supercapacitor using single-walled carbon nanotubes”. In: *Energy Environ. Sci.* 4.2 (2011), pp. 413–416.

[80] John S Wei. “Distributed Capacitance of and Planar Electrodes in Optic and Acoustic Surface Wave Devices”. In: *Journal of Quantum Electronics* (1977), pp. 1–7.

[81] G A H Wetzelaer et al. “Origin of the dark-current ideality factor in polymer:fullerene bulk heterojunction solar cells”. In: *Applied Physics Letters* 99.15 (Oct. 2011), pp. 153506–4.

[82] Alan Chi Wai Wong et al. “A 1 V 5 mA Multimode IEEE 802.15.6/Bluetooth Low-Energy WBAN Transceiver for Biotelemetry Applications”. In: *Solid-State Circuits, IEEE Journal of* 48.1 (Dec. 2012), pp. 186–198.

[83] Jing Xu et al. “Integrated Photo-supercapacitor Based on Bi-polar TiO 2Nanotube Arrays with Selective One-Side Plasma-Assisted Hydrogenation”. In: *Advanced Functional Materials* 24.13 (Nov. 2013), pp. 1840–1846.

[84] Yanfei Xu et al. “Inkjet-printed energy storage device using graphene/polyaniline inks”. In: *Journal of Power Sources* 248.C (Feb. 2014), pp. 483–488.

[85] Zhibin Yang et al. “An integrated device for both photoelectric conversion and energy storage based on free-standing and aligned carbon nanotube film”. In: *J. Mater. Chem. A* 1.3 (2013), pp. 954–958.

[86] Junyeob Yeo et al. “Flexible supercapacitor fabrication by room temperature rapid laser processing of roll-to-roll printed metal nanoparticle ink for wearable electronics application”. In: *Journal of Power Sources* 246.C (Jan. 2014), pp. 562–568.

[87] H Zhang et al. “Acetylene black agglomeration in activated carbon based electrochemical double layer capacitor electrodes”. In: *Solid State Ionics* 179.33-34 (Oct. 2008), pp. 1946–1950.

[88] Xi Zhang et al. “Dye-Sensitized Solar Cell with Energy Storage Function through PVDF/ZnO Nanocomposite Counter Electrode”. In: *Advanced Materials* 25.30 (June 2013), pp. 4093–4096.

[89] Yinhua Zhou et al. “A Universal Method to Produce Low-Work Function Electrodes for Organic Electronics”. In: *science* 336.6079 (Apr. 2012), pp. 324–327.

[90] Yinhua Zhou et al. “All-plastic solar cells with a high photovoltaic dynamic range”. In: *J. Mater. Chem. A* 2.10 (2014), pp. 3492–6.

[91] L. zubieta and R. Bonert. “Characterization of double-layer capacitors for power electronics applications”. In: *IEEE Transactions on Industry Applications* (2000).